Astronomy Letters, Vol. 31, No. 12, 2005, pp. 787–791. Translated from Pis'ma v Astronomicheskiĭ Zhurnal, Vol. 31, No. 12, 2005, pp. 883–887.

Analysis of the Clustering of 2dFGRS Galaxies Using the Method of a Modified Correlation Gamma Function

A. V. Tikhonov*

St. Petersburg State University, Universitetskiĭ pr. 28, St. Petersburg, 198504 Russia

Received February 22, 2005

Abstract—The apparatus of a correlation gamma function is used to analyze a sample of 2dFGRS galaxies. We suggest a modified gamma-function algorithm with nonintersecting working spheres, which ensures that the counts are independent at each step. The method of nonintersecting spheres has revealed a change in the regime of clustering (a break of the gamma function) on a scale of $10–16h^{-1}$ Mpc ($H_0 = 65$ km s^{-1} Mpc^{-1}). The standard method yields a scale of $30h^{-1}$ Mpc. An artificial distribution is used as an example to show that, in some cases, the modified algorithm is more responsive to a mixture of distributions with various properties than the standard method. © *2005 Pleiades Publishing, Inc.*

Key words: *galaxies, large-scale structure.*

INTRODUCTION

The method of a correlation gamma function (or a conditional density) was introduced into astrophysics by L. Pietronero, who noticed that the main features of the form of the gamma function are consistent with the ideas of a fractal distribution of galaxies in a certain range of scales (Coleman and Pietronero 1992). The results of gamma analysis became the subject of extensive discussion (Pietronero *et al.* 1997). The technique of counting based on the gamma-function method was described in detail by Coleman and Pietronero (1992) and Tikhonov (2002). In the classical gamma-function method, the density variation with distance is computed in spheres (the integral Γ^* function) and spherical layers (the differential gamma function). Any objects of the sample the spheres around which are located within the geometrical boundaries of the sample can act as the centers of the spheres. Thus, the spheres considered can intersect, and the galaxy counts in them are not fully independent. Furthermore, for a typical geometry of galaxy and cluster samples on various scales (various radii of the working spheres), different objects of the sample contribute to the counts; i.e., the sample objects are not used on equal terms, because the objects located near the boundaries rapidly fall out of the calculations as the centers of the spheres. In this paper, we suggest a modified gamma-function algorithm (the method of nonintersecting spheres), a technique that differs from the classical method of counting.

*E-mail: avt@gong.astro.spbu.ru

THE METHOD OF INDEPENDENT SPHERES

In our approach, the maximum spheres, which are defined by the condition of their location strictly within the geometrical boundaries of the sample (see Tikhonov (2002) for the gamma-function algorithm) and which are fixed before the counts around the sample objects begin, are chosen in such a way that they do not overlap (Fig. 1). Thus, at each step (at each working radius r of the spheres around the objects

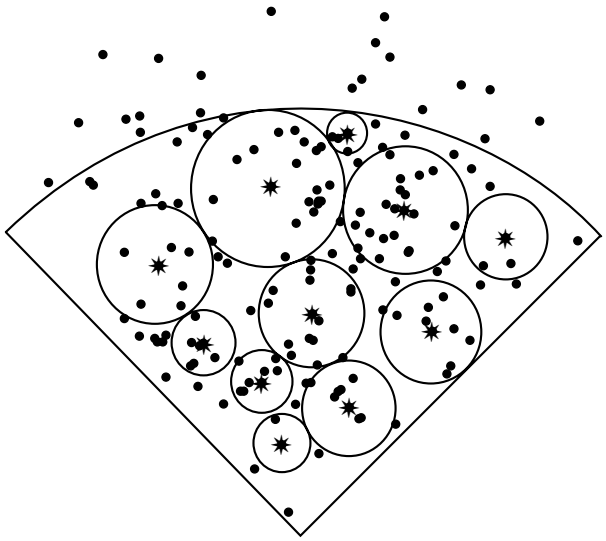

Fig. 1. Nonintersecting spheres. A two-dimensional illustration of the modified gamma-function algorithm. The region of sample completeness is outlined by the boundary.

1063-7737/05/3112-0787$26.00

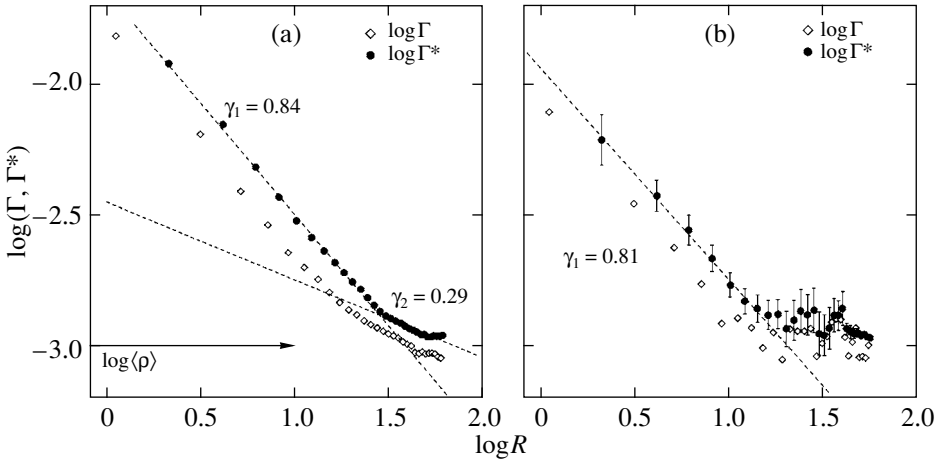

Fig. 2. Gamma-function for the 2dFGRS sample of galaxies: (a) analysis by the classical method and (b) analysis using the modified algorithm. Here, $\langle\rho\rangle$ is the mean density of the 2dFGRS galaxy sample.

in which the galaxies are counted), the spheres do not overlap, thereby ensuring that the values of the gamma function are independent when averaging at this step. The counts with the working radius r within a given maximum sphere of radius R^i are performed as long as the condition $r < R^i$ is satisfied. When $r > R^i$, the sphere is excluded from the counts, as in the classical version of the method. Choosing the first sphere to be close in volume to the largest sphere that can be fitted within the geometrical boundaries of the sample, we obtain smaller remaining maximum spheres, and, starting from a certain scale, only one sphere is involved in the counts. The number of spheres with close radii increases with decreasing radius of the initial sphere (i.e., when limiting the maximum counting scale); i.e., the statistics become better on larger scales. The sample size becomes very important for the quality of the modified counting version. We compared the classical and modified methods as applied to a sample of 2dFGRS galaxies.

DESCRIPTION OF THE 2dFGRS SURVEY

The second edition of the 2dFGRS survey of galaxies and quasars (Colles *et al.* 2001, 2003) includes ~250 000 galaxies and up to 25 000 quasars. The redshifts were measured using a multiobject spectrograph with a 2° field, which is capable of taking 400 spectra during a single exposure. The survey was based on the APM photometric catalog ($b_j < 20.5$). All of the galaxies with their magnitudes corrected for Galactic extinction in the range $14.5 < b_j < 19.5$ were selected for 2dFGRS. The main region in the sky covered by 2dFGRS consists of two bands, 80° in right ascension and 15° in declination near the South Galactic Pole and 75° and 10°, respectively, in the Northern Galactic Hemisphere. In addition, the survey includes galaxies in 99 randomly located fields in the high-latitude region of the Southern Galactic Hemisphere. The survey covers ~2000 square degrees and has a median depth of $z = 0.11$. We chose an area in the southern sky for our analysis by the gamma-function method in such a way that the sphere of the largest possible radius at the redshift limit under consideration fit within the geometrical boundaries of the sample. The boundaries of the resulting sample are: $21^{\rm h}.8 < \alpha < 23^{\rm h}.3$, $-36° < \delta < -24°$, $0.03 < z < 0.13$. We constructed a volume-limited sample containing 6633 galaxies with $M_{\rm abs} < -19.9$. To estimate the absolute magnitudes of the galaxies, the K-correction was computed in the same way as in the 2dFGRS survey when constructing the luminosity function (Madgwick *et al.* 2002). The metric distances were recalculated from the redshifts using a formula from Pen (1999). The Hubble parameter is $H_0 = 65$ km s^{-1} Mpc^{-1}, and the density parameters are $\Omega_{\rm tot} = 1$, $\Omega_{\rm vacuum} = 0.7$, and $\Omega_0 = 0.3$.

RESULTS

Figure 2a shows the result of galaxy counting by the standard gamma-function method. The slope is $\gamma_1 = 0.84 \pm 0.03$, which corresponds to a fractal dimension of $D = 3 - \gamma \approx 2.16$ for the galaxy distribution in the fractal interpretation of the gamma-function slope. As in previous analyses of galaxy samples (Tikhonov *et al.* 2000), two regimes of variation in the gamma function are distinguished. Starting from a scale of $R_0 \approx 30h^{-1}$ Mpc, a well-defined change in the slope of the integral gamma function (of the form of the dependence $\log\Gamma^* \log R$) from $\gamma_1 = 0.84$ to $\gamma_2 = 0.29 \pm 0.02$) is observed. This is indicative of a change in the clustering regime of the

2dFGRS galaxy survey on scales larger than R_0. The limiting counting scale for the selected area of the 2dFGRS survey is $R_s = 62h^{-1}$ Mpc.

In implementing the method of independent spheres, we first fixed the set of maximum spheres around all the galaxies of the sample centered on these galaxies. Subsequently, we sorted this set in order of decreasing radius of the sphere. After choosing a particular sphere (center) from the resulting set as the initial sphere, all of the remaining covering spheres were chosen according to the following rule: at each step, we added the maximum possible sphere that intersects neither with the sample boundaries nor with the already chosen covering spheres to the covering. There are many variants of covering the sample volume by spheres. Different variants are realized, for example, by choosing different first spheres for the set of covering spheres or by decreasing the radius of the first sphere. Clearly, different independent coverings are obtained in this way each time. Figure 2b shows a typical result of calculations by the method of independent spheres. Sphere no. 50 from the sorted set of maximum spheres (the initial number of the set is 0) was taken as the initial sphere. The pattern of correlations does not differ fundamentally from that in Fig. 2a: the slope is $\gamma_1 = 0.81 \pm 0.03$, and the break is observed even on a scale of $R_0 \approx 10{-}16h^{-1}$ Mpc; the slope is virtually zero after the break. A number of coverings produced by the method described above yielded the following results: the scale of the break is $R_0 \approx 10{-}16h^{-1}$ Mpc; the slope before the break γ_1 varies within the range 0.61–1.00; the error of the linear fit is less than 0.1, and the form of the gamma function may deviate from that in Fig. 2a after the break.

Thus, the spread of slopes γ_1 casts doubt on the possibility of describing the distribution of 2dFGRS galaxies by a monofractal with a single dimension even on small scales—the slope of the gamma function depends on the covering. The classical and modified methods yield significantly different positions of the breakpoint: for the method of nonintersecting spheres, this scale is a factor of about 2 smaller, with its value depending only slightly on the covering. If we introduce a parameter characterizing the degree of sphere intersection in the algorithm, then we can analyze the pattern of change in the form of the gamma function for various degrees of overlapping between the limiting spheres. In the algorithm considered, this is the working parameter Int (it can be negative). In constructing the set of covering spheres, this parameter determines the minimum distance between the center of the new sphere to be included in the covering and the boundary of the sphere that has already been included in the covering when the center of the new sphere falls within the sphere from the set of covering formed by the step considered. Figure 3 shows variants of the computation of the modified gamma function for various parameters Int. One can clearly see that the breakpoint moves toward the larger scales and that the length of the portion of the gamma function after the break, where a different regime of galaxy clustering, is decreases with increasing degree of sphere intersection. The break

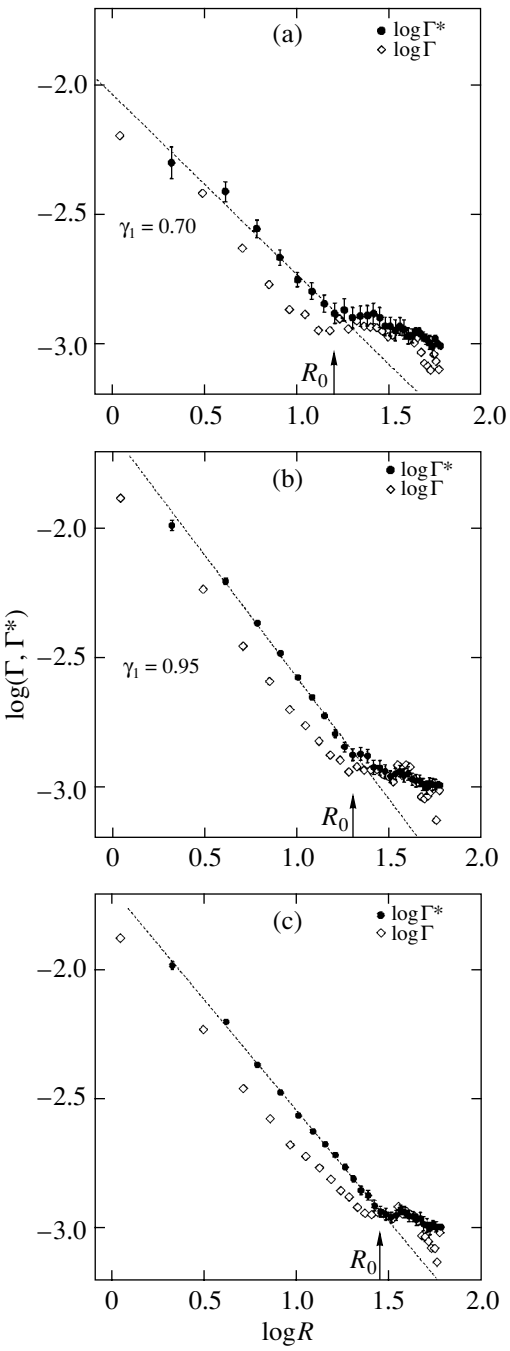

Fig. 3. Modified gamma function of the 2dFGRS galaxies with various intersection parameters: (a) Int = 5, (b) Int = 15, and (c) Int = 20.

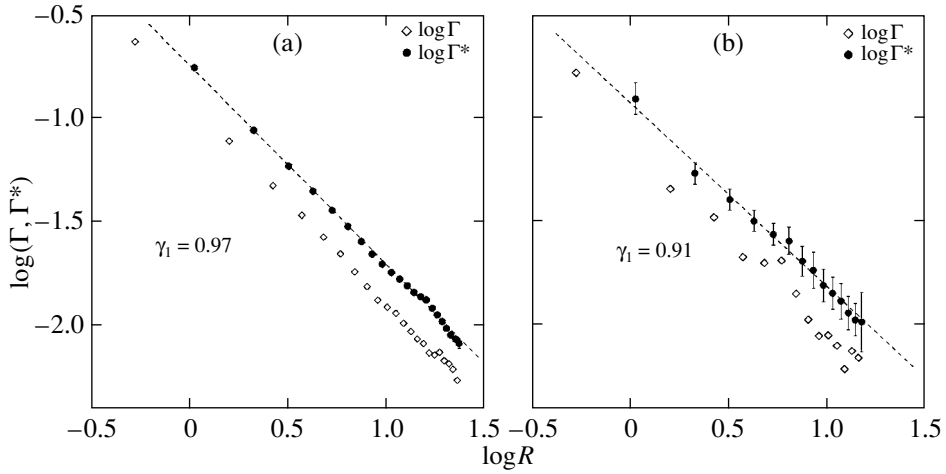

Fig. 4. Gamma function for an artificial fractal distribution (a β cascade): (a) analysis by the classical method and (b) analysis using the modified algorithm.

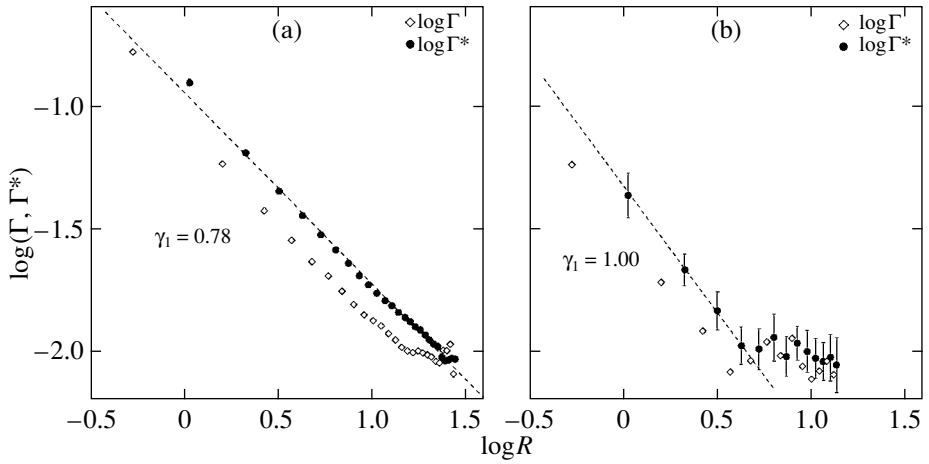

Fig. 5. Gamma function for a fractal distribution with a uniform background: (a) analysis by the classical method and (b) analysis using the modified algorithm.

scale approaches the value obtained by the classical gamma-function method.

AN ARTIFICIAL DISTRIBUTION

To illustrate the differences between the results obtained using the classical algorithm and the method of nonintersecting spheres, we used an artificial fractal distribution with a dimension of $D = 2$ generated using something known in the literature as a β cascade (Paladin and Vulpiani 1987). In this paper, we divided the initial cube uniformly filled with 10^5 points iteratively, with the cube division into eight parts at each iteration; the cubic volumes (increasingly small at each iteration) remained empty with a probability of $p = 0.5$. After seven iterations, the regions that were not marked as empty were filled with 10^5 points. Figure 4 shows the results of applying both the classical and modified gamma-function methods to the derived distribution of 1500 points with a density of 7×10^{-4}. When using the method of nonintersecting spheres, the gamma function shows a nonzero slope over the entire interval of our computations, and this slope remains close to that inferred by the classical method and to the slope $\gamma = 3 - D = 1$ determined by the fractal dimension. Analysis of the variant with the addition of a uniform background of 750 points (with a density of 10^{-3}) is presented in Fig. 5. The addition of a uniform distribution component has virtually no effect on the classical gamma-function (slope decreases to $\gamma_0 = 0.72 \pm 0.01$), but the modified algorithm "feels" it well. This is an example of the fact that, in contrast to the classical method, the method of nonintersecting spheres responds to a change in the properties of the distribution in some special cases.

CONCLUSIONS

Thus, a test using fairly simple artificial samples shows that in those cases where the sample is a mixture of distributions with different properties (a highly likely model for the actual distribution of galaxies), the algorithm with nonintersecting spheres reflects more accurately the presence of these properties than the classical gamma-function method. The scale of the break for the classical gamma function (if it exists) appears to be an upper limit for the actual scale of the change in the clustering regime, while a covering of nonintersecting spheres yields a much lower value of this scale. Since the gamma function is commonly used as a tool for determining the scale length of the region with a fractal distribution of galaxies, it seems appropriate to use the method of independent spheres as an additional tool.

ACKNOWLEDGMENTS

This work was supported by the Administration of St. Petersburg (grant no. PD05-1.9-117) and the "Astronomy" federal science and technology program (grant no 40.022.1.1.1001).

REFERENCES

1. P. H. Coleman and L. Pietronero, Phys. Rep. **213**, 311 (1992).
2. M. M. Colles, G. Dalton, S. Maddox, *et al.* (the 2dFGRS Team), Mon. Not. R. Astron. Soc. **328**, 1039 (2001).
3. M. M. Colles, B. Peterson, C. Jackson, *et al.* (the 2dFGRS Team), astro-ph/0306581 (2003).
4. D. S. Madgwick, O. Lahav, I. Baldry, *et al.*, Mon. Not. R. Astron. Soc. **333**, 133 (2002).
5. G. Paladin and A. Vulpiani, Phys. Rep. **156**, 147 (1987).
6. Ue-Li Pen, Astrophys. J., Suppl. Ser. **120**, 49 (1999).
7. L. Pietronero, M. Montuori, and F. Sylos Labini, *Critical Dialogues in Cosmology*, Ed. by N. Turok (World Sci., Singapore, 1997), p. 24.
8. A. V. Tikhonov, Astrofizika **45**, 99 (2002) [Astrophys. **45**, 79 (2002)].
9. A. V. Tikhonov, D. I. Makarov, and A. I. Kopylov, Bull. Spets. Astrofiz. Obs. **50**, 39 (2000).

Translated by A. Dambis

Astronomy Letters, Vol. 31, No. 12, 2005, pp. 792–805. Translated from Pis'ma v Astronomicheskiĭ Zhurnal, Vol. 31, No. 12, 2005, pp. 888–902.

Optical Observations of Type-IIP Supernova 2004dj: Evidence for Asymmetry of the ^{56}Ni Ejecta

N. N. Chugai[1*], S. N. Fabrika[2], O. N. Sholukhova[2], V. P. Goranskij[2], P. K. Abolmasov[3], and V. V. Vlasyuk[2]

[1] *Institute of Astronomy, Russian Academy of Sciences, ul. Pyatnitskaya 48, Moscow, 119017 Russia*

[2] *Special Astrophysical Observatory, Russian Academy of Sciences, 369167 Karachai-Cherkessian Republic, Nizhnii Arkhyz, Russia*

[3] *Sternberg Astronomical Institute, Universitetskiĭ pr. 13, Moscow, 119992 Russia*

Received July 19, 2005

Abstract—Photometric and spectroscopic observations of the nearby type-IIP supernova 2004dj are presented. The ^{56}Ni mass in the envelope of SN 2004dj was estimated from the light curve to be $\approx 0.02 M_\odot$. This estimate is confirmed by modeling the Hα luminosity. The Hα emission line exhibits a strong asymmetry characterized by the presence of a blue component in the line with a shift of -1600 km s^{-1} at the early nebular phase. A similar asymmetry was found in the Hβ, [O I], and [Ca II] lines. The line asymmetry is interpreted as being the result of asymmetric ^{56}Ni ejecta. The Hα profile and its evolution are reproduced in the model of an asymmetric bipolar ^{56}Ni structure for a spherical hydrogen distribution. The mass of the front ^{56}Ni jet is comparable to that of the central component and twice that of the rear ^{56}Ni jet. We point out that the asymmetric bipolar structure of ^{56}Ni ejecta is also present in SN 1999em, a normal type-IIP supernova. © *2005 Pleiades Publishing, Inc.*

Key words: *supernovae and supernova remnants*.

1. INTRODUCTION

The supernova SN 2004dj was discovered on July 31, 2004, in the Sc galaxy NGC 2403 (Nakano *et al.* 2004). According to its light curve and spectra (Korcakova *et al.* 2005), this is an ordinary type-IIP supernova (i.e., with a plateau in the light curve) detected 30–45 days after the explosion. With the distance of 3.13 Mpc (Freedman *et al.* 2001), this is the nearest SN IIP after SN 1987A and, given the peculiarity of the latter SN 2004dj, the nearest known normal SN IIP.

Type-IIP supernovae are associated with the explosion (of an as yet not quite clear nature) of a massive (10–25 $M_\odot$) red supergiant following the collapse of its iron core. Three versions of the explosion mechanism have been proposed: (1) a neutrino mechanism (Colgate and White 1966; Buras *et al.* 2003), (2) a magnetorotational mechanism (Ardelyan *et al.* 2005), and (3) rotational fragmentation of a rapidly rotating neutron star followed by the explosion of an unstable fragment with a mass of $\sim$0.1 $M_\odot$ (Blinnikov *et al.* 1990). In any case, the generated shock wave ejects the envelope with an internal energy enough to provide the SN IIP luminosity at the plateau stage (Grasberg *et al.* 1971). The shock propagation in a silicon mantle results in the synthesis of iron-peak elements, including radioactive ^{56}Ni; its decay ^{56}Ni–^{56}Co–^{56}Fe maintains the SN IIP luminosity in the tail of the light curve (Weaver and Woosley 1980). As of yet none of the proposed explosion models reproduces the empirical values of the explosion energy and the ejected ^{56}Ni mass of SN IIP.

The proximity of SN 2005dj provides a unique opportunity to study in greater detail the observational manifestations of the explosions of normal SN IIP. Unfortunately, the supernova was discovered long after the explosion, so the explosion energy cannot be derived from hydrodynamic modeling. At the same time, the light curve and the Hα luminosity at the nebular epoch can yield an estimate of the ejected ^{56}Ni mass (Elmhamdi *et al.* 2003b), another vital property of the explosion mechanism.

Studying the emission line profiles at the nebular epoch is of particular interest, since these can contain important information about the possible explosion asymmetry in SN IIP. The problem of the explosion asymmetry arose after the detection of an

*E-mail: nchugai@inasan.ru

emission line redshift in SN 1987A (Phillips and Williams 1991) and the interpretation of this redshift as being the result of ^{56}Ni ejecta asymmetry (Chugai 1991). A similar phenomenon was recently detected in a normal SN IIP, SN 1999em (Elmhamdi *et al.* 2003a). There is reason to believe that the ^{56}Ni ejecta asymmetry as well as the high initial pulsar velocities are closely related to the violation of a point symmetry in core-collapse supernovae due to large-scale neutrino convection immediately after the collapse (Herant *et al.* 1992).

Below, we present the results of our spectroscopic and photometric observations of SN 2004dj at the Special Astrophysical Observatory (SAO). Apart from a qualitative analysis of the spectra and photometry, we present the estimates of the ^{56}Ni mass in SN 2004dj obtained from the light curve and the Hα luminosity. The observed spectra of SN 2004dj reveal an unusually strong Hα asymmetry. Given the importance of this phenomenon, attention is focused on studying in detail the line asymmetry and its relationship to the asymmetry of ^{56}Ni ejecta.

Below, we use the distance $D = 3.13$ Mpc (the distance module $\mu = 27.48$) derived from Cepheids (Freedman *et al.* 2001) and the redshift of 129 km s^{-1} from the LEDA database.

2. OBSERVATIONS

Broad-band $BVRc$ photometry of SN 2004dj was performed with a 1-m Zeiss telescope at the SAO using Electronika K-585 and EEV 42-40 CCDs and with a 60-cm telescope at the Crimean Station of the Sternberg Astronomical Institute (SAI) using a VersArray CCD (Princeton Instruments). These three detectors are designated as K, E, and VA for short, respectively. The local photometric standard in the vicinity of the supernova is referenced to the $UBVR$ standard near the galaxy NGC 2403 (Zickgraf *et al.* 1990). The CCD images were reduced with the WinFITS software package written by V.P. Goranskij using the method of corrected aperture measurements and with allowance made for the inhomogeneous background of the galaxy around the supernova. The measurement accuracy is $0^m.005$–$0^m.010$. The photometric data are presented in Table 1. The columns give the Julian dates, the magnitudes, and the detector types. The first row of the table contains the photometry obtained on January 19, 2001, i.e., long before the explosion; these magnitudes probably refer to the star cluster S96 on which SN 2004dj is superimposed.

A log of spectroscopic observations, including the dates of observations, the spectrograph types, the spectral range, and the resolution, is given in Table 2.

Table 1. Photometric data for SN 2004dj

JD 2450000+	B	V	Rc	CCD
1929.4831	$18^m.337$	$17^m.836$	$17^m.434$	K
3321.6191	15.949	14.727	14.110	E
3355.5434	16.100	15.068	14.210	VA
3357.5453	16.140	15.082	14.210	VA
3358.5417	16.116	15.083	14.187	VA
3361.5745	16.128	15.129	14.243	VA
3385.3628	16.320	15.342	14.311	E
3386.3845	16.346	15.345	14.326	E
3387.4160	16.320	15.351	14.320	E
3436.4913	16.534	15.666	14.662	E
3437.2683	16.539	15.689	14.678	E
3500.4002	16.044			E

A total of eight spectra for SN 2004dj were taken from October 18, 2004, through June 9, 2005. The first spectrum was obtained during the transition from the plateau to the tail of the light curve, while the remaining spectra were taken at the tail of the light curve. Three spectrographs were used in the observations: the Scorpio universal focal reducer (Afanasiev and Moiseev 2005) of the 6-m large azimuthal telescope (LAT), the multipupil fiber spectrograph (MPFS) of the LAT, and the UAGS spectrograph of the 1-m SAO telescope. The Scorpio and UAGS CCD images were reduced using the MIDAS package with the standard procedures of cosmic-ray hit removal, flat fielding, and spectra extraction. The MPFS images were reduced using a software package written in IDL by V.L. Afanasiev, A.V. Moiseev and P.K. Abolmasov. In two cases (spectra 2 and 6 in Table 2), atmospheric dispersion modifies appreciably the spectral energy distribution. Therefore, these two spectra cannot be used to measure the Hα flux. However, they may well be used to analyze the line profiles.

3. PHOTOMETRY AND THE ^{56}Ni MASS

The V light curve according to our measurements and amateur data[1] is shown in Fig. 1. The time is counted off from JD 2453170 (June 13, 2004), which we took as the explosion date. This estimate is based on the assumption that the light curves of SN 2004dj and SN 1999gi, a standard SN IIP (Leonard *et al.* 2002), are identical. This assumption is supported by the fact that the analytical fit to the

[1] http://www.astrosurf.com/snweb2/2004dj/Meas.htm

Table 2. Log of spectroscopic observations

Date	JD 2450000+	Spectrograph	Range, Å	Resolution, Å
Oct. 18, 2004	3298.5	LAT Scorpio	3700–7500	13
Oct. 22, 2004	3301.5	1-m UAGS	4000–7800	7.6
Nov. 9, 2004	3320.3	LAT Scorpio	3900–7500	13
Nov. 15, 2004	3325.3	LAT MPFS	4000–7000	6
Jan. 16, 2005	3387.2	LAT MPFS	4000–7000	6
Feb. 5, 2005	3406.8	LAT Scorpio	3900–7500	13
May 9, 2005	3500.3	LAT Scorpio	5700–7400	6
June 7, 2005	3529.4	LAT Scorpio	4000–5700	6

light curve on the plateau and the tail for SN 2004dj describes satisfactorily the light curve for SN 1999gi (Fig. 1). The fit used suggests an exponential behavior of the V-band flux at the tail of the light curve, $F(V) \propto \exp(-t/111\overset{d}{.}26)$, in accordance with the radioactive decay of cobalt (^{56}Co–^{56}Fe).

The last two measurements (days 266 and 267) exceed the value on the exponential tail by $0\overset{m}{.}17$ (Fig. 1). Most of this excess is probably related to the contribution from the star cluster S96. Indeed, assuming an exponential behavior of the intrinsic V magnitude of SN 2004dj, we find that the star cluster on day 266.5 contributed $0\overset{m}{.}14$, given the pre-explosion magnitude (Table 1). Thus, the light from S96 accounts for the observed excess almost completely.

The Galactic reddening toward NGC 2403 is $E(B-V) = 0.062$ (Schlegel *et al.* 1998). We took this value as an estimate of the total reddening of the supernova in our Galaxy and the host galaxy. With this reddening, the intrinsic $B-V$ color of SN 2004dj, as inferred from our (Table 1) and amateur photometric data, is displayed in Fig. 2. Also shown in this figure are the lower envelope of the intrinsic

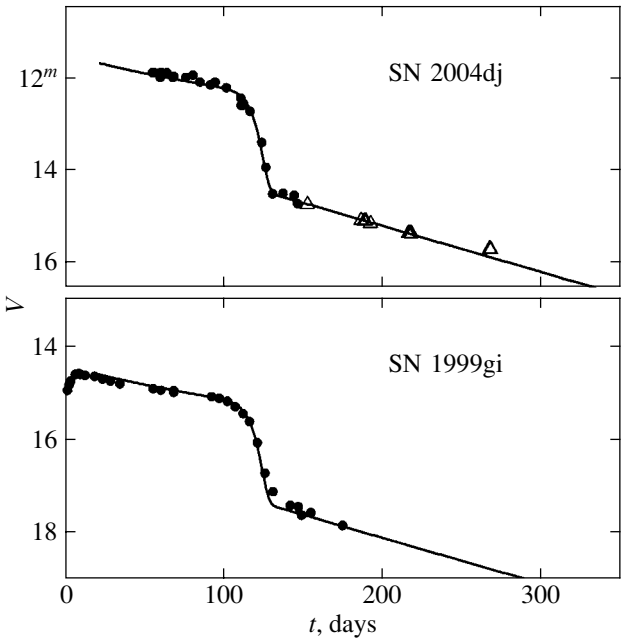

Fig. 1. V-band light curves for SN 2004dj and SN 1999gi: the triangles are our data, and the dots are the data of amateurs; the solid line indicates the analytical fit, the same in both cases. The time is counted off from the explosion date (June 13, 2004).

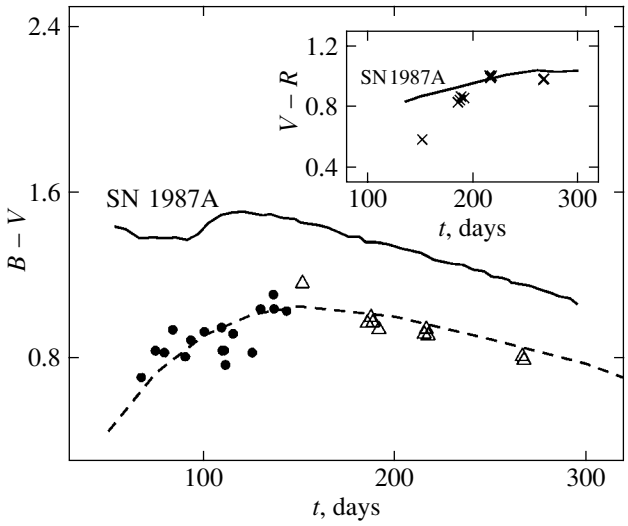

Fig. 2. $B-V$ color curve for SN 2004dj: the triangles are our data, and the dots are the data of amateurs; the solid line represents the color of SN 1987A, and the dashed line is the lower envelope of the $B-V$ color for SN IIP (Elmhamdi *et al.* 2003b). The inset shows the $V-R$ color of SN 2004dj (crosses) in comparison with the color of SN 1987A (line).

$B-V$ colors for a sample of SN IIP (Elmhamdi *et al.* 2003b) and the intrinsic $B-V$ color for SN 1987A (Catchpole *et al.* 1987, 1988). The $B-V$ color of SN 2004dj qualitatively corresponds to the lower envelope of the SN IIP colors, suggesting that the total reddening of the supernova cannot exceed appreciably the adopted value, $E(B-V)=0.062$. On the other hand, based on the population synthesis of the spectrum for S96, Wang *et al.* (2005) concluded that the reddening for the cluster is $E(B-V)\sim 0.35$. The contradiction can be resolved if the light from S96 is reddened in a cold shell around this cluster, while the supernova lies outside the shell, closer to the observer.

The $V-R$ color for SN 2004dj (Fig. 2, the inset) near day 150 is almost $0^m.3$ lower than that for SN 1987A. However, the $V-R$ color difference between these supernovae decreases with time and disappears near day 200. This indicates that the spectral energy distributions (SED) for both supernovae in the long wavelength range ($\lambda > 5000$ Å) at $t \geq 200$ days are similar. This fact proves to be important for the photometric estimation of the ^{56}Ni mass in SN2004dj.

The ^{56}Ni mass in the envelope can be found by comparing the absolute magnitudes M_V of SN 2004dj and SN 1987A at the early nebular epoch ($t < 250$ days), when the envelope is still optically thick for gamma rays, and, hence, the entire energy of the radioactive ^{56}Co decay is reradiated almost instantaneously by the envelope in the optical range. The method assumes that the distance to the supernova and the reddening in our Galaxy and the host galaxy are known and that the bolometric correction to the V magnitude is the same for both supernovae. At first glance, the latter assumption is in conflict with the apparent $B-V$ color difference between SN 2004dj and SN 1987A. However, it should be kept in mind that the bulk of the energy at the nebular epoch is emitted in the long wavelength range ($\lambda > 5000$ Å), in which the SEDs for both supernovae are similar at $t \geq 200$ days, as suggested by the similarity of their $V-R$ colors (Fig. 2). Thus, using SN 1987A as a template, we can determine the ^{56}N mass in SN 2004dj from the V light curve near day 200.

Fitting the V light curve for SN 2004dj (Fig. 1) yields the apparent magnitude $V = 15^m.32$ on day 200. With the reddening $E(B-V)=0.062$ and the standard extinction law (Seaton 1979), the absorption is $A_V = 0.19$. In this case, with the distance modulus $\mu = 27.48$ for NGC 2403, the absolute magnitude on day 200 is $M_V = -12.48$. On the other hand, $V = 5.09$ for SN 1987A at this epoch (Catchpole *et al.* 1988). At an assumed distance to SN 1987A of $D = 50$ kpc and absorption $A_V = 0.6$, we obtain $M_V = -14.01$ on day 200. Thus, on day 200, SN 1987A is brighter in the V band than SN 2004dj by $\Delta V = 1.53$. Consequently, with the ^{56}Ni mass of $0.075 M_\odot$ in the SN 1987A envelope (Suntzeff and Bouchet 1991), we estimate the ^{56}Ni mass in SN 2004dj to be $M(^{56}\mathrm{Ni}) \approx 0.02\ M_\odot$.

The uncertainty in the ^{56}Ni mass estimated from the V light curve related to the error in the distance (Freedman *et al.* 2001) is 20%. The uncertainty in the ^{56}Ni mass related to the extinction is unlikely to exceed 10%, given the low reddening for SN 2004dj suggested by its extremely blue $B-V$ color. The possible difference between the bolometric corrections for SN 2004dj and SN 1987A can also contribute to the error in the ^{56}Ni mass. As a result, the error in the photometric ^{56}Ni mass estimate is probably ~30%.

Independently, the ^{56}Ni mass can be estimated using an empirical relation between the ^{56}Ni mass and the parameter $S = dV/dt$, which characterizes the maximum steepness of the V light curve when passing from the plateau to the tail (Elmhamdi *et al.* 2003b). For SN 2004dj, we found $S = 0.17 \pm 0.04\ ^m\ \mathrm{day}^{-1}$. Using this empirical relation, we obtained $M(^{56}\mathrm{Ni}) = 0.013 \pm 0.004 M_\odot$, which agrees, within the error limits, with the value found above from the light curve.

4. THE SPECTRUM AND ITS EVOLUTION

4.1. Qualitative Analysis

All the observed spectra of SN 2004dj are presented in Fig. 3. The last two spectra (Table 2) were combined into a single spectrum, since the spectrum at this epoch evolves slowly. In general, the appearance and evolution of the spectra for SN 2004dj are similar to those for ordinary SN IIP at the nebular epoch. The late spectra are dominated by the Hα, [O I] 6300, 6364 Å, and [Ca II] 7291, 7324 Å emission lines against the background of a relatively weak quasi-continuum. The quasi-continuum is generally believed to be formed by the emission of numerous metal lines, mostly Fe II, that arises mainly from the fluorescence of ultraviolet photons generated in the central parts of the envelope through the energy reprocessing of the radioactive decay (Xu and McCray 1991). The scattering (absorption) of the quasi-continuum emission in metal and hydrogen lines in the outer layers of the envelope gives rise to broad P Cygni profiles, such as, e.g., Hβ, Fe II lines of the 42nd multiplet, or the Na I doublet (Fig. 3).

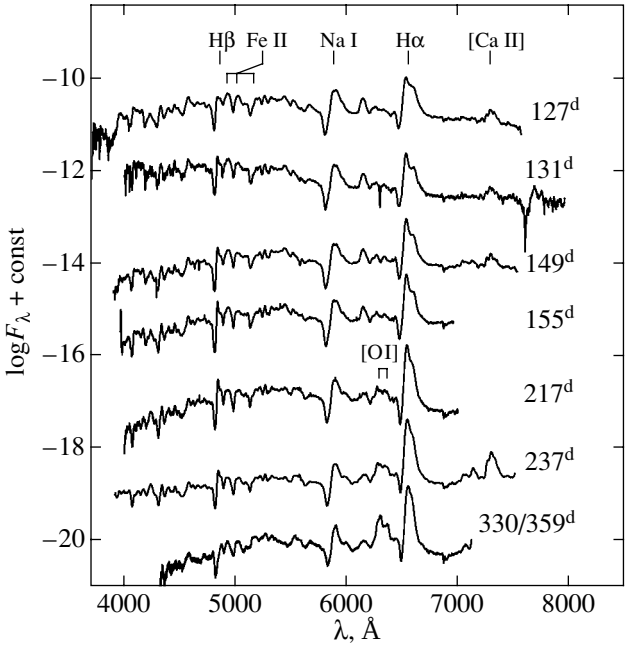

Fig. 3. Spectra of SN 2004dj at different times and the identification of major features. The wavelength was corrected for the redshift of the galaxy. The time (in days) next to the spectra is counted off from the explosion date (June 13, 2004).

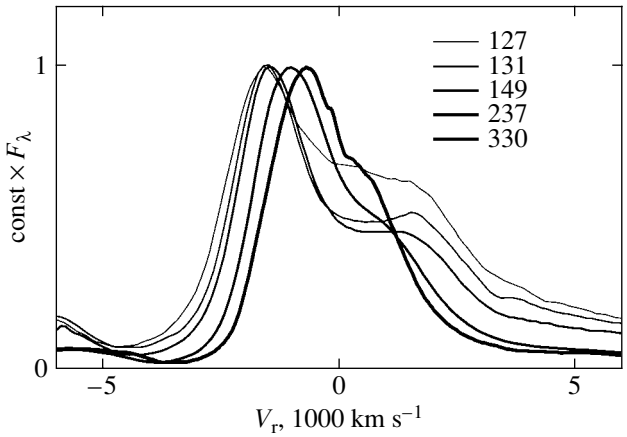

Fig. 4. Evolution of the Hα line in the spectra of SN 2004dj. The age (in days) is indicated next to the line of the corresponding width.

A prominent feature in the spectra of SN 2004dj that has not yet been observed in SN IIP is the significant blueshift of the emission line maxima, which is particularly clearly seen in Hα (Fig. 4). The profile of this line is asymmetric, and its maximum is shifted by -1600 km s^{-1} in the early (127 and 131 days) spectra. Remarkably, on day 131, the Hα profile exhibits a double-peaked structure with a distinct, but much weaker, red peak shifted by $\approx$1600 km s^{-1}. This profile points to a bipolar, asymmetric structure of the hydrogen excitation in the envelope. The absolute value of the blueshift, along with the line FWHM, decreases with time. The blueshift of the peak on day 330 is -600 km s^{-1}. The blue peak is also present in Hβ (Fig. 3), although it is much weaker due to the low intensity of the Hβ emission.

Previously, only two cases of significant Hα asymmetry were noted among type IIP supernovae: SN 1987A (Phillips and Williams 1991) and SN 1999em (Elmhamdi *et al.* 2003a). In both supernovae, the peak was redshifted. The redshift in SN 1987A was interpreted as being the result of a predominant ^{56}Ni ejection in the far hemisphere in an otherwise spherically symmetric envelope (Chugai 1991). The redshift of the Hα and He I 10830 Å lines in SN 1999em was interpreted in a similar way (Elmhamdi *et al.* 2003a). It would be natural to assume that the Hα asymmetry in SN 2004dj is also due to an asymmetric ^{56}Ni ejection, with the only difference that in this case ^{56}Ni is predominantly ejected in the near hemisphere.

Figure 5 gives an idea of the line asymmetry in SN 2004dj and two other supernovae. This figure shows Hα and the [Ca II] doublet in SN 2004dj on day 149, SN 1987A on day 198 (Phillips and Williams 1991), and SN 1999em on day 140 (Elmhamdi *et al.* 2003a). SN 2004dj surpasses the other two supernovae in shift and intensity of the asymmetric Hα component. The [Ca II] doublet in SN 2004dj also differs significantly from that in the other supernovae (Fig. 5). In particular, SN 2004dj exhibits a characteristic peak in [Ca II] with a shift of -1600 km s^{-1}, which was also seen in Hα. This blue peak in Ca II probably reflects the local overexcitation related to the asymmetry of ^{56}Ni ejecta, like that in Hα.

Remarkably, Hα in SN 1999em, like that in SN 2004dj, shows evidence of a bipolar structure of the Hα excitation. More specifically, a blue peak of lower amplitude with a shift of about -600 km s^{-1} (Fig. 5) is present in addition to the red peak in the line. Moreover, a weak blue peak with a shift of ≈ -600 km s^{-1}, the same as that for the blue peak in Hα, is also present in the [Ca II] doublet of SN 1999em. Thus, at least in two supernovae (SN 2004dj and SN 1999em), we see clear evidence of an asymmetric bipolar structure of the excitation in the envelope, which is probably related to the bipolar asymmetric ^{56}Ni ejection.

There are also other differences between the spectra of SN 2004dj and SN 1999em that may be related to different signs of the asymmetry in these supernovae. In particular, the absorption component

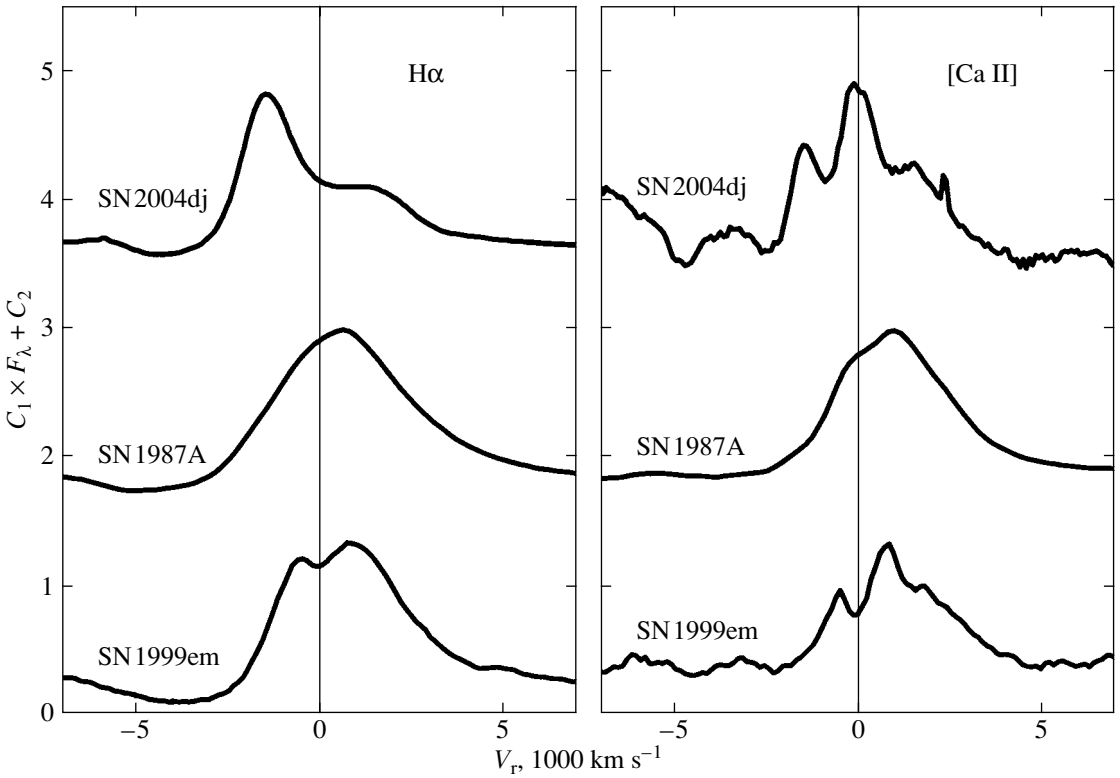

Fig. 5. Hα line and the [Ca II] doublet in the spectrum of SN 2004dj on day 149, in the spectrum of SN 1987A on day 198, and in the spectrum of SN 1999em on day 140. The radial velocity in the 7291 Å line is indicated for [Ca II].

of Hα in SN 2004dj is appreciably weaker than that in SN 1999em (Fig. 6). This is most likely attributable to the presence of a blue emission peak that fills the Hα absorption component in the spectrum of SN 2004dj. In contrast, the absorption component of Hβ in SN 2004dj is stronger than that in SN 1999em. The reason is probably the same: the predominant ^{56}Ni ejection toward the observer. This presumably causes stronger hydrogen excitation in the near hemisphere of SN 2004dj owing to radioactive ^{56}Co decay than that in SN 1999em where most of ^{56}Ni is shifted toward the far hemisphere. As a result, the Sobolev optical depth in Hβ in the near hemisphere of SN 2004dj is larger than that in SN 1999em.

The spectra of SN 2004dj at the plateau epoch (Korcakova *et al.* 2005) exhibit fairly high velocities of the Hα absorption minimum compared to SN 1999em at the corresponding phases. On JD 2453221 (day 51 in the chosen age scale), the radial velocity of the Hα absorption minimum in SN 2004dj is −6955 km s^{-1} (Korcakova *et al.* 2005) compared to −5000 km s^{-1} in SN 1999em on day 54 (Elmhamdi *et al.* 2003a). We are convinced that the higher velocity in SN 2004dj reflects the stronger hydrogen excitation in the near hemisphere of SN 2004dj due to the asymmetric ^{56}Ni distribution rather than the higher energy-to-mass (E/M) ratio, which leads to an extension of the Hα line formation region through the higher-velocity outer layers.

Note the difference between the quasi-continuum shapes in the range 5000–5700 Å in the spectra of both supernovae (Fig. 6). Interestingly, the quasi-continua in SN 1999em and SN 1987A are almost identical. It may well be that different signs of the ^{56}Ni asymmetry in SN 2004dj and SN 1999em are also responsible for the difference between their quasi-continua. Indeed, the ^{56}Ni displacement from the envelope center would lead to different optical depths in the "fence" of metal lines and, hence, to dissimilar spectra of the emergent radiation in the asymmetric hemispheres.

4.2. The Hα *Luminosity and the* ^{56}Ni *Mass*

The integrated Hα flux was determined from the spectra that could be calibrated relatively reliably. The flux was calibrated using V and Rc photometric data, which were compared with the V and Rc magnitudes calculated from the observed spectra with the transmission function of the V and Rc filters. The Hα fluxes derived from the V and Rc calibrations were averaged. We excluded the spectra on days 131 and

Table 3. Hα flux and luminosity

Date	t, days	F, erg s^{-1}	$F^{\rm corr}$, cm^{-2}	L, erg s^{-1}
Oct. 18, 2004	127	2.37×10^{-12}	2.72×10^{-12}	3.19×10^{39}
Nov. 9, 2004	149	1.82×10^{-12}	2.09×10^{-12}	2.45×10^{39}
Nov. 15, 2004	155	1.84×10^{-12}	2.12×10^{-12}	2.49×10^{39}
Jan. 16. 2005	217	2.27×10^{-12}	2.61×10^{-12}	3.07×10^{39}

237, which are strongly affected by the atmospheric dispersion, and the spectrum on day 330, which cannot be calibrated reliably, because the contribution of the [Ca II] emission to the *Rc* filter is large at this epoch, as can be judged from the spectra of SN 1999em (Elmhamdi *et al.* 2003a). The derived Hα fluxes, uncorrected (F) and corrected ($F^{\rm corr}$) for the Galactic absorption, are presented in Table 3. The last column gives the Hα luminosity. Half of the maximum difference between the logarithms of the fluxes derived from the V and *Rc* calibrations can be taken as the typical relative error in the flux. The error determined in this way is 0.12 dex.

The Hα luminosity at the nebular epoch can be used to estimate the ^{56}Ni mass in the envelope of SN 2004dj, as was done previously for SN IIP (Elmhamdi *et al.* 2003b). The method suggests calculating the Hα luminosity in the model of nonthermal ionization and hydrogen excitation under the effect of gamma rays from the radioactive decay ^{56}Co–^{56}Fe with allowance made for the photoionization from excited levels. A three-level hydrogen atom with a continuum is considered, although the recombination to excited levels followed by cascade transitions downward are included. The radiative transfer in the continuum is treated in the escape probability approximation (Chugai 1987). Of course, the ^{56}Ni mass estimate in this case depends on the chosen model envelope. The two-zone model envelope consists of a macroscopically mixed core and an outer hydrogen envelope. The model parameters include the mass M, the kinetic energy E, the ^{56}Ni mass, the supernova mass fraction in the core $f_{\rm mix}$, and the mass fraction of the core in the form of metals and helium $f_{\rm m}$. The quasi-continuum is described by a diluted blackbody radiation with a color temperature $T_{\rm c}$. In contrast to the previous version of the model (Elmhamdi *et al.* 2003b), the electron temperature $T_{\rm e}$ here is calculated from the thermal balance equation, which includes the cooling in Ca II, Mg II, Fe II (approximately), O I lines, the ff-emission, and the adiabatic cooling. We abandon the approximation of a uniform density and assume that the density in the inner zone (the core) of the model is a factor of 3 higher than that in the outer zone (the envelope). This mimics the density decrease outward in SN IIP.

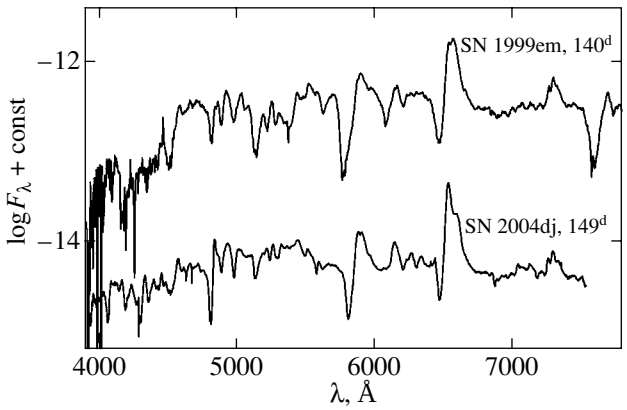

Fig. 6. Spectra of SN 2004dj and SN 1999em at close phases. The marked difference between the line profiles and the quasi-continuum behavior near 5600 Å is clearly seen.

The model includes the result of the macroscopic ^{56}Ni mixing in the envelope of the exploding massive star with a stratified chemical composition. The ^{56}Ni fragments are assumed to be surrounded by cocoons composed of metals and helium, i.e., a material without hydrogen. The optical depth of the cocoon for gamma rays is determined by its mass and surface area, $\tau_{\rm c} = kf_{\rm m}f_{\rm mix}M/(4\pi f_{\rm s}R_1^2)$, where $k = 0.03(1+X)$ cm^2 g^{-1} is the absorption coefficient for gamma rays (Fransson and Chevalier 1989), X is the hydrogen mass fraction, R_1 is the radius of the mixed core, and $f_{\rm s}$ is the mixing parameter. The latter is the ratio of the cocoon surface area to $4\pi R_1^2$. Below, we present our results for $f_{\rm s} = 2$ (moderate mixing) and $f_{\rm s} = 20$ (strong mixing).

The envelope mass in the model is $M = 13\ M_\odot$; the mass of the envelope of SN 1999em (Nadyozhin 2003), which corresponds to a main-sequence star of $15M_\odot$. The kinetic energy is $E = 10^{51}$ erg, a typical value for SN IIP (Nadyozhin 2003). The remaining parameters are $f_{\rm mix} = 0.4$ and $f_{\rm m} = 0.3$, i.e., $\approx 1.56M_\odot$ of the core is contained in the form of metals and helium. From a few tenths to one solar

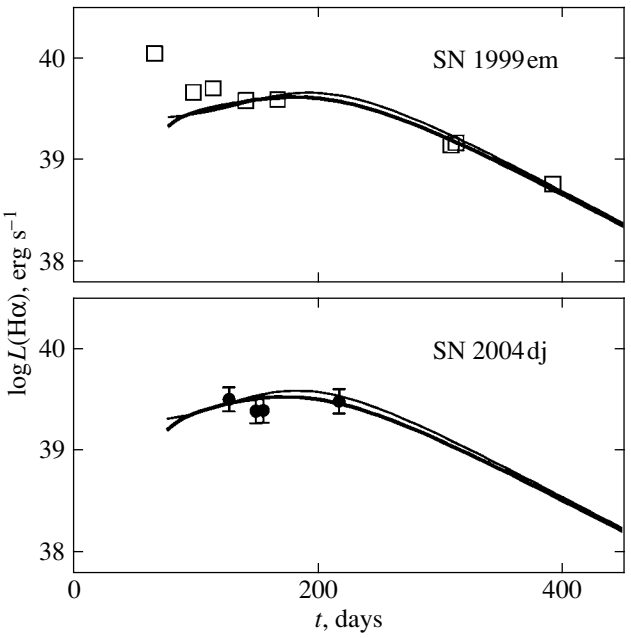

Fig. 7. Models for the evolution of the Hα luminosity in SN 1999em and SN 2004dj. The data for SN 1999em (squares) were taken from Elmhamdi *et al.* (2003b). The model for SN 1999em suggests a ^{56}Ni mass of $0.027\,M_\odot$ and two mixing parameters, $f_s = 2$ (thick line) and $f_s = 20$ (thin line). The model of SN 2004dj was computed for the same parameters as those for the model of SN 1999em, but the ^{56}Ni mass is $0.02M_\odot$.

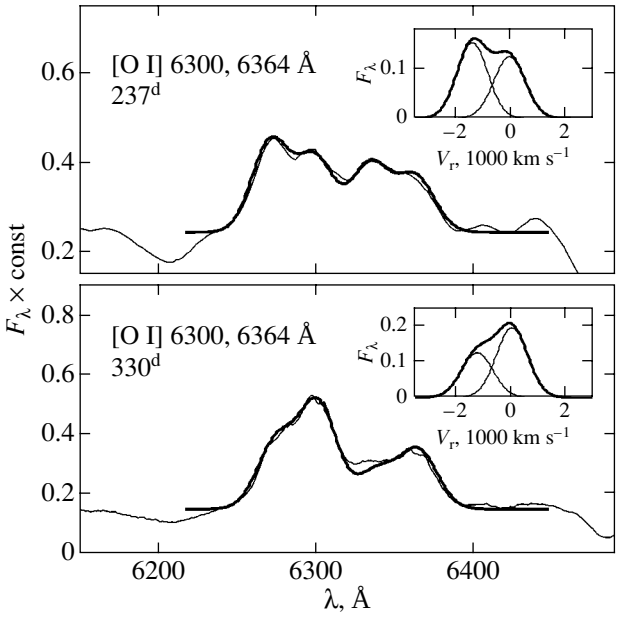

Fig. 8. Reconstruction of the [O I] 6300, 6364 Å doublet line profile in the spectrum of SN 2004dj on days 237 and 330: the thick and thin lines represent the model and the observations, respectively. The inset shows the model line profile (thick line) together with the Gaussian components with which this profile was synthesized.

helium mass is presumably mixed with hydrogen. For a star with an initial mass of $M \approx 15M_\odot$, the mass of the synthesized metals and helium in the supernova envelope is close to $3M_\odot$ (Woosley and Weaver 1995), consistent with our assumptions about the mass of the helium and metals.

The optimal models of the Hα luminosity for SN 1999em at the nebular epoch, $t \geq 130$ days, are presented in Fig. 7 for two values of the mixing parameter f_s under the assumption that the ^{56}Ni mass is equal to the value obtained from the tail of the V light curve (Elmhamdi *et al.* 2003b), i.e., $M(^{56}\mathrm{Ni}) = 0.027M_\odot$. The color temperature of the quasi-continuum is the only free parameter that was used for model fitting. Its values are $T_c = 5500$ K and $T_c = 5000$ K for the models with $f_s = 2$ and $f_s = 20$, respectively.

This model envelope for two values of f_s was also used to compute the evolution of the Hα luminosity at the epoch $t > 130$ days in SN 2004dj (Fig. 7). In this case, the ^{56}Ni mass was taken to be $M(^{56}\mathrm{Ni}) = 0.02M_\odot$, the value obtained from the V light curve. Figure 7 shows that the model of the Hα luminosity for this ^{56}Ni mass is in satisfactory agreement with the observational data, within the error limits. This does not prove that the ^{56}Ni mass is $\approx 0.02M_\odot$, since other parameters of SN 2004dj are rather uncertain. At the same time, this suggests that the ^{56}Ni mass inferred from the V light curve qualitatively agrees with the Hα luminosity.

5. THE LINE ASYMMETRY AND THE ^{56}Ni DISTRIBUTION

The line profile formed in a supernova envelope with homologous expansion kinematics ($v = r/t$) depends on the level population distribution and the quasi-continuum optical depth. At the nebular epoch, the absorption in the "fence" of metal lines plays a significant role in the blue ($\lambda < 5000$ Å) and, particularly, ultraviolet spectral ranges. However, the role of absorption is minor in the red spectral range. Thus, the profiles of the Hα, [O I] 6300, 6364 Å and [Ca II] 7291, 7324 Å emission lines contain information about the asymmetry of the radiation sources throughout the envelope, including the central zone.

5.1. The [O I] 6300, 6364 Å Lines

Since the lines in the [O I] and [Ca II] doublets partially overlap, it is appropriate to reconstruct the true line profiles by representing each line as a superposition of the minimum number of Gaussians. Each

Table 4. Parameters of the components of the [O I] and [Ca II] doublet lines

Doublet	Epoch	Component	V_r, km s^{-1}	w, km s^{-1}	A	R
[O I]	237	1	−1380	730	1.55	1.33
[O I]	237	2	−30	750	1.21	1.33
[O I]	330	1	−1200	750	1.2	1.8
[O I]	330	2	60	750	1.9	1.8
[Ca II]	149	1	−1500	440	9.5	1.1
[Ca II]	149	2	200	1300	0.53	1.1
[Ca II]	237	1	−1270	470	8.8	1.3
[Ca II]	237	2	200	1300	1.3	1.3

Gaussian line component is described by its radial velocity V_r, Doppler width w, and relative amplitude A.

The [O I] 6300, 6364 Å doublet is the most convenient case for a Gaussian decomposition, because the doublet lines overlap only slightly due to the large velocity interval between the lines (3000 km s^{-1}). Using only two Gaussian components, the central and blueshifted ones, we are able to describe satisfactorily the [O I] doublet profile on days 237 and 330 (Fig. 8). Parameters of the components (their shift, width, and amplitude) are given in Table 4. It should be kept in mind that the table actually lists the relative amplitudes of the components. The [O I] line profile on day 237 resembles the Hα profile at the same epoch (Fig. 4), but the difference on day 330 is significant: the [O I] maximum is at zero, while the Hα maximum is blueshifted by ≈ -700 km s^{-1}. This probably reflects the fact that the hydrogen and oxygen distributions in the envelope are essentially different.

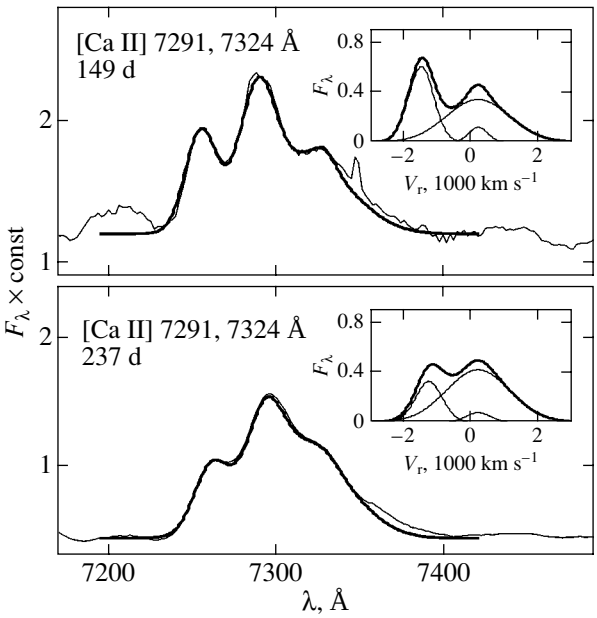

Fig. 9. Reconstruction of the [Ca II] 7291, 7324 Å doublet line profile in the spectrum of SN 2004dj on days 149 and 237. The thick and thin lines represent the model and the observations, respectively. The inset shows the model line profile (thick line) together with the Gaussian components with which this profile was synthesized.

The increasing role of the central component in the [O I] line between days 237 and 330 can be explained in terms of a picture that includes two (central and blueshifted) ^{56}Ni components. The central ^{56}Ni component is presumably surrounded by an absorbing cocoon that is optically thick for gamma rays and that does not contribute appreciably to the [O I] doublet luminosity. The cocoon can even be composed of an oxygen-rich material (O/C or O/Si/Ne/Mg) and yet be unseen in the [O I] lines. The reason is that CO and/or SiO molecules can be formed in it; these efficiently cool down the oxygen material, so its contribution to the [O I] doublet emission is minor (Liu and Dalgarno 1995). As the envelope expands, the cocoon becomes optically thin and gamma rays penetrate into the outer oxygen material, causing a relative enhancement of the central component in the [O I] line. This effect in Hα is studied below (see Section 5.3).

To decompose the oxygen doublet profile, we used a doublet ratio of $R = I(6300)/I(6364)$. The latter is equal to the ratio of the specific line luminosities $h\nu_{ik} n_k A_{ki} \beta_{ik}$ [erg s^{-1} cm^{-3}], where β_{ik} is the Sobolev photon escape probability, while the meaning of the remaining quantities is obvious. The optimal R values (Table 4, the last column) are appreciably lower than the nebular value of $R = 3$, as in other SN IIP (Spyromilio and Pinto 1991; Chugai 1988). The doublet ratio is determined mainly by the oxygen number density and depends weakly on the electron temperature T_e, since the excitation potential of the lower level of the 6364 Å transition is only 0.02 eV. Since oxygen is mostly neutral, the ratio R allows the mean oxygen

number density $n(\mathrm{O})$ in the [O I] doublet formation zone to be determined. The observed value of $R = 1.33$ on day 237 corresponds to the oxygen number density $n(\mathrm{O}) = 6.63 \times 10^9 (237\ \mathrm{d}/t)^3\ \mathrm{cm}^{-3}$, where t is in days and $T_\mathrm{e} = 5000$ K. Given these values and the density evolution $n(\mathrm{O}) \propto t^{-3}$, the extrapolated ratio on day 330 is $R = 1.77$, in good agreement with $R = 1.8$ found from observations (Table 4). This confirms that the adopted explosion date of SN 2004dj is valid, although the accuracy of reconstructing the explosion date from the R evolution is low, ± 30 days.

5.2. The [Ca II] 7391, 7324 Å Lines

The [Ca II] doublet lines can also be represented by two Gaussian components, the central and blueshifted ones (Fig. 9, Table 4). However, the broad central component shows a small deviation from the Gaussian shape, which requires introducing an additional, weak narrow component (see the inset in Fig. 9). On day 237, for which the [Ca II] and [O I] doublets can be compared, the line profiles are similar, although there are differences. In particular, the blue component of [Ca II] exhibits almost the same shift as that for [O I], but it is a factor of 1.6 narrower. In contrast, the central component of [Ca II] is a factor of 1.7 broader than that of [O I]. Another difference is that the mean radial velocity of the [Ca II] line (e.g., 7291 Å) is -149 km s^{-1} on day 237, i.e., lower than that of the [O I] line at the same epoch (-770 km s^{-1}).

These differences probably stem from the fact that the [Ca II] and [O I] lines originate in different zones. Indeed, models for the evolution of massive stars (e.g., 15 $M_\odot$) and supernova models predict that Ca is synthesized via two processes: static oxygen burning in the presupernova core and explosive oxygen burning during the shock propagation (Woosley and Weaver 1995). Therefore, the synthesized calcium is expected in the oxygen burning products (Si/S matter) and the explosive nucleosynthesis products (iron-peak elements), not in the oxygen material. The [Ca II] 7391, 7324 Å lines can also be formed in the hydrogen or helium material (Li and McCray 1993) with the main-sequence abundance.

Given the uncertainty in choosing the [Ca II] doublet line formation region, it is interesting that the doublet ratio on day 149 is $R = I(7291)/I(7324) \approx 1.1$, i.e., smaller than the nebular one ($R = 1.5$). If this is interpreted as the optical depth effect in the [Ca II] 7391, 7324 Å lines, then the required Ca number density in the line formation region is estimated to be $n(\mathrm{Ca}) > 3.6 \times 10^6 (149\ \mathrm{d}/t)^3\ \mathrm{cm}^{-3}$. If the [Ca II] doublet is emitted by the hydrogen material at a normal Ca abundance, then the required density of the hydrogen material in the [Ca II] line emission region is $\rho > 3.7 \times 10^{-12} (149\ \mathrm{d}/t)^3\ \mathrm{g\ cm}^{-3}$. This can be compared with the oxygen density found from the oxygen doublet ratio, $\rho \approx 7 \times 10^{-13} (149\ \mathrm{d}/t)^3\ \mathrm{g\ cm}^{-3}$. The latter turns out to be at least a factor of 5 lower than the required density of the hydrogen material. In reality, the reverse must be true, since analysis of SN 1987A shows that oxygen is distributed in dense condensations with a filling factor of $f \sim 0.1$ (Spyromilio and Pinto 1991; Chugai 1994). Thus, the hypothesis of the [Ca II] doublet formation in the hydrogen material runs into difficulties. At the same time, given the uncertainty in the quasi-continuum shape in the [Ca II] doublet band, we may have underestimated the doublet ratio R. For this reason, we do not yet rule out the formation of the [Ca II] doublet in the hydrogen material, although this possibility raises doubts.

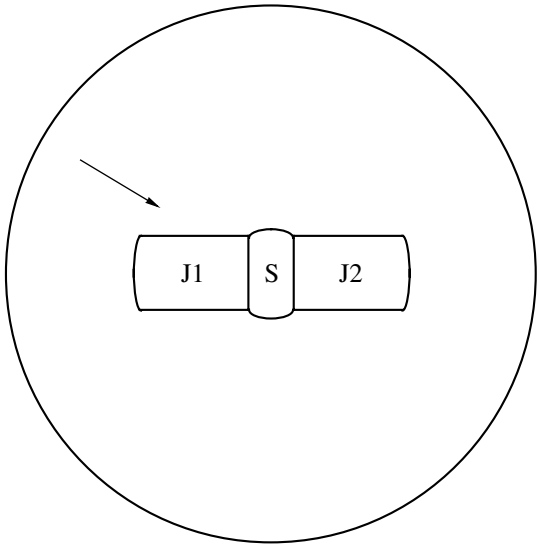

Fig. 10. Schematic representation of the spherical envelope of SN 2004dj with a bipolar ^{56}Ni distribution. The ^{56}Ni distribution includes the central spherical component S and two cylindrical jets, J1 and J2. The arrow indicates the line of sight.

5.3. Modeling the Hα *Asymmetry*

Here, we are interested in the shape of the Hα line profile and its relationship to the structure of the ^{56}Ni distribution in the asymmetric model. We will not describe in detail the energy cascade processes leading to the Hα emission, but assume that the specific Hα luminosity, $\eta = Ch\nu_{23} n_3 A_{32} \beta_{23}$, is proportional to the local energy deposition rate of the radioactive decay, ϵ_d, with a constant proportionality factor C. In this case, to calculate the Hα line profile, it will suffice to specify the ^{56}Ni distribution and to calculate the distribution of the deposition rate ϵ_d in the envelope.

The gamma-ray transfer is computed in the single-flight approximation with the absorption coefficient adopted above (Section 4.2).

We assume the envelope to expand homologously ($v = r/t$), the mass (except ^{56}Ni) to have a spherical distribution, and the density to be distributed in velocity as $\rho = \rho_0 \exp(-v/v_0)$, where $\rho_0 \propto t^{-3}$. The exponential law is acceptable for describing the density distribution of the bulk of the envelope where the index $|d\ln\rho/d\ln v|$ monotonically increases with velocity (see, e.g., Utrobin 2004). The parameters ρ_0 and v_0 in this law are determined by the mass M and the kinetic energy E. We assume, as in the case of modeling the evolution of the Hα luminosity, that $M = 13M_\odot$ and $E = 10^{51}$ erg.

We will describe the ^{56}Ni distribution by three components: a central homogeneous sphere of radius $v_s t$ and two cylindrical jets with the angle θ between the jet axis and the line of sight (Fig. 10). In the regions where the jets and the central spherical component overlap, the ^{56}Ni density is assumed to be equal to the jet density. The opposite case yields slightly poorer agreement with the observations. The ^{56}Ni density in the jets is assumed to decrease linearly outward along the axis to zero at the outer jet boundary. The chemical composition of the envelope is taken to be homogeneous with the hydrogen abundance $X = 0.7$, except in the central zone with a radius of $R_s = v_s t$ where the filling factor of the hydrogen material is assumed to decrease linearly with depth from unity at the boundary of the central zone to zero at the center. This assumption is qualitatively consistent with the expected result of the mixing of helium and metals with the hydrogen envelope.

Our analysis of the model parameter space shows that only the model with a cocoon around the ^{56}Ni-containing material can satisfactorily represent the evolution of the Hα profile. The cocoon model has already been used above to describe the evolution of the Hα luminosity. Here, this model should be refined, given the more complex mixing geometry. We assume that ^{56}Ni is distributed in the form of an ensemble of spherical fragments, each surrounded by a cocoon with an optical depth τ_c for gamma rays. The mean gamma-ray emissivity should be multiplied by the attenuation factor $\exp(-\tau_c)$. We assume that the optical depth of the cocoon in the central zone of radius R_s is constant, $\tau_c = \tau_o = \text{const}$, while in the jets outside the central zone, the cocoon optical depth decreases with increasing velocity v as

$$\tau_c = \tau_0 \left(\frac{v_k - v}{v_k - v_s}\right)^p, \qquad (1)$$

where v_k is the velocity the k-th jet ($k = 1, 2$) at the outer boundary. The optimal power index is $p = 3$. It is convenient to express the parameter τ_0 in terms of the cocoon mass M_c, $\tau_0 = kM_c/4\pi f_s R_s^2$, where f_s is the mixing parameter introduced above (Section 4.2). The decrease in τ_c outward corresponds to the increase in the mixing parameter outward. This is also expected from the mixing physics: a material that passed through a larger mass would undergo stronger mixing with the surrounding matter.

Parameters of the optimal model, specifically, the angle θ between the line of sight and the jet axis, the expansion velocity of the central component v_s, the boundary velocities of the jets in the near and far hemispheres (v_1, and v_2), the masses of the jets in the near and far hemispheres in mass fractions of the central component, and the cocoon mass M_c for the moderate mixing parameter ($f_s = 2$), are given in Table 5. The accuracy of determining the velocities and the angle θ is ~20% and ~10°, respectively. Note that the model for the evolution of the Hα luminosity does not impose stringent constraints on f_s, while here we found that the cocoon mass $M_c \sim 1M_\odot$ suggests a moderate mixing, $f_s \sim 2$.

The model Hα profiles for three epochs in the models with and without the absorbing cocoon are compared with the observations in Fig. 11. Clearly, the model with the absorbing cocoon describes much better the profile structure and evolution in the period 131–330 days. We emphasize that the complex transformation of the profile from an asymmetric double-peaked profile on day 131 through a plateau-type profile with a blue peak on day 149 to a smooth asymmetric profile with a blueshifted maximum can be described in terms of a single model.

The characteristic features of the derived ^{56}Ni distribution include the bipolar structure and the significant deviation from the point symmetry. The mass of the jet directed toward the observer is comparable to the mass of the central component and twice as large as the mass of the jet in the far hemisphere (Table 5). Note that there is no need to assume an asymmetry of the hydrogen distribution. Otherwise, the degree of asymmetry of the supernova envelope would be very high.

The one-dimension projection of the derived ^{56}Ni distribution onto the line of sight and the jet axis is shown in Fig. 12. For comparison, the figure shows the reconstructed [Ca II] 7291 Å line profile on day 149 (Fig. 9), when the gamma-ray transfer effect is small, and, therefore, the sources in the [Ca II] lines follow the ^{56}Ni distribution. While the presented profiles are generally similar, there are marked differences. The projection of the ^{56}Ni distribution onto the line of sight does not show such a strong central peak as that in the [Ca II] doublet lines on day 149. This

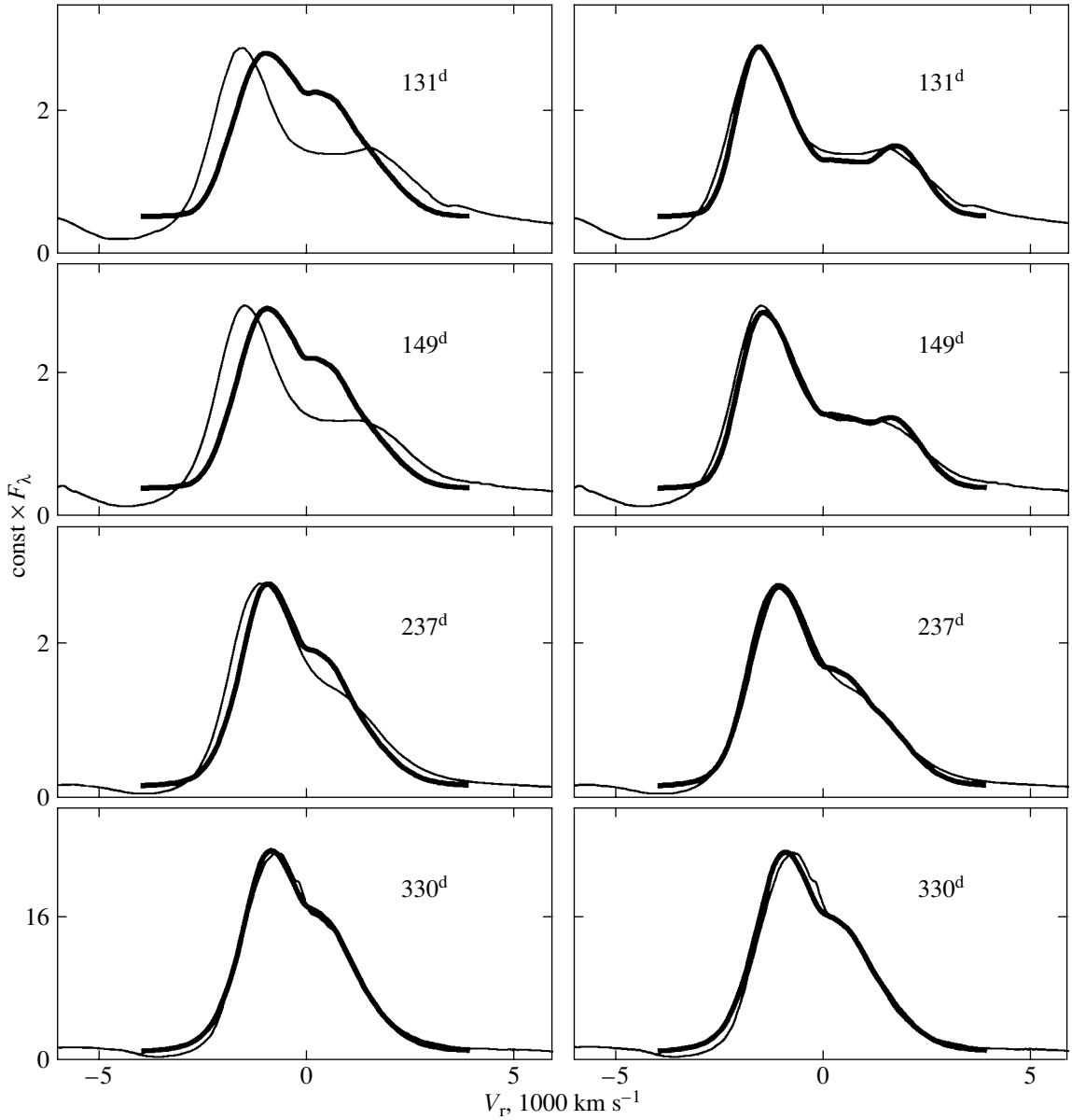

Fig. 11. Models for the Hα profile in the spectrum of SN 2004dj for the asymmetric bipolar ^{56}Ni distribution: the thick and thin lines represent the model and the observations, respectively. The models of the ^{56}Ni distribution without a cocoon (left panels) and with a cocoon that is partially opaque for gamma rays (right panels) are shown.

indicates that the Ca distribution deviates appreciably from the ^{56}Ni distribution.

An interesting result of our modeling is that the bulk of the ^{56}Ni mass should be separated from the hydrogen material by a cocoon, i.e., by a layer of material without hydrogen; the degree of ^{56}Ni mixing should not be large, i.e., the cocoon should be optically thick. A similar property of the ^{56}Ni distribution was found previously by Liu and Dalgarno (1995) when interpreting the CO 2.3 μm emission in SN 1987A. To reconcile the model with the observations, they introduced an attenuation factor for gamma-rays that decreased with time. In our view, this factor reflects the existence of cocoons around the ^{56}Ni fragments in SN 1987A.

Table 5. Parameters of the ^{56}Ni distribution

θ	v_s	v_1	v_2	M_1/M_s	M_2/M_s	M_c, $M_\odot$
	km s^{-1}					
30°	1400	2700	3500	1.07	0.49	1.3

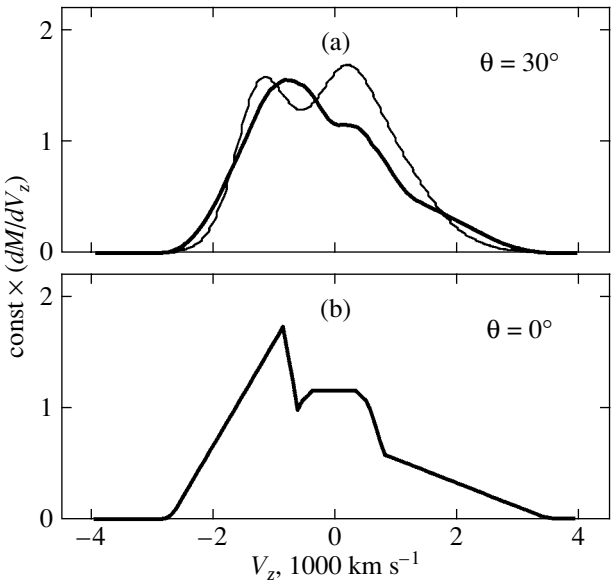

Fig. 12. ^{56}Ni distribution along the radial velocity in SN 2004dj: (a) the ^{56}Ni distribution in projection onto the line of sight (thick line) together with the model [Ca II] 7291 Å line profile (thin line) on day 149 (Fig. 9); (b) the ^{56}Ni distribution along the jet axis.

6. DISCUSSION AND CONCLUSIONS

We presented our photometric and spectroscopic observations of SN 2004dj, an ordinary type IIP supernova. We estimated the ^{56}Ni mass in the envelope by comparing the V light curves of SN 2004dj and SN 1987A at the nebular epoch and by modeling the Hα luminosity. Both estimates suggest that the ^{56}Ni mass in the envelope of SN 2004dj is $\approx$0.02 $M_\odot$. This value is a factor of 3.8 lower than that in SN 1987A and is comparable to the ^{56}Ni mass in SN 1999em (0.02–0.027 $M_\odot$, Elmhamdi *et al.* 2003a, 2003b).

The most important result of our spectroscopic study of SN 2004dj is the detection of a strong blueshift of the Hα line, which is interpreted as being the result of an asymmetric ^{56}Ni ejection in a spherically symmetric envelope. Our modeling of the Hα line profile shows that the profile structure and evolution are well reproduced in the model of asymmetric bipolar ^{56}Ni ejecta with a jet mass ratio of two and comparable masses of the massive jet and the central component.

We also found signatures of the bipolar structure in the Hα and [Ca II] lines of SN 1999em, indicating that the asymmetric bipolar ^{56}Ni ejection is not an exceptional phenomenon for SN IIP. Although there are no clear manifestations of the bipolar structure in SN 1987A, Wang *et al.* (2002) see signatures of the bipolar structure in the HST images of SN 1987A. The detection of a bipolar structure of the ^{56}Ni ejecta at least in two normal SN IIP suggests that a bipolar explosion of core-collapse supernovae can occur for a moderately rotating red supergiant core.

The significant deviation from the point symmetry in the ^{56}Ni distribution at least in three supernovae (SN 1987A, SN 1999em, and SN 2004dj) implies that the total momentum for the synthesized iron-peak elements can be nonzero in SN IIP. In this case, the finite momentum of the asymmetric ejection of iron-peak elements is presumably compensated for either by the remaining part of the envelope or by the neutron star. According to a recent study of the proper motions of pulsars (Hobbs *et al.* 2005), neutron stars at birth acquire high velocities, on average, $\sim$400 km s^{-1}. These velocities cannot be explained by the sling effect of a supernova in a close binary, so the kick of a newly born neutron star is the preferred explanation. Thus, the asymmetry of ^{56}Ni ejecta in SN IIP in combination with the high pulsar velocities is a strong argument that the explosion of core-collapse supernovae is accompanied by significant violations of the point symmetry.

At present, the main asymmetry mechanism for core-collapse supernovae is large-scale neutrino convection in the first second after the collapse (Herant *et al.* 1992; Scheck *et al.* 2004), although the ejection of the supernova envelope with the required kinetic energy of $\sim10^{51}$ erg still remains problematic for the neutrino-driven explosion mechanism (Buras *et al.* 2003).

The detection of a bipolar structure of the ^{56}Ni ejecta in normal SN IIP raises another intriguing question: can the neutrino-driven explosion mechanism produce it? This problem was recently discussed in connection with the interpretation of the bipolar ejecta in Cas A and SN 1987A (Burrows *et al.* 2005). In particular, the authors considered the possible effect of moderate rotation on the explosion asymmetry in terms of the neutrino-driven mechanism. However, it should be emphasized that both these supernovae could originate from presupernovae with relatively fast rotation: Cas A is an SN Ib/c, and the nebular ring around SN 1987A is indicative of fast rotation of the presupernova. In the case of normal SN IIP, which SN 2004dj and SN 1999em are, we deal with the cores of red supergiants that are most likely slow rotators. For this reason, it may well be that the origin of the asymmetric bipolar ^{56}Ni ejection in SN IIP bears no relation to the rotation.

ACKNOWLEDGMENTS

We are grateful to V.L. Afanasiev, N.V. Borisov, and S.S. Kaisin for help in the observations. The work was supported in part by the Russian Foundation for Basic Research (project nos. 04-02-17255, 03-02-16341, and 04-02-16349).

REFERENCES

1. V. L. Afanasiev and A. V. Moiseev, Pis'ma Astron. Zh. **31**, 193 (2005) [Astron. Lett. **31**, 194 (2005)].
2. N. V. Ardeljan, G. S. Bisnovatyi-Kogan, and S. G. Moiseenko, Mon. Not. R. Astron. Soc. **359**, 333 (2005).
3. S. I. Blinnikov, V. S. Imshennik, D. K. Nadezhin, *et al.*, Astron. Zh. **67**, 1181 (1990) [Sov. Astron. **34**, 595 (1990)].
4. R. Buras, M. Rampp, H.-Th. Janka, and K. Kifonidis, Phys. Rev. Lett. **90**, 1101 (2003).
5. A. Burrows, R. Walder, C. D. Ott, and E. Livne, in *The Fate of the Most Massive Stars,* Ed. by R. Humphreys and K. Stanek (Astron. Soc. Pac., San Francisco, 2005); Astron. Soc. Pac. Conf. Ser. **332**, 358 (2005).
6. R. M. Catchpole, J. W. Menzies, A. S. Monk, *et al.*, Mon. Not. R. Astron. Soc. **229**, 15 (1987).
7. R. M. Catchpole, P. A. Whitelock, M. W. Feast, *et al.*, Mon. Not. R. Astron. Soc. **231**, 75 (1988).
8. N. N. Chugai, Pis'ma Astron. Zh. **13**, 671 (1987) [Sov. Astron. Lett. **13**, 282 (1987)].
9. N. N. Chugai, Astron. Tsirk. **1525**, 15 (1988).
10. N. N. Chugai, Astron. Zh. **68**, 349 (1991) [Sov. Astron. **35**, 171 (1991)].
11. N. N. Chugai, Astrophys. J. **428**, L17 (1994).
12. S. A. Colgate and R. H. White, Astrophys. J. **143**, 626 (1966).
13. A. Elmhamdi, I. J. Danziger, N. N. Chugai, *et al.*, Mon. Not. R. Astron. Soc. **338**, 939 (2003a).
14. A. Elmhamdi, N. N. Chugai, and I. J. Danziger, Astron. Astrophys. **404**, 1077 (2003b).
15. C. Fransson and R. A. Chevalier, Astrophys. J. **343**, 323 (1989).
16. W. L. Freedman, B. F. Madore, B. K. Gibson, *et al.*, Astrophys. J. **553**, 47 (2001).
17. E. K. Grasberg, V. S. Imshennik, and D. K. Nadyozhin, Astrophys. Space Sci. **10**, 28 (1971).
18. M. Herant, W. Benz, and S. Colgate, Astrophys. J. **395**, 642 (1992).
19. G. Hobbs, D. R. Lorimer, A. G. Lyne, and M. Kramer, Mon. Not. R. Astron. Soc. **360**, 974 (2005).
20. D. Korcakova, Z. Mikulasek, A. Kawka, *et al.*, Int. Bull. Var. Stars **5605**, 1 (2005).
21. D. C. Leonard, A. V. Filippenko, W. Li, *et al.*, Astron. J. **124**, 2490 (2002).
22. H. Li and R. McCray, Astrophys. J. **405**, 730 (1993).
23. W. Liu and A. Dalgarno, Astrophys. J. **454**, 472 (1995).
24. D. K. Nadyozhin, Mon. Not. R. Astron. Soc. **346**, 97 (2003).
25. S. Nakano, K. Itegaki, R. J. Bouma, *et al.*, IAU Circ. **8377**, 1 (2004).
26. M. M. Phillips and R. E. Williams, in *Supernovae. The 10th Santa Cruz Workshop in Astronomy and Astrophysics, Lick Observatory, 1989*, Ed. by S. E. Woosley (Springer, New York, 1991), p. 36.
27. L. Scheck, T. Plewa, H.-Th. Janka, *et al.*, Phys. Rev. Lett. **92**, 1103 (2004).
28. D. Schlegel, D. Finkbeiner, and M. Davis, Astrophys. J. **500**, 525 (1998).
29. M. J. Seaton, Mon. Not. R. Astron. Soc. **187**, 75 (1979).
30. J. Spyromilio and P. A. Pinto, in *SN 1987A and Other Supernovae. Proceedings of an ESO/IEPS Workshop, Marciana Marina, Isola d'Elba, 1990*, Ed. by I. J. Danziger and K. Kjär (ESO, Garching, 1991), p. 423.
31. N. B. Suntzeff and P. Bouchet, in *Supernovae*, Ed. by S. E. Woosley (Springer, New York, 1991), p. 3.
32. V. P. Utrobin, Pis'ma Astron. Zh. **30**, 334 (2004) [Astron. Lett. **30**, 293 (2004)].
33. X. Wang, Y. Yang, T. Zhang, *et al.*, Astrophys. J. **626**, L89 (2005).
34. L. Wang, J. C. Wheeler, and P. Höflich, Astrophys. J. **579**, 671 (2002).
35. T. A. Weaver and S. E. Woosley, in *Ninth Texas Symp. on Relativistic Astrophysics, Munich, West Germany*, Ed. by J. Ehlers, J. Perry, and M. Walker (N. Y. Acad. Sci., N. Y., 1980), p. 335.
36. S. E. Woosley and T. A. Weaver, Astrophys. J., Suppl. Ser. **101**, 181 (1995).
37. Y. Xu and R. McCray, in *Supernovae. The 10th Santa Cruz Workshop in Astronomy and Astrophysics, Lick Observatory, 1989*, Ed. by S. E. Woosley (Springer, New York, 1991), p. 444.
38. F.-J. Zickgraf, R. M. Humphreys, M. L. Sitko, and T. Manley, Publ. Astron. Soc. Pac. **102**, 925 (1990).

Translated by V. Astakhov

Astronomy Letters, Vol. 31, No. 12, 2005, pp. 806–815. Translated from Pis'ma v Astronomicheskiĭ Zhurnal, Vol. 31, No. 12, 2005, pp. 903–912.

Supernova 1987A: The Envelope Mass and the Explosion Energy

V. P. Utrobin*

Institute for Theoretical and Experimental Physics, ul. Bol'shaya Cheremushkinskaya 25, Moscow, 117259 Russia
Max-Planck-Institut für Astrophysik, Karl-Schwarzschild-Str. 1, Postfach 1317, D-85741 Garching, Germany
Received June 14, 2005

Abstract—Our study of the photometric and spectroscopic observations of SN 1987A based on the hydrodynamic modeling of its bolometric light curve and nonstationary hydrogen kinetics and energy balance when modeling the hydrogen spectral lines at the photospheric stage has shown that good agreement with the observations can be achieved only at a ratio of the explosion energy to the ejected-envelope mass of $\approx 0.83 \times 10^{50}$ erg $M_\odot^{-1}$. In this case, the radius of the presupernova is $35.0 \pm 5 R_\odot$, and the surface chemical composition is typical of the LMC with the mass fractions of hydrogen $X = 0.743$, helium $Y = 0.251$, and heavy elements $Z = 0.006$. The analyzed dependence of the bolometric light curve on the mass of the ejected envelope at the above ratio of the explosion energy to the envelope mass suggests that the optimal mass is $18.0 M_\odot$ with an admissible spread of $\pm 1.5 M_\odot$, and, accordingly, the explosion energy of SN 1987A is $(1.50 \pm 0.12) \times 10^{51}$ erg. If a neutron star with a mass of $\approx 1.6 M_\odot$ was formed through the gravitational collapse of an iron stellar core, then the mass of the presupernova immediately before the explosion of SN 1987A was $19.6 \pm 1.5 M_\odot$. © *2005 Pleiades Publishing, Inc.*

Key words: *supernovae and supernova remnants*.

INTRODUCTION

The mass of a star is a fundamental parameter that determines the properties of the star and the course of its evolution. Therefore, estimating the mass of the matter ejected during a supernova (SN) explosion is of paramount importance; in addition, it sheds light on the final stages of stellar evolution. Determining the kinetic energy of the ejected envelope imposes a constraint on the explosion energy, a key parameter of the SN explosion mechanism. Unfortunately, even in the case of SN 1987A, a well-studied supernova that exploded in the Large Magellanic Cloud (LMC) and that provided surprisingly extensive astrophysical information, the mass of the envelope and its kinetic energy are still open to question.

The hydrodynamic modeling of the SN 1987A explosion (only this modeling can give a relatively reliable interpretation of the photometric SN observations) painted a not entirely clear picture of this phenomenon. Two approaches turned out to be possible in the hydrodynamic modeling. The first approach is based on evolutionary calculations of the presupernova and has to use strong mixing of the radioactive ^{56}Ni nuclide up to velocities of $\sim$4000 km s^{-1} to reproduce the observed bolometric light curve (Woosley 1988; Shigeyama and Nomoto 1990; Blinnikov *et al.* 2000). Woosley (1988) showed that the SN 1987A explosion had the following basic parameters: the presupernova radius $43.1 \pm 14.4 R_\odot$, the mass of the hydrogen-containing envelope $5{-}10 M_\odot$, the explosion energy $(0.8{-}1.5) \times 10^{51}$ erg, and the ratio of the explosion energy to the ejected-envelope mass $\sim 0.73 \times 10^{50}$ erg $M_\odot^{-1}$. Shigeyama and Nomoto (1990) obtained slightly different values: the presupernova radius $35.9{-}50.3 R_\odot$, the ejected-envelope mass $11.4{-}14.6 M_\odot$, the explosion energy $(1.0 \pm 0.4) \times 10^{51}$ erg, and the ratio of the explosion energy to the ejected-envelope mass $\sim 0.76 \times 10^{50}$ erg $M_\odot^{-1}$. Blinnikov *et al.* (2000) confirmed the previous results: the presupernova radius $48.5 R_\odot$, the ejected-envelope mass $14.67 M_\odot$, the explosion energy $(1.1 \pm 0.3) \times 10^{51}$ erg, and the ratio of the explosion energy to the ejected-envelope mass $\sim 0.75 \times 10^{50}$ erg $M_\odot^{-1}$. The second approach in the hydrodynamic modeling of the SN 1987A explosion uses nonevolutionary models of the presupernova constructed from the condition of the best agreement with the observations and demonstrates the possibility of moderate ^{56}Ni mixing up to velocities of $\sim$2000 km s^{-1} (Utrobin 1993). Our previous calculations (Utrobin 1993) showed that this approach yields higher values of the ejected-envelope mass and the explosion energy and the following basic parameters: the presupernova radius

*E-mail: utrobin@itep.ru

$47R_\odot$, the ejected-envelope mass $15-19M_\odot$, the explosion energy $(1.25-1.65) \times 10^{51}$ erg, and the ratio of the explosion energy to the envelope mass $\approx 0.85 \times 10^{50}$ erg $M_\odot^{-1}$. Thus, unfortunately, interpreting only the photometric observations of SN 1987A by hydrodynamically modeling its explosion admits of a very wide range of basic parameters: the presupernova radius $28.7-57.5R_\odot$, the ejected-envelope mass $9.4-19M_\odot$, the explosion energy $(0.6-1.65) \times 10^{51}$ erg, and the ratio of the explosion energy to the envelope mass $(0.73-0.85) \times 10^{50}$ erg $M_\odot^{-1}$.

Using the spectroscopic observations of SN 1987A, which undoubtedly contain more information about the structure of the presupernova and the pattern of its explosion than the photometric observations, could rectify the situation. However, an adequate analysis of the spectra at the photospheric expansion phase was restrained by the lack of a clear understanding of the nature of even the hydrogen lines. Realizing the role of nonstationary hydrogen recombination in populating the second level in the atmosphere of SN 1987A (Chugai 1991) and reliable confirmation of this effect with allowance made for the ion–molecular processes for type-II plateau supernovae, including SN 1987A (Utrobin and Chugain 2002), made it possible to study the hydrogen spectral lines. The development of a completely nonstationary approach to studying the spectral lines of hydrogen and other elements and its application to the atmosphere of SN 1987A constructed from the currently available hydrodynamic model (Utrobin 2004) allowed such an important parameter as the ratio of the explosion energy to the ejected-envelope mass to be refined (Utrobin and Chugai 2005). Such a simultaneous study of both the photometric and spectroscopic observations based on the hydrodynamic model is highly efficient and promising.

In this paper, we use the above method to investigate the SN 1987A explosion by additionally studying the influence of the presupernova radius, the mass of the ejected envelope, and its kinetic energy and attempt to find optimal values for these basic parameters of the phenomenon. For this purpose, we first present a general dependence of the bolometric luminosity of the supernova on the initial radius, the ejected-envelope mass, the explosion energy, and the surface chemical composition of the presupernova. Using this dependence and simultaneously studying the photometric and spectroscopic observations of SN 1987A, we determine plausible values of the presupernova radius and the ratio of the explosion energy to the ejected-envelope mass. Subsequently, we analyze the dependence of both the bolometric light curve of the supernova and the Hα line profile on the mass of the ejected envelope at a fixed value of this ratio and obtain an optimal value of the ejected-envelope mass and, hence, the explosion energy of SN 1987A. In conclusion, we discuss the results obtained for SN 1987A and their possible applications.

THE DEPENDENCE OF THE SUPERNOVA LUMINOSITY ON BASIC PARAMETERS

The basic parameters on which the bolometric luminosity of a supernova depends at a fixed mass of the radioactive ^{56}Ni nuclide include the initial radius R_0, the mass of the ejected envelope $M_{\rm env}$, the explosion energy E, and the surface chemical composition of the presupernova. This dependence has been studied both in the approximation of flux-limited radiative heat conduction (Utrobin 1989, 1993) and in terms of radiation hydrodynamics (Blinnikov *et al.* 2000; Utrobin 2004). A comprehensive analysis of the above dependence became possible after a detailed study of the hydrodynamic model for SN 1987A using evolutionary and nonevolutionary models of the presupernova (Utrobin 2004). As the basic hydrodynamic model, we took model M18 (see the table). It is based on a hydrostatic nonevolutionary model of the presupernova with an initial radius of $R_0 = 35.0R_\odot$; an ejected-envelope mass of $M_{\rm env} = 18.0M_\odot$; a surface chemical composition typical of the LMC with hydrogen, helium, and heavy-element mass fractions of $X = 0.743$, $Y = 0.251$, and $Z = 0.006$, respectively; and an explosion energy of $E = 1.50 \times 10^{51}$ erg. Using auxiliary hydrodynamic models, Rps, Mms, Ems, and Xms (see the table), Fig. 1 presents the dependence of the bolometric luminosity of the supernova on the initial radius, the mass of the ejected envelope, the explosion energy, and the surface chemical composition of the presupernova.

Increasing the initial radius R_0 from $35.0R_\odot$ to $46.8R_\odot$ (see the table, models M18 and Rps) causes an increase in the characteristic envelope expansion time scale and, as a result, an increase in the width of the narrow intense peak on the bolometric light curve produced by the heating of the outer layers as the shock emerged on the surface of the presupernova and by the subsequent rapid cooling of these layers as the star expanded (Fig. 1a). In addition, increasing the initial radius decreases the role of adiabatic energy losses and, accordingly, increases the bolometric luminosity of the supernova at the cooling wave (CW) stage from $\sim$10 days to $\sim$30 days. Since the physical conditions for photon diffusion in the inner layers of the envelope depend weakly on the initial radius, the bolometric luminosity near and after maximum light was almost constant.

Decreasing the mass of the ejected envelope $M_{\rm env}$ by $\approx$17% (see the table, models M18 and Mms) has

Parameters of the hydrodynamic models

Model	R_0, $R_\odot$	$M_{\rm env}$, $M_\odot$	E, 10^{51} erg	$M_{\rm Ni}$, $M_\odot$	X	Y	Z
Rps	46.8	18	1.50	0.0765	0.743	0.251	0.006
Mms	35.0	15	1.50	0.0765	0.743	0.251	0.006
Ems	35.0	18	1.00	0.0765	0.743	0.251	0.006
Xms	35.0	18	1.50	0.0765	0.555	0.441	0.004
M15	35.0	15	1.25	0.0765	0.743	0.251	0.006
M16	35.0	16	1.33	0.0765	0.743	0.251	0.006
M17	35.0	17	1.42	0.0765	0.743	0.251	0.006
M18	35.0	18	1.50	0.0765	0.743	0.251	0.006
M19	35.0	19	1.58	0.0765	0.743	0.251	0.006
M20	35.0	20	1.67	0.0765	0.743	0.251	0.006
M21	35.0	21	1.75	0.0765	0.743	0.251	0.006

virtually no effect on the narrow peak in the bolometric light curve and on the supernova luminosity at the CW stage (Fig. 1b). However, decreasing the matter density in the inner layers of the envelope reduces the characteristic photon diffusion time scale. This, in turn, increases the bolometric luminosity of the supernova on the branch ascending to maximum light by displacing the dome of the light curve as a whole toward the earlier times.

In contrast to the decrease in the ejected-envelope mass by ≈17%, decreasing the explosion energy E by a factor of 1.5 (see the table, models M18 and Ems) lowers the bolometric luminosity both in the narrow peak of the light curve and on the branch ascending to maximum light by reducing the maximum itself and displacing it toward the later times (Fig. 1c). This behavior of the luminosity can be explained in terms of a significant decrease in the mean velocity of the envelope and an appreciable weakening of the shock propagating through the presupernova matter and, as a result, heating the latter to a lesser degree, which decreases the luminosity in the narrow peak of the light curve and at the CW stage. Since the characteristic photon diffusion time scale in the central regions of the envelope is longer, the ascending branch of the light curve runs lower and reaches its maximum at a lower luminosity and considerably later, conserving the energy emitted by the supernova to within ∼5%.

Replacing the chemical composition of the LMC with $X = 0.743$, $Y = 0.251$, and $Z = 0.006$ in the surface layers of the presupernova by a chemical composition with $X = 0.555$, $Y = 0.441$, and $Z = 0.004$ at an appreciably lower hydrogen abundance (see the table, models M18 and Xms) corresponds to a significant decrease in the opacity of these layers. This decrease in opacity leads to the corresponding increase in bolometric luminosity in the interval $t_{\rm obs} \approx$ 5–70 days (Fig. 1d). The dome of the bolometric light curve undergoes almost no changes, since the physical conditions are retained in the central regions of the envelope.

THE PRESUPERNOVA RADIUS AND THE RATIO OF THE KINETIC ENERGY OF THE ENVELOPE TO ITS MASS

We used a nonevolutionary model of the presupernova obtained from the condition of the best agreement between the computed and observed bolometric light curves at moderate ^{56}Ni mixing (Fig. 2a) to study in detail the hydrodynamic model of SN 1987A (Utrobin 2004). The presupernova model was constructed from an evolutionary model by Woosley *et al.* (1997) and had an ejected-envelope mass of $M_{\rm env} = 18.0M_\odot$, a total mass of $M = 19.58M_\odot$, and an initial radius of $R_0 = 46.8R_\odot$; the latter corresponds to a distance modulus of $m - M = 18.5$ for the LMC, a color excess of $E(B{-}V) = 0.15$, and an interstellar extinction of $A_V = 3.1E(B{-}V)$ (Pun *et al.* 1995). The surface chemical composition of the presupernova with hydrogen, helium, and heavy-element mass fractions of $X = 0.555$, $Y = 0.441$, and $Z = 0.004$, respectively, corresponds to the ratio $n({\rm He})/n({\rm H}) = 0.20$ in the circumstellar matter of SN 1987A (Wang 1991; Lundqvist and Fransson 1996) and to the metal abundance in the LMC derived by Dufour (1984). The explosion energy, which was specified as an excess above the total energy of the initial envelope configuration and, in fact, determined the kinetic energy of the ejected

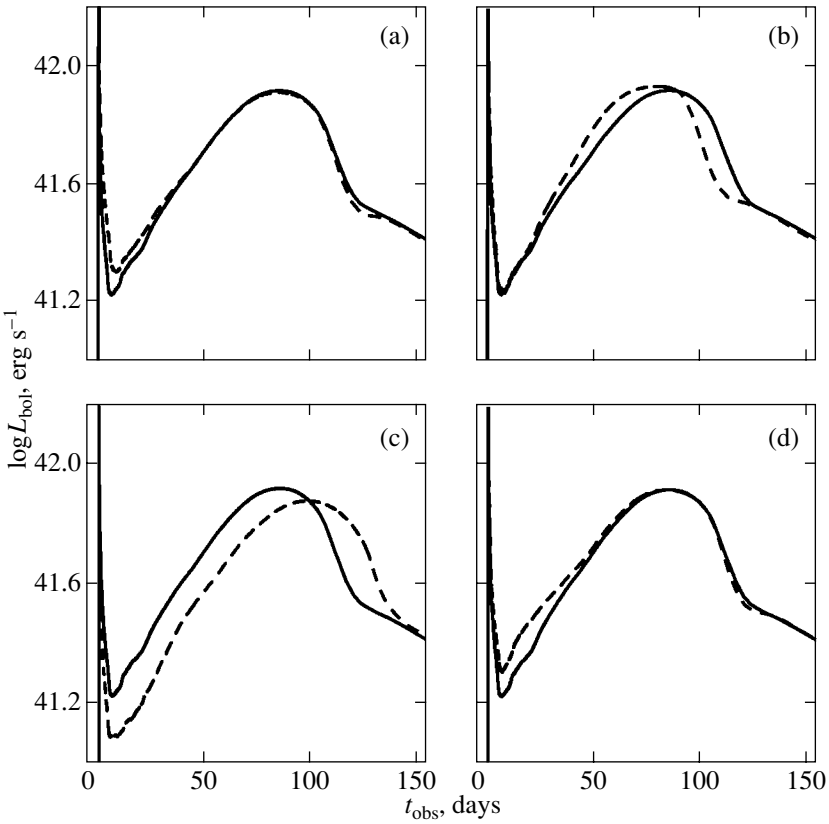

Fig. 1. Bolometric luminosity of the supernova vs. basic parameters: (a) the initial radius R_0 (model Rps), (b) the ejected-envelope mass M_{env} (model Mms), (c) the explosion energy E (model Ems), and (d) the surface chemical composition of the presupernova (model Xms). The solid and dashed lines represent the basic hydrodynamic model M18 and the corresponding auxiliary model, respectively.

envelope, was $E = 1.0 \times 10^{51}$ erg, and the mass of the radioactive nickel nuclide M_{Ni} was $0.073 M_\odot$.

However, as was shown more recently by Utrobin and Chugai (2005), good agreement between the computed and observed bolometric light curves (Fig. 2a) found no proper confirmation when the theoretical Hα line profile was compared with the observed one 4.64 days after the explosion (Fig. 2b). This phase of the supernova is of great importance for studying the hydrodynamic flow of the expanding envelope using the observed Hα line profile, since its absorption component is formed in envelope layers that span a wide range of expansion velocities, 9700–25 000 km s^{-1}. Utrobin and Chugai (2005) have found that the intensity of both the emission and absorption components of the Hα line depends on the matter density in the outer layers of the envelope: the higher the density in the range of velocities responsible for the absorption component, the stronger the Hα line. The increase in the matter density in the outer layers of the envelope required for the agreement with the observed Hα line profile was shown to be achieved by increasing the explosion energy to $E = 1.5 \times 10^{51}$ erg at a fixed ejected-envelope mass (Fig. 2d). Thus, the reproduction of the Hα line profile at 4.64 days that closely matches the spectroscopic observations of SN 1987A is possible only at a ratio of the explosion energy to the ejected-envelope mass of $E/M_{env} \approx 0.83 \times 10^{50}$ erg $M_\odot^{-1}$.

A simple increase in the explosion energy is known to cause the corresponding increase in the bolometric luminosity on the ascending branch of the light curve (Fig. 1c). This increase in luminosity at a fixed ejected-envelope mass can be offset by a decrease in the presupernova radius (Fig. 1a) and an increase in the hydrogen mass fraction in the surface layers of the envelope (Fig. 1d). Decreasing the presupernova radius to $R_0 = 35.0 R_\odot$ and passing to a surface chemical composition with $X = 0.743$, $Y = 0.251$, and $Z = 0.006$, which, according to Dufour (1984), is typical of the LMC, increases the explosion energy by only a factor of 1.5 at good agreement with the observed bolometric light curve (Fig. 2c). In addition, we used the currently available color excess $E(B - V) = 0.17$ (Michael *et al.* 2003) and, accordingly, a larger mass of radioactive nickel, $M_{Ni} = 0.0765 M_\odot$.

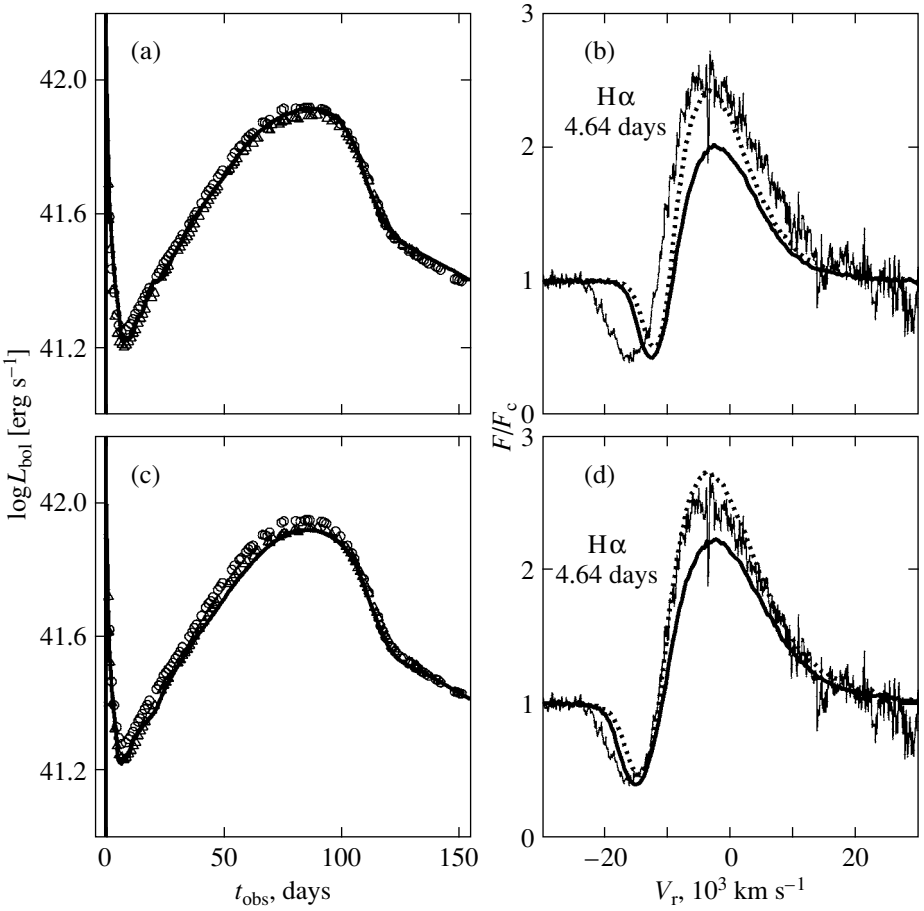

Fig. 2. Comparison of the hydrodynamic models for SN 1987A with low and high explosion energies. The bolometric light curves: (a) model N with an explosion energy of 10^{51} erg from Utrobin (2004) and (c) model M18 with an explosion energy of 1.5×10^{51} erg. The circles and triangles represent the observations of SN 1987A by Catchpole *et al.* (1987, 1988) and Hamuy *et al.* (1988), respectively. The Hα line profiles 4.64 days after the explosion: (b) model N and (d) model M18. The Hα line was computed for two extreme cases of photospheric continuum radiation (Utrobin and Chugai 2005): blackbody radiation with the effective temperature from the hydrodynamic model (dotted line) and radiation with the observed spectrum (thick solid line). The thin solid line represents the spectroscopic observations by Phillips *et al.* (1988).

The hydrodynamic model M18 (see the table) meets all of the above requirements. The decrease in the presupernova radius from $46.8R_\odot$ to $35.0R_\odot$, along with the decrease in the bolometric luminosity at the CW stage, also strengthened the agreement with the observations on the descending branch of the narrow and intense peak on the bolometric light curve in the interval $t_{obs} \approx 1$–5 days (Figs. 2a, 2c). If half the difference between the observations by Catchpole *et al.* (1987, 1988) and Hamuy *et al.* (1988) in the interval 10–70 days is taken as a measure of uncertainty in the measured bolometric luminosity of SN 1987A, then a change in the presupernova radius within $\pm 5R_\odot$ (Fig. 1a) near the basic value of $35R_\odot$ will roughly correspond to this measure.

THE BOLOMETRIC LIGHT CURVE AND THE ENVELOPE MASS

A simultaneous analysis of the photometric and spectroscopic observations of SN 1987A showed that reasonable agreement with them can be achieved only at a ratio of the explosion energy to the ejected-envelope mass of $E/M_{env} \approx 0.83 \times 10^{50}$ erg $M_\odot^{-1}$. Knowing the required value of this important ratio and fixing it, we attempted to analyze the dependence of the bolometric light curve on the mass of the ejected envelope. Varying the ejected-envelope mass M_{env} over the range 15–$21M_\odot$ showed that the hydrodynamic model M18 (Fig. 3) with $M_{env} = 18M_\odot$ is optimal.

The lower-mass hydrodynamic models M15, M16, and M17 (see the table) exhibit noticeable deviations from the optimal model M18 both at the CW stage

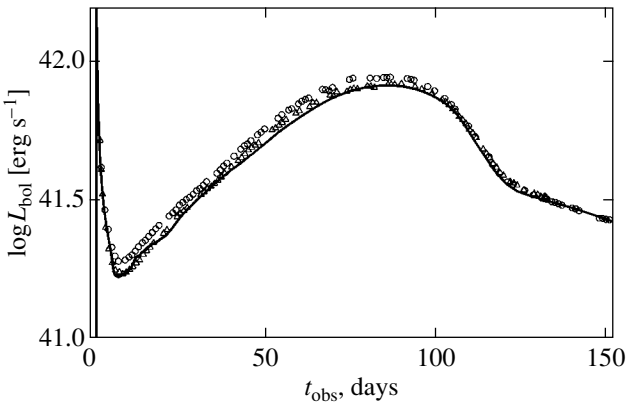

Fig. 3. Bolometric light curve for the optimal hydrodynamic model M18 (solid line). The circles and triangles represent the observations of SN 1987A by Catchpole *et al.* (1987, 1988) and Hamuy *et al.* (1988), respectively.

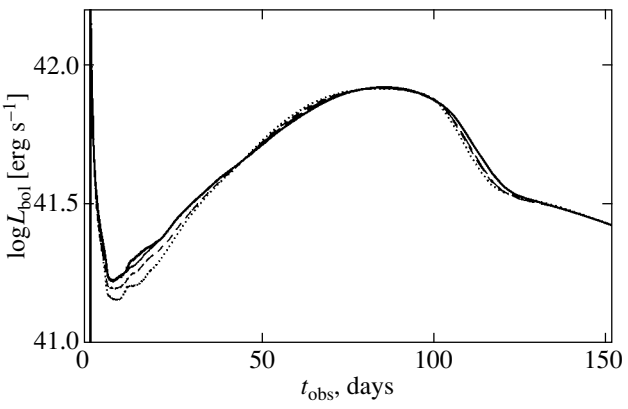

Fig. 4. Bolometric light curves for models M18 (solid line), M17 (long dashes), M16 (short dashes), and M15 (dotted line).

and after maximum light (Fig. 4). The decrease in luminosity at the CW stage with decreasing mass of the ejected envelope when the condition $E \propto M_{\rm env}$ is satisfied immediately follows from our analysis of the dependence of the bolometric luminosity of the supernova on the ejected-envelope mass and the explosion energy, which is shown in Figs. 1b and 1c, and is related to a strong dependence on the explosion energy. After maximum light, the deviation of the bolometric luminosity from that of the optimal model M18 increases with decreasing mass of the ejected envelope, since a lower matter density in the inner layers and, hence, a lower deposition of the energy released during the radioactive ^{56}Co decays corresponds to a lower mass at a fixed mean envelope velocity. It is for these physical reasons that the bolometric luminosity of the higher-mass hydrodynamic models (M19, M20, and M21 in the table) exceeds appreciably the luminosity of model M18 at the CW stage and, to a lesser degree, near and after maximum light (Fig. 5).

The detected sensitivity of the bolometric luminosity to the ejected-envelope mass allows the range of admissible masses to be estimated. As we see from Fig. 4, decreasing the ejected-envelope mass of the optimal model M18 by $1M_\odot$ (model M17) has almost no effect on the luminosity at the CW stage and only reduces it after maximum light, while decreasing the mass by $2M_\odot$ (model M16) changes significantly the light curve. Consequently, it is quite acceptable to decrease the envelope mass by $\sim 1.5M_\odot$ if the measure of uncertainty in the measured bolometric luminosity of SN 1987A introduced above is used. For higher masses, even increasing the ejected-envelope mass of the optimal model M18 by $1M_\odot$ (model M19) causes a change in the luminosity comparable to the chosen measure of uncertainty (Fig. 5). Thus, based on the discussed dependence of the bolometric light curve, we can assert that the optimal mass of the ejected envelope is $M_{\rm env} = 18.0M_\odot$ with an admissible spread of $\pm 1.5M_\odot$.

THE Hα LINE AND THE ENVELOPE MASS

Now, it is time to study the dependence of the Hα line profile at 4.64 days on the ejected-envelope mass at a fixed ratio $E/M_{\rm env}$, which is shown in Fig. 6. First of all, note the spectral feature of the Hα line in SN 1987A that was observed within the first two weeks after the supernova explosion and that consisted in a blueshift of the Hα emission component (negative radial velocities) (Menzies *et al.* 1987). This blueshift of the emission component arises in an atmosphere with a significant Thomson scattering by free electrons when photons are diffusively reflected from the photosphere, since the photons emitted by the photosphere after their backscattering followed by their reflection from the expanding subphotospheric layers acquire a predominantly higher energy (Chugai 1988). In addition, it increases appreciably when the relativistic effects are included (Mihalas 1978; Jeffery 1993). At an optical depth for Thomson scattering by free electrons in the atmosphere of ≈ 1.6 at 4.64 days, the computed Hα line profiles exhibit this effect (Figs. 6a, 6b) and agree well with the observations (Fig. 2d).

Comparison of the Hα line profiles at 4.64 days for the optimal model M18 and model M15, the envelope masses of which differ by $3M_\odot$, shows that decreasing the ejected-envelope mass also causes an appreciable growth of the Hα emission component near maximum light and in the red wing, with the absorption component being unchanged (Fig. 6a). This emission excess results from the subphotospheric increase in

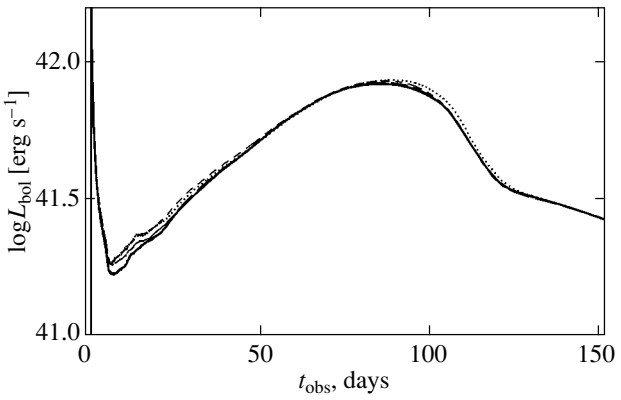

Fig. 5. Bolometric light curves for models M18 (solid line), M19 (long dashes), M20 (short dashes), and M21 (dotted line).

the hydrogen excitation, which manifests itself in a larger optical depth of the Hα line (Fig. 6c) and, accordingly, in greater emission of the photons that are scattered by free electrons and that drift from the blue spectral region to the red one. Increasing the ejected-envelope mass from $18M_\odot$ in the optimal model M18 to $21M_\odot$ in model M21 causes an insignificant reduction of the Hα emission component at 4.64 days and a barely noticeable shift of the Hα absorption component to the higher radial velocities (Fig. 6b). This change in the Hα line profile is attributable to the smaller line optical depth in model M21 than that in model M18 (Fig. 6d).

Significant deviations of the ejected-envelope mass, by $3M_\odot$, from the optimal value of $18M_\odot$ cause no significant changes in the Hα line profile at 4.64 days. This is mainly the result of nonstationary hydrogen recombination, which essentially offsets the influence of the ejected-envelope mass. As a result, it can be argued that the established weak dependence of the Hα line profile at 4.64 days on the envelope mass at a fixed ratio $E/M_{\rm env}$ imposes less stringent constraints on the mass than the dependence of the bolometric light curve analyzed above and does not allow the admissible spread in mass to be narrowed, especially when the high noise level in the spectra observed at this phase is taken into account.

DISCUSSION

A simultaneous analysis of the photometric and spectroscopic observations of SN 1987A based on the hydrodynamic modeling of its bolometric light curve and nonstationary hydrogen kinetics and energy balance when modeling the hydrogen spectral lines at the photospheric stage showed that good agreement with the observations could be achieved only at a ratio of the explosion energy to the ejected-envelope mass of $\approx 0.83 \times 10^{50}$ erg $M_\odot^{-1}$. In this case, the presupernova radius is $35 \pm 5R_\odot$, and the chemical composition of the surface layers is typical of the LMC with hydrogen, helium, and heavy-element mass fractions of $X = 0.743$, $Y = 0.251$, and $Z = 0.006$, respectively. The analyzed dependence of the bolometric light curve and the Hα line profile at 4.64 days on the ejected-envelope mass at the ratio of the explosion energy to the envelope mass determined above suggests that the optimal mass is $18.0M_\odot$ with an admissible spread of $\pm 1.5M_\odot$. It thus immediately follows that the explosion energy of SN 1987A is $(1.50 \pm 0.12) \times 10^{51}$ erg. Thus, having complemented the traditional analysis of the photometric observations of SN 1987A via hydrodynamic modeling by a spectral analysis, we achieved our goal and obtained a significant and reliable refinement of the basic supernova explosion parameters.

According to the evolutionary calculations by Woosley *et al.* (1997, 2002), the iron core of a main-sequence star with a mass of $\sim 20M_\odot$ collapses to produce a stellar remnant in the form of a neutron star with a mass of $\approx 1.6M_\odot$. Consequently, it can be asserted that the presupernova mass was $19.6 \pm 1.5M_\odot$ immediately before the explosion of SN 1987A. A careful analysis of the ten-year-long observations of the optical echo from the neighborhood around SN 1987A allowed the complex three-dimensional structure to be reconstructed in which a bipolar nebular can be distinguished and which consists of gas and dust with a total mass of $\sim 1.7M_\odot$ (Sugerman *et al.* 2005). It would be natural to assume that this extended structure rich in features is the result of the entire evolution of the presupernova with mass loss up to the SN 1987A explosion. Given this observed structure, a rotating main-sequence star with a mass of at least $21.3 \pm 1.5M_\odot$ corresponds to the SN 1987A phenomenon in the case of a single star. For SN 1987A, the luminosity of the presupernova is determined by the helium core mass, and its observed value agrees with a core mass of $\sim 6M_\odot$, which, in turn, corresponds to a nonrotating main-sequence star with a mass of $16-22M_\odot$ (Woosley 1988) or $18-22M_\odot$ (Nomoto and Hashimoto 1988; Shigeyama and Nomoto 1990; Woosley *et al.* 1997). In the scenario of a binary system where the presupernova evolved as a member of a close binary until it merged with the secondary component, the above estimate of $21.3 \pm 1.5M_\odot$ yields the minimum total mass of the two components.

The explosion energy of SN 1987A or, in fact, the kinetic energy of the ejected envelope, $(1.50 \pm 0.12) \times 10^{51}$ erg, that we estimated places a slightly more stringent energy requirement for the specific supernova explosion mechanism rather than relaxes it.

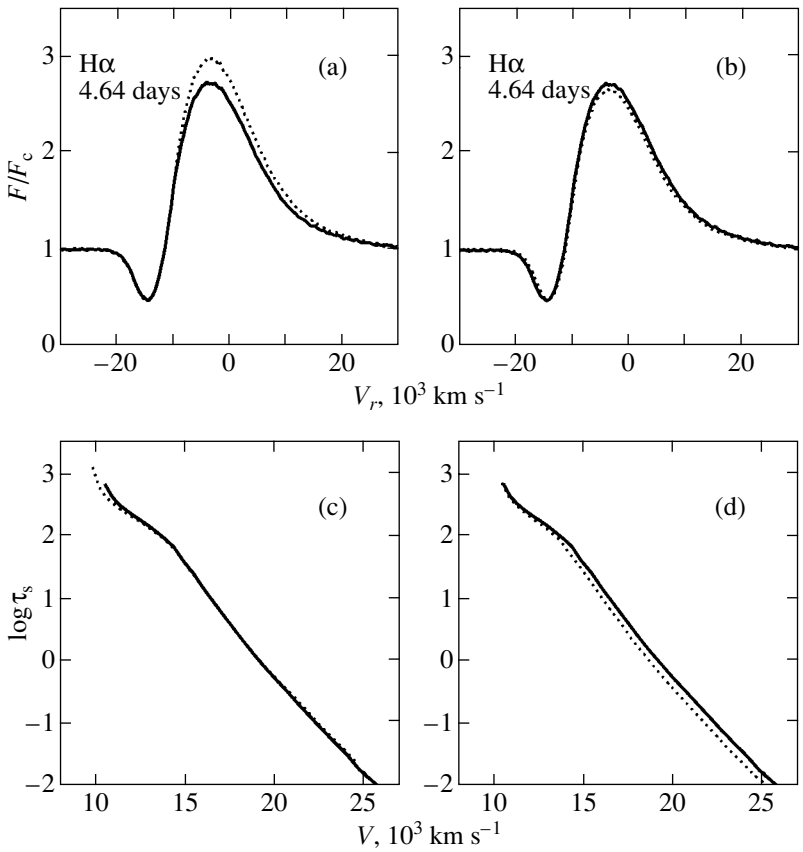

Fig. 6. Dependence of the Hα line profile 4.64 days after the explosion and the Hα optical depth as a function of the velocity on the ejected-envelope mass at a fixed ratio $E/M_{\rm env}$: (a) and (c) model M18 (solid line) and model M15 (dotted line); (b) and (d) model M18 (solid line) and model M21 (dotted line). The Hα line was computed for the photospheric continuum in the form of blackbody radiation with the effective temperature from the corresponding hydrodynamic model.

Unfortunately, this result cannot yet be used properly, since the currently available theory for the explosion of collapsing supernovae with massive ($\sim 1.6 M_\odot$) iron cores, which includes the neutrino-convective mechanism, the magnetorotational mechanism, and the scenario of the rotational mechanism, is being continuously developed, and this process is far from being complete and, accordingly, from obtaining reliable supernova explosion energies.

The study of the gravitational collapse of an iron stellar core that has continued for almost forty years has been mostly in crisis and has not yet given a clear answer regarding the ways out of it. The only unquestionable result of the numerous studies is the absence of ejection of the outer envelope with a kinetic energy comparable in scales to the supernova explosion energy for spherically symmetric collapse, despite an increasingly accurate description of all physical processes (see, e.g., Colgate and White 1966; Nadyozhin 1978; Bruenn 1985, 1989a, 1989b; Myra *et al.* 1987; Swesty *et al.* 1994; Rampp and Janka 2000; Bruenn *et al.* 2001; Mezzacappa *et al.* 2001). This important result forced us to abandon spherical symmetry and to pass to multidimensional problems of the neutrino-convective supernova explosion mechanism with the (simultaneous, if possible) inclusion of very complex processes: the interaction between neutrinos of different flavors with matter, neutrino transport, hydrodynamic instabilities (including convection), rotation, and the generation and strengthening of magnetic fields. The current attempts to model some of these processes (two-dimensional collapse, convection, solution of the Boltzmann equation for neutrinos, and rotation (Buras *et al.* 2003); three-dimensional collapse, convection, and flux-limited neutrino transport (Fryer and Warren 2002); and the same with rotation (Fryer and Warren 2004)) have failed so far and even have not clearly identified the most important of them. At the same time, as Janka (2001) who comprehensively analyzed the deposition of the neutrinos emitted by a hot protoneutron star, showed, the neutrino-convective mechanism has great potentialities and promises an explosion energy in the range from $\sim 10^{50}$ erg to several units times 10^{51} erg.

The magnetorotational supernova explosion mech-

anism suggested by Bisnovatyi-Kogan (1970) is based on the generation and strengthening of a toroidal magnetic field due to the differential rotation of the collapsing stellar core. When the pressure produced by the magnetic field is comparable to the gas pressure, it is capable of expelling the stellar matter outward. Since this process takes place in a medium with an outward-decreasing density, a shock wave is eventually produced. As a result, the rotation energy of the protoneutron star is transformed into the kinetic energy of the ejected envelope through the magnetic field. If the energy of the shock wave is much higher than the binding energy of the stellar envelope, then a supernova explosion arises. The currently available two-dimensional calculations of this mechanism yield an explosion energy of $\sim 0.6 \times 10^{51}$ erg (Ardeljan *et al.* 2005).

At present, the scenario of the rotational supernova explosion mechanism suggested by Imshennik (1992) appears most promising. This scenario includes the gravitational collapse of a rotating massive iron core into a rapidly rotating neutron star, its subsequent dynamical fragmentation into two neutron stars, the evolution of the formed binary system through the emission of gravitational waves until the stage of mass transfer from the low-mass component to the high-mass component, and, finally, the hydrodynamic explosion of the neutron star when it reaches the minimum ($\sim 0.1 M_\odot$) neutron star mass. According to the most recent studies (Imshennik and Manukovskii 2004), the explosion energy in this mechanism lies within the range $\sim (0.25-1.0) \times 10^{51}$ erg. A more accurate description of the physical processes may allow the maximum explosion energy to be increased by a factor of ~ 1.5 (Imshennik 2005). In addition, the response to the neutrino signal from SN 1987A detected by the LSD underground observatory under Mont Blanc has been interpreted for the first time in terms of the scenario of the rotational mechanism (Imshennik and Ryazhskaya 2004).

In conclusion, we express the hope that the parameters of the presupernova estimated when studying SN 1987A will help determine its evolutionary status and that the explosion energy found will serve as a reliable reference for the explosion mechanisms of collapsing supernovae being developed.

ACKNOWLEDGMENTS

I wish to thank V.S. Imshennik and N.N. Chugai for helpful discussions. This work was supported in part by the Russian Foundation for Basic Research, project no. 04-01-17255.

REFERENCES

1. N. V. Ardeljan, G. S. Bisnovatyi-Kogan, and S. G. Moiseenko, Mon. Not. R. Astron. Soc. **359**, 333 (2005).
2. G. S. Bisnovatyi-Kogan, Astron. Zh. **47**, 813 (1970).
3. S. Blinnikov, P. Lundqvist, O. Bartunov, *et al.*, Astrophys. J. **532**, 1132 (2000).
4. S. W. Bruenn, Astrophys. J., Suppl. Ser. **58**, 771 (1985).
5. S. W. Bruenn, Astrophys. J. **340**, 955 (1989a).
6. S. W. Bruenn, Astrophys. J. **341**, 385 (1989b).
7. S. W. Bruenn, K. R. De Nisco, and A. Mezzacappa, Astrophys. J. **560**, 326 (2001).
8. R. Buras, M. Rampp, H.-Th. Janka, and K. Kifonidis, Phys. Rev. Lett. **90**, 241 101 (2003).
9. R. M. Catchpole, J. M. Menzies, A. S. Monk, *et al.*, Mon. Not. R. Astron. Soc. **229**, 15 (1987).
10. R. M. Catchpole, P. A. Whitelock, M. W. Feast, *et al.*, Mon. Not. R. Astron. Soc. **231**, 75 (1988).
11. S. A. Colgate and R. H. White, Astrophys. J. **143**, 626 (1966).
12. N. N. Chugai, Pis'ma Astron. Zh. **14**, 787 (1988) [Sov. Astron. Lett. **14**, 334 (1988)].
13. N. N. Chugai, *Supernovae,* Ed. by S. E. Woosley (Springer-Verlag, New York, 1991), p. 286.
14. R. J. Dufour, *IAU Symposium No. 108: Structure and Evolution of the Magellanic Clouds,* Ed. by S. van den Bergh and K. S. de Boer (Reidel, Dordrecht, 1984), p. 353.
15. C. L. Fryer and M. S. Warren, Astrophys. J. **574**, L65 (2002).
16. C. L. Fryer and M. S. Warren, Astrophys. J. **601**, 391 (2004).
17. M. Hamuy, N. B. Suntzeff, R. Gonzalez, and G. Martin, Astron. J. **95**, 63 (1988).
18. V. S. Imshennik, Pis'ma Astron. Zh. **18**, 489 (1992) [Sov. Astron. Lett. **18**, 194 (1992)].
19. V. S. Imshennik, private communication (2005).
20. V. S. Imshennik and K. V. Manukovskiĭ, Pis'ma Astron. Zh. **30**, 883 (2004) [Astron. Lett. **30**, 803 (2004)].
21. V. S. Imshennik and O. G. Ryazhskaya, Pis'ma Astron. Zh. **30**, 17 (2004) [Astron. Lett. **30**, 14 (2004)].
22. H.-Th. Janka, Astron. Astrophys. **368**, 527 (2001).
23. D. J. Jeffery, Astrophys. J. **415**, 734 (1993).
24. P. Lundqvist and C. Fransson, Astrophys. J. **464**, 924 (1996).
25. J. W. Menzies, R. M. Catchpole, G. van Vuuren, *et al.*, Mon. Not. R. Astron. Soc. **227**, 39 (1987).
26. A. Mezzacappa, M. Liebendörfer, O. E. B. Messer, *et al.*, Phys. Rev. Lett. **86**, 1935 (2001).
27. E. Michael, R. McCray, R. Chevalier, *et al.*, Astrophys. J. **593**, 809 (2003).
28. D. Mihalas, *Stellar Atmospheres* (Freeman, San Francisco, 1978; Mir, Moscow, 1982), Part 2.
29. E. S. Myra, S. A. Bludman, Y. Hoffman, *et al.*, Astrophys. J. **318**, 744 (1987).
30. D. K. Nadyozhin, Astrophys. Space Sci. **53**, 131 (1978).

31. K. Nomoto and M. Hashimoto, Phys. Rep. **163**, 13 (1988).
32. M. M. Phillips, S. R. Heathcote, M. Hamuy, and M. Navarrete, Astron. J. **95**, 1087 (1988).
33. C. S. J. Pun, R. P. Kirshner, G. Sonneborn, *et al.*, Astrophys. J., Suppl. Ser. **99**, 223 (1995).
34. M. Rampp and H.-Th. Janka, Astrophys. J. **539**, L33 (2000).
35. T. Shigeyama and K. Nomoto, Astrophys. J. **360**, 242 (1990).
36. B. E. K. Sugerman, A. P. S. Crotts, W. E. Kunkel, *et al.*, Astrophys. J. (2005) (in press); astro-ph/0502378.
37. F. D. Swesty, J. M. Lattimer, and E. S. Myra, Astrophys. J. **425**, 195 (1994).
38. V. P. Utrobin, Pis'ma Astron. Zh. **15**, 99 (1989) [Sov. Astron. Lett. **15**, 42 (1989)].
39. V. P. Utrobin, Astron. Astrophys. **270**, 249 (1993).
40. V. P. Utrobin, Pis'ma Astron. Zh. **30**, 334 (2004) [Astron. Lett. **30**, 293 (2004)].
41. V. P. Utrobin and N. N. Chugai, Pis'ma Astron. Zh. **28**, 440 (2002) [Astron. Lett. **28**, 386 (2002)].
42. V. P. Utrobin and N. N. Chugai, Astron. Astrophys. **441**, 271 (2005); astro-ph/0501036.
43. L. Wang, Astron. Astrophys. **246**, L69 (1991).
44. S. E. Woosley, Astrophys. J. **330**, 218 (1988).
45. S. E. Woosley, A. Heger, and T. A. Weaver, Rev. Mod. Phys. **74**, 1015 (2002).
46. S. E. Woosley, A. Heger, T. A. Weaver, and N. Langer, presented at *SN 1987A: Ten Years Later, 1997*, Ed. by M. M. Phillips and N. B. Suntzeff (in press).

Translated by V. Astakhov

Astronomy Letters, Vol. 31, No. 12, 2005, pp. 816–823. Translated from Pis'ma v Astronomicheskiĭ Zhurnal, Vol. 31, No. 12, 2005, pp. 913–921.

An Accretion Disk, a Bipolar Outflow, and an Envelope—a Structure That Accompanies the Formation of a Protostar

L. I. Matveyenko[1*], V. A. Demichev[1], S. S. Sivakon'[1], Ph. D. Diamond[2], and D. A. Graham[3]

[1] *Space Research Institute, Russian Academy of Sciences, Profsoyuznaya ul. 84/32, Moscow, 117997 Russia*

[2] *Nuffield Radio Astronomy Observatory, Macclesfield, Great Britain*

[3] *Max-Planck-Institut für Radioastronomie, Auf dem Hügel 69, D-53121 Bonn, Germany*

Received July 11, 2005

Abstract—We analyze the superfine structure of the supermaser H_2O emission region in Orion KL over the period 1979–1999. The angular resolution reached 0.1 mas, which corresponds to 0.045 AU at a distance to Orion KL of 450 pc. We determined the velocity of the local standard of rest, $V_{LSR} = 7.65$ km s^{-1}. The formation of a protostar is accompanied by a structure that consists of an accretion disk, a bipolar outflow, and a surrounding envelope. The disk is at the stage of separation into protoplanetary rings. The disk plane is warped like the brim of a hat. The disk is 27 AU in diameter and ~0.3 AU in thickness. The rings contain ice granules. Radiation and stellar wind sublimate and blow away the water molecules to form halos around the rings, maser rings. The radiation from the rings is concentrated in the azimuthal plane, and its directivity reaches 10^{-3}. The relative velocities of the rings located in the central part of the disk 15 AU in diameter correspond to rigid-body rotation, $V_{rot} = \Omega R$. The rotation period is $T \approx 170$ yr. The injector is surrounded by a toroidal structure 1.2 AU in diameter. The diameter of the injected flow does not exceed 0.05 AU. A highly collimated bipolar outflow with a diameter of ~0.1 AU is observed at a distance as large as 3 AU. Precession of the injector axis with a period of ~10 yr forms a spiral flow structure. The flow velocity is ~10 km s^{-1}. The kinetic energy of the accreting matter and the disk is assumed to be transferred to the bipolar outflow, causing the rotation velocity distribution of the rings to deviate from the Keplerian velocity. The surrounding envelope amplifies the emission from the structure at a velocity of 7.65 km s^{-1} in a band of ~0.5 km s^{-1} by more than two orders of magnitude, which determines the supermaser emission.

Key words: *masers, star formation, rigid-body rotation, accretion disk, protoplanetary rings, bipolar outflow, envelope.*

INTRODUCTION

Gravitational instability in gas-dust complexes gives rise to active regions of protostar formation. The formation of protostars is accompanied by strong maser emission in water-vapor lines with a flux density that reaches several tens of kJy. In extremely rare cases, intense H_2O maser flares are observed; their nature and triggering mechanism are not yet completely clear (Burke *et al.* 1972; Matveyenko *et al.* 1980). In the Orion Nebula, compact maser sources are concentrated in eight zones whose sizes reach ~2000 AU (Genzel *et al.* 1978). The velocities of the maser sources are within several tens of km s^{-1}.

High activity in Orion KL was observed in the periods 1979–1987 and 1998–1999. The radio flux densities of H_2O maser flares reached 8 MJy, and the widths of the line profiles were $\Delta V \approx 0.5$ km s^{-1}. Their velocities changed only slightly and were $V \approx 8$ km s^{-1}. The coordinates of the active region are RA $= 5^h35^m14^s.121$ and DEC $= -05°22'36''.27$ (2000.0). Below, we analyze in detail the structure of the active supermaser emission region over the period under consideration.

THE H_2O SUPERMASER FLARE REGION IN THE PERIOD 1979–1987

The period of high activity 1979–1987 was accompanied by intense H_2O maser outbursts. The flux densities of the maser outbursts reached $F = 1$–8 MJy, and the duration of some of them did not exceed a few days; on average, the enhanced activity lasted for several months (Abraham *et al.* 1981; Garay *et al.* 1989). The supermaser line profiles were in the shape of a Gaussian with a high-velocity or low-velocity tail. The observed changes in the profiles

*E-mail: lmatveen@iki.rssi.ru

are attributable to a change in the relative contribution of the constituent features and are indicative of a complex spatial structure of the emission region. The line profile centroid velocity is $V \approx 8$ km s^{-1} and changes only slightly with time due to a change in the relative contribution from the maser sources. The full width at half maximum (FWHM) of the line profile is $\Delta V \approx 0.5$ km s^{-1} (Fig. 1). We analyzed the superfine structure of the H_2O supermaser emission region in Orion KL with an angular resolution of ~0.1 mas. At a distance to Orion KL of 450 pc, this corresponds to ≈0.045 AU.

VLBI measurements of the active region in Orion KL showed that the maser emission in the period under consideration is determined by a highly organized structure, a chain of compact features (Matveyenko 1981). The most complete VLBI measurements were performed in October 1985. A detailed analysis revealed both an extended structure of low brightness, $T_b \approx 10^{11}$ K, and a superfine component of high brightness, $T_b \approx 10^{16}$ K. The structure of the active region consists of a chain of bright compact features distributed along a thin, ~0.3 AU, extended S-shaped structure ~27 AU in length (Fig. 2). The velocities of the individual components of the structure are also indicated here (Demichev and Matveyenko 2004). The compact features do not exceed 0.1 AU in size. The two features located in the central part of the chain have the highest brightness temperatures, reaching $T_b \approx 10^{16}$ K. The radial velocities and brightness temperatures of these features are $V_{||} = 7.50$ km s^{-1}, $T_b \approx 10^{16}$ K and $V_{||} = 7.75$ km s^{-1}, $T_b \approx 0.6 \times 10^{16}$ K. They contain compact sources ~0.05 AU in size, and their brightness temperatures reach $T_b \approx 4 \times 10^{16}$ K.

On average, the velocities of the features in the eastern and western parts of the chain are $V_{||} \approx 9.0$ km s^{-1} and $V_{||} \approx 6.6$ km s^{-1}, respectively. A detailed velocity distribution of the features along the chain at different epochs is shown in Fig. 3. A linear change in the velocity with $dV/dR = 0.17 \pm 0.01$ km s^{-1} AU^{-1} is observed in the central part of the structure within 15 AU.

The chain of compact features under consideration corresponds to the tangential directions of the concentric rings seen edge-on, and their velocities are equal to the rotation velocity. In this case, the rotation velocity of the rings in the central part of the structure can be represented as $V_{rot} = \Omega R$, suggesting a rigid-body rotation with a constant angular velocity. The observed angular velocity Ω corresponds to a rotation period of $T \approx 170$ yr.

The brightness of the features in the chain declines with increasing distance from the center to $T_b \approx 10^{12}$ K at its edges. The velocity dependence of the brightness of the features and its conservation during the period 1979–1987 under consideration suggests an amplification of their emission by more than two orders of magnitude in the ambient medium of the envelope at a velocity $V \approx 7.7$ km s^{-1} in a ~0.5 km s^{-1} band (Matveyenko *et al.* 1988). The weighted mean value of the velocities of the two central bright features is $V = 7.65$ km s^{-1}. The velocity of the center of the structure is almost equal to this value (Fig. 3). It thus follows that the velocity of the local standard of rest is $V_{LSR} = 7.65$ km s^{-1}. Observations of the OH maser sources located in the dense molecular cloud OMC-1 yield a similar estimate (Matveyenko *et al.* 2004).

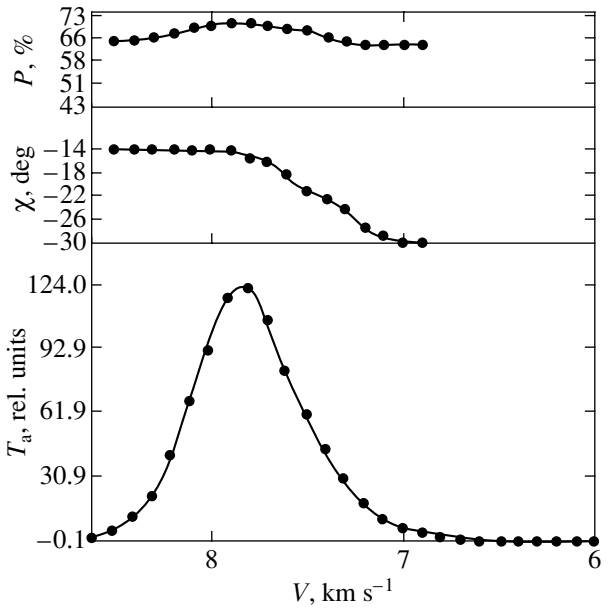

Fig. 1. Profile of the H_2O supermaser emission line in Orion KL—the velocity dependence of the antenna temperature T_a; the epoch is October 17, 1985. Variations in the polarization of the emission (P) and the position angle χ within the line profile.

The velocities of the outer parts of the chain deviate from the linear dependence in its central part (Fig. 3). This may be because the rotation of the outer part of the disk slows down and is delayed relative to the rigid-body rotation of its central part. The mean velocity gradient is $dV/dR = -0.156$ km s^{-1} AU^{-1} at the eastern edge of the disk and $dV/dR = 0.248$ km s^{-1} AU^{-1} at its western edge (the dashed line in Fig. 3). The slowdown in the western part of the disk is a factor of ~1.5 higher than that in its eastern part. There is a correlation between the slowdown and the brightness temperature of the corresponding parts of the disk. The western part of the disk is about twice as bright as its eastern

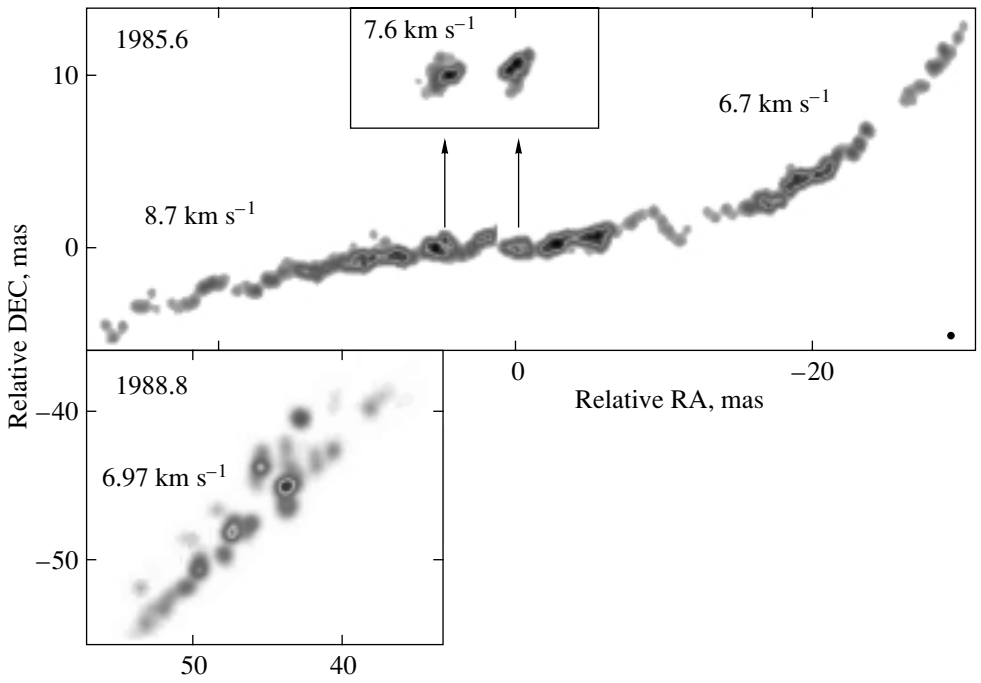

Fig. 2. Structure of the H_2O supermaser emission region in Orion KL with an angular resolution of 0.5 mas; the epoch is 1985.6. The velocities refer to the corresponding fragments of the structure. The ejection is observed at the time of decrease in activity; the epoch is 1988.8.

part (Fig. 2). The enhanced slowdown may result from the higher density of the medium, including H_2O molecules, which causes the intensity of the maser emission to increase relative to the opposite part of the disk. In particular, this can be the accreting matter that causes the plane of the outer parts of the disk to be warped. The outer part of the disk has a mean rotation velocity of $V_{\rm rot} \approx 1.1$ km s^{-1} and a radius of $R \approx 14$ AU. It lies outside the region of rigid-body rotation. Its rotation velocity may be determined by Keplerian motion, $V^2R = MG$. In this case, the total mass of the inner part of the structure is $\sim 0.02 M_\odot$.

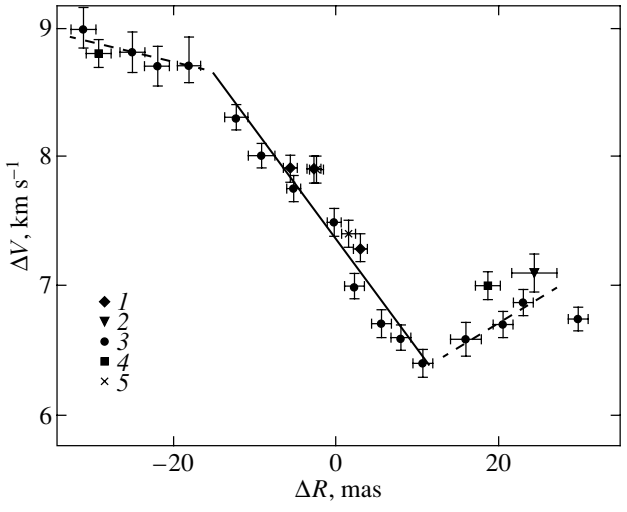

Fig. 3. Dependence of the relative velocity and positions of the features at different epochs: *1*, 1982; *2*, 1983; *3*, 1985; *4*, 1986; *5*, 1991. A linear dependence (solid line) is observed in the central part of the structure.

As we showed above, the chain of compact features corresponds to the tangential directions of the rings seen edge-on. The rings contain ice granules. Stellar wind and radiation cause the sublimation and acceleration of water molecules. They are also the excitation (pumping) sources of water-vapor molecules. Thus, halos, maser rings, are formed around the rings. A ring seen edge-on appears as two bright compact sources connected by a bridge. In the unsaturated regime, the maser emission is proportional to $T_{\rm b} \sim e^{\tau}$. The optical depth τ is proportional to the number of molecules along the line of sight, i.e., to the geometrical distance in the ring. Therefore, the radiation from the ring is concentrated in its azimuthal plane, and its directivity reaches $\leq 10^{-3}$. High directivity relaxes the pumping power requirement, but limits significantly the detectability of the ring emission.

At the end of the period of high activity 1988–1989, a jet, a fine elongated structure with bullets, was detected at a distance of $\sim$30 AU from the center of the chain in the direction PA $= 135^\circ$. The jet reached $\sim$6 AU in size, and its brightness temperature was $T_{\rm b} \approx 10^{13}$ K (Fig. 2).

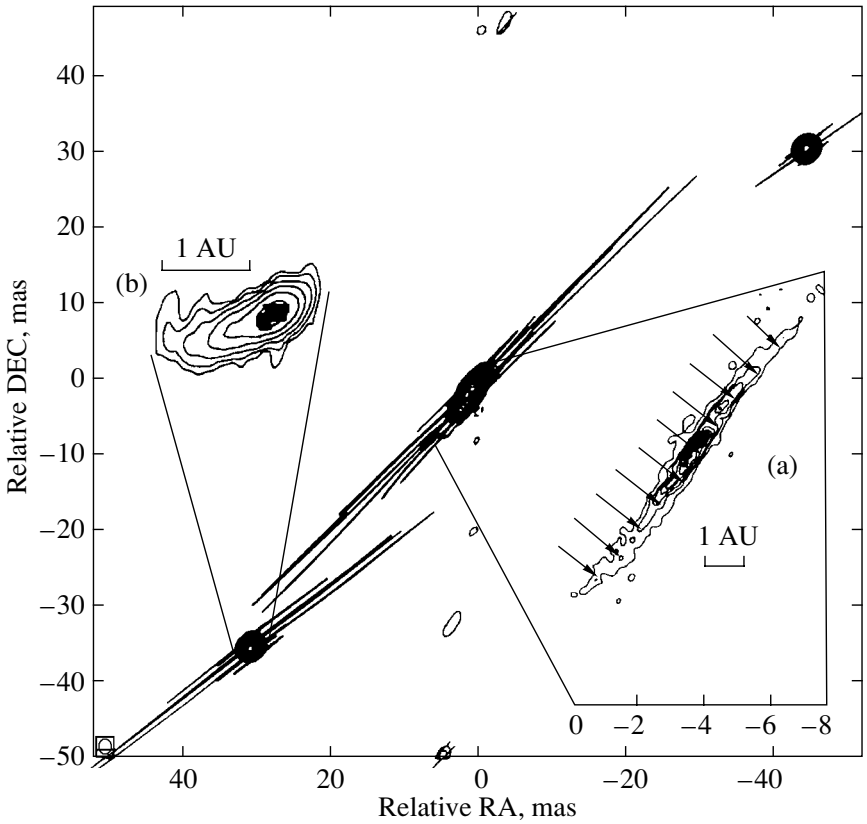

Fig. 4. Structure of the active region at the epoch of quiescence on May 26, 1995. The length and orientation of the lines correspond to the degree of polarization of the emission and the orientation of the polarization plane, respectively (the orientation angle is turned through 90°). Also shown here are the images of the bipolar outflow (a) and the bullet (b) on an enlarged scale; the angular resolution is 0.3 mas.

The supermaser emission is linearly polarized; the degree of polarization reaches 73%. Figure 1 shows the variations in polarization P and position angle χ within the line profile. The change in the orientation of the polarization plane χ within the line profile corresponds to 25 deg/km s^{-1} or ~4 deg AU^{-1} when recalculated to the observed chain (Matveyenko 1994).

THE PERIOD OF QUIESCENCE

Observations of the active region in the period of low activity (the epoch 1995.6) showed that the H_2O maser emission at a velocity of 8 km s^{-1} does not exceed 1 kJy. VLBI studies with an ultrahigh angular resolution revealed a highly collimated bipolar outflow with a bright compact central source in the putative region, but the expected chain of features was absent or its emission was below the detection limit (Fig. 4, Matveyenko *et al.* 1988). The bipolar outflow is oriented at PA = −33°, its sizes are 4.5 × 0.5 AU, and its brightness temperature is $T_b \approx 10^{12}$ K. The compact bright source in the central part of the bipolar outflow is a nozzle. The injected flow at the exit from the nozzle is oriented at PA = −44°. The flow does not exceed 0.05 × 0.15 AU in size, and its brightness temperature reaches $T_b \approx 10^{13}$ K. The radial velocity of the injector is $V_{||} = 7.63$ km s^{-1}.

As previously, bullets are observed within the active region. The southeastern bullet is at a distance of 18.5 AU from the injector in the direction PA = 132°. It has a cometary (head–tail) shape, and its radial velocity is $V_{||} = 0.32$ km s^{-1} (Fig. 4). However, the head of the "comet" is behind its tail. Since the velocity of the "comet" is low, radiation pressure and stellar wind blow the tail forward. The northwestern bullet is at a distance of 32.5 AU from the injector in the direction PA = −54°. Its relative radial velocity is $V_{||} = -0.18$ km s^{-1}. The brightness temperature of the bullets is $T_b \approx 10^{12}$ K.

The emission from the structure is linearly polarized and is indicated by the line segments in Fig. 4. The length and orientation of the lines correspond to the degree of polarization and orientation of the polarization plane (they are turned through 90° in the main figure). Also shown here on an enlarged scale

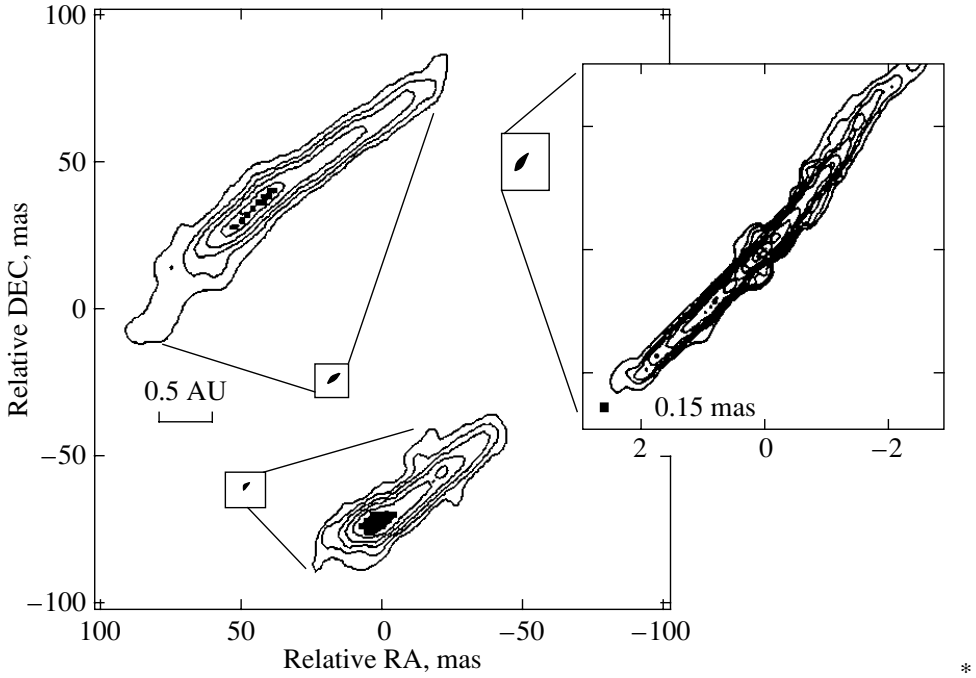

Fig. 5. Structure of the active region: the bipolar outflow and two bullets; the epoch is March 21, 1998. The fine structure of the features has an angular resolution of 0.15 mas.

are the bullet and the bipolar outflow with an angular resolution of 0.3 mas. The polarization of the emission from the bipolar outflow near the injector is 33% and increases with distance from it to 50%. This may be attributable to partial saturation of the amplification in the region of the injector, whose brightness temperature is an order of magnitude higher than that of the bipolar outflow. The polarization of the emission from the southeastern bullet reaches 45 and 13% of the northwestern bullet (Matveyenko *et al.* 1998).

HIGH ACTIVITY PERIOD 1998–1999

In the period under consideration, the line had a Gaussian profile, its velocity $V = 7.65$ km s^{-1} was conserved, and its width was ~0.5 km s^{-1}. The conservation of the line velocity and width suggests that the emission from the structure in the envelope was amplified by more than three orders of magnitude. The maser emission in February 1998 began to exponentially rise and reached its maximum level of $F = 4.3$ MJy in August–October. The emission began to exponentially decline in November and reached its original level in May 1999. The structure of the active region remained almost the same as it was at the epoch 1995.6. Figure 5 shows the structure of the active region on March 21, 1998. It includes the bipolar outflow and the two bullets. As previously, the bullets have a cometary shape. However, in this case, the head of the comet is in front of its tail, which is indicative of its fairly high velocity. The bipolar outflow is highly collimated and is 2.5×0.2 AU in size (Figs. 5 and 6). The rise in the H_2O maser emission was caused by the increase in the brightness of the structure by more than three orders of magnitude. The brightness temperatures of the bipolar outflow and the injector rose to $T_b \approx 10^{15}$ K and $T_b \approx 5 \times 10^{16}$ K, respectively.

Analysis of the parameters of the structure for the entire period of its activity showed that the relative radial velocities of the flows are $V_{NW_{||}} = -0.3$ km s^{-1} and $V_{SE_{||}} = 0.3$ km s^{-1}. In the plane of the sky, the flow velocities in the period preceding the enhanced activity were $V_{NW_\perp} = 10$ km s^{-1} and $V_{SE_\perp} = 8$ km s^{-1}; they reached $V_{NW_\perp} = 6.8$ km s^{-1} and $V_{SE_\perp} = 5.0$ km s^{-1} at the emission peak and then decreased to $V_{NW_\perp} = 4.0$ km s^{-1} and $V_{SE_\perp} = 3.5$ km s^{-1} in the period of decline in activity. Thus, the high and low velocities precede the high activity and the decline in emission, respectively. The observed correlation of the supermaser emission with the flow velocity suggests collisional pumping, the interaction of the flow with the ambient medium.

The bipolar outflow has a spiral structure that is determined by the precession of the rotation axis of the injector; the precession period is $T \approx 10$ yr,

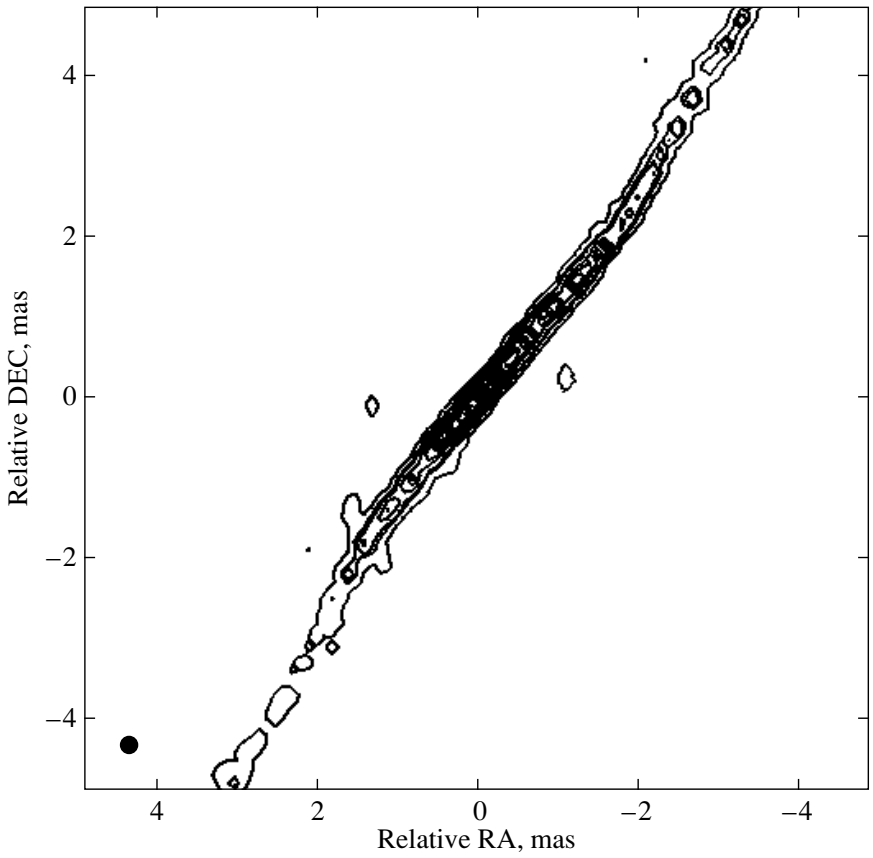

Fig. 6. Bipolar outflow (the epoch is October 14, 1998) with an angular resolution of 0.15 mas.

and the precession angle is ∼16° (Matveyenko *et al.* 2004).

At the end of the period of high activity under consideration, a toroidal structure seen edge-on showed up in the central part around the injector. Previously, the supermaser emission blended the image of the torus. The dynamic range of the measurements was not enough to reveal a structure of relatively low brightness. The plane of the torus is perpendicular to the plane of the injector axis. The torus is 1.2 AU in diameter, and its brightness temperature reaches $T_\mathrm{b} \approx 10^{13}$ K (Fig. 7).

INTERPRETATION OF THE RESULTS

The observed highly organized structure, the chain of bright compact features distributed along the elongated S-shaped structure, corresponds to an accretion disk separated into protoplanetary rings seen edge-on. The disk is 27 AU in diameter and 0.3 AU in thickness. The separation of the accretion disk into rings suggests a differential rotation velocity of the rings, Keplerian motion. However, the observed velocity distribution of the features (the rings) corresponds to a rigid-body rotation, $V_\mathrm{rot} = \Omega R$. The rotation period of the rings is 170 yr.

The maser rings result from the sublimation of ice granules in the protoplanetary rings. The water molecules are blown away by radiation pressure and stellar wind to form halos around the rings (Fig. 8). The maser radiation is concentrated in the azimuthal plane of the rings; its directivity reaches 10^{-3}.

The bipolar outflow of particles is formed through the transfer of the rotational kinetic energy of the disk to the flow. The energy of the rings is proportional to the square of their rotation velocity, $\sim m_\mathrm{ring} V_\mathrm{rot}^2/2$. The energy transfer will cause the Keplerian velocity $V^2R = MG$ to decrease. The loss of the rotation velocity increases as one approaches the central body. The matter density in the rings is $\sim R^{-2}$. The mass and kinetic energy of the accreting matter and the disk is probably transferred to the bipolar outflow in the central part of the disk ∼15 AU in diameter, which determines its rigid-body rotation. The velocity of the bipolar outflow is $V = 4$–10 km s^{-1}. The apparent residual rotation velocity of the rings is $V_\mathrm{rot} =$

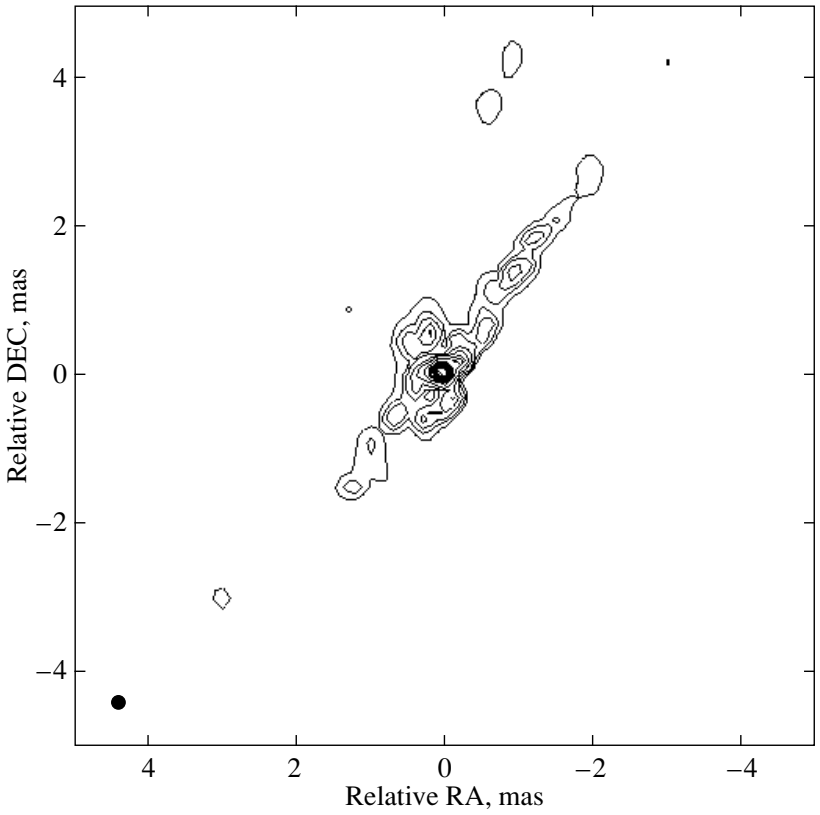

Fig. 7. Fine structure of the active region at the epoch of decline in activity (April 24, 1999) with an angular resolution of 0.15 mas.

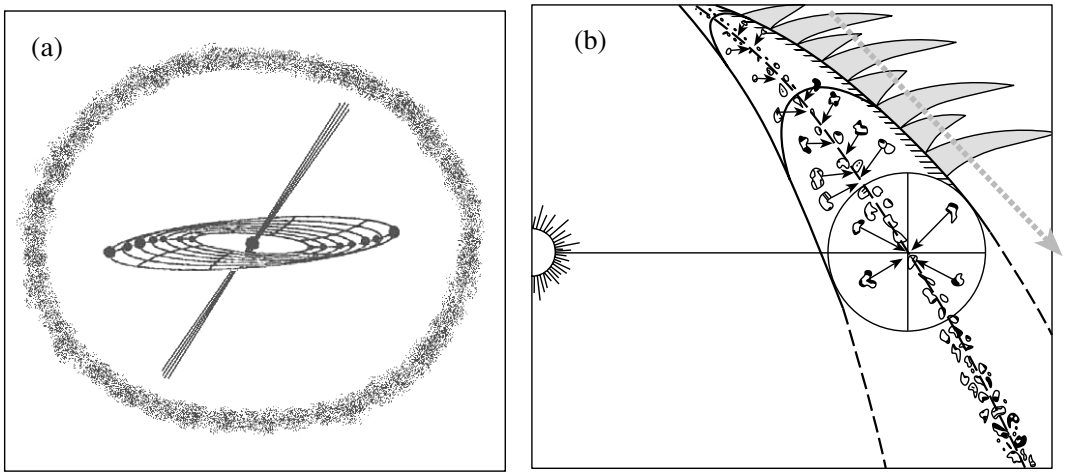

Fig. 8. (a) Model for the structure of the active region in Orion KL: an accretion disk separated into protoplanetary rings, a bipolar outflow, and an envelope; (b) one of the rings surrounded by a halo of H_2O sublimated molecules (a maser ring) is shown on an enlarged scale.

0.2–1.2 km s^{-1}, depending on the distance. The diameter of the injected flow does not exceed 0.05 AU. This quasi-stationary structure, which consists of an accretion disk and a bipolar outflow surrounded by an envelope, accompanies the initial star formation stage (Fig. 8). The envelope amplifies the emission at $V = 7.65$ km s^{-1} in a $\sim$0.5 km s^{-1} band by more than two orders of magnitude.

CONCLUSIONS

Our studies of the superfine structure of one active region in Orion KL in H_2O maser emission have shown the following.

(1) Intense H_2O maser emission accompanies the formation of a thin accretion disk, a highly collimated bipolar outflow, and an envelope (Fig. 8).

(2) The disk is 27 AU in diameter and ~0.3 AU in thickness. The disk is separated into protoplanetary rings containing ice granules. Radiation and stellar wind sublimate and blow away the water molecules to a form halo around each ring. The radiation from the maser rings is concentrated in the azimuthal plane and has a high directivity, $\leq 10^{-3}$.

(3) The central part of the disk ~15 AU in diameter rotates as a rigid body; the rotation period is $T =$ 170 yr. The kinetic energy of the accreting matter and the disk is partially transferred to the bipolar outflow, causing a deviation from Keplerian motion.

(4) The injector is surrounded by a toroidal structure 1.2 AU in diameter. The diameter of the injected flow is ~0.05 AU.

(5) The highly collimated bipolar outflow ~0.1 AU in thickness and ~3 AU in apparent length has a spiral structure determined by precession. The precession period is ~10 yr, and the precession angle is ~16°. The flow velocity in the active period reaches 10 km s^{-1}.

(6) The surrounding medium (the envelope) amplifies the emission at $V = 7.65$ km s^{-1} in a ~0.5 km s^{-1} band by more than two orders of magnitude, which determines the supermaser emission.

(7) The maser emission has a high degree of linear polarization determined by the pumping directivity.

ACKNOWLEDGMENTS

L.I. Matveyenko thanks the Russian Foundation for Basic Research (project no. 05-02-16135), the "Nonstationary Objects" program of the Presidium of the Russian Academy of Sciences, the "Extended Objects" program of the Russian Academy of Sciences, the Max-Planck-Institut für Radioastronomie, and the Nuffield Radio Astronomy Observatory for hospitality and support.

REFERENCES

1. Z. Abraham, N. L. Cohen, R. Opher, *et al.*, Astron. Astrophys. **100**, L10 (1981).
2. B. F. Burke, K. J. Johnston, V. A. Efanov, *et al.*, Astron. Zh. **49**, 465 (1970) [Sov. Astron. **16**, 379 (1970)].
3. V. A. Demichev and L. I. Matveyenko, Astron. Rep. **48**, 979 (2004).
4. G. Garay, J. M. Moran, and A. D. Hashick, Astrophys. J. **338**, 244 (1989).
5. R. Genzel, D. Downs, J. M. Moran, *et al.*, Astron. Astrophys. **66**, 13 (1978).
6. L. I. Matveyenko, L. R. Kogan, and V. I. Kostenko, Pis'ma Astron. Zh. **6**, 505 (1980) [Sov. Astron. Lett. **6**, 279 (1980)].
7. L. I. Matveyenko, Pis'ma Astron. Zh. **7**, 100 (1981) [Sov. Astron. Lett. **7**, 54 (1981)].
8. L. I. Matveyenko, D. A. Graham, and P. J. Diamond, Pis'ma Astron. Zh. **14**, 1101 (1988) [Sov. Astron. Lett. **14**, 468 (1988)].
9. L. I. Matveyenko, Pis'ma Astron. Zh. **20**, 456 (1994) [Astron. Lett. **20**, 388 (1994)].
10. L. I. Matveyenko, P. J. Diamond, and D. A. Graham, Pis'ma Astron. Zh. **24**, 723 (1998) [Astron. Lett. **24**, 623 (1998)].
11. L. I. Matveyenko, K. M. Zakharin, P. J. Diamond, and D. A. Graham, Pis'ma Astron. Zh. **30**, 121 (2004) [Astron. Lett. **30**, 100 (2004)].
12. L. I. Matveyenko, V. A. Demichev, Ph. D. Diamond, and D. A. Graham, in *Symposium IAU No. 227: Massive Star Birth: A Crossroads of Astrophysics, Italy, 2005,* Ed. by Churchwell and Malcolm Walmsley.

Translated by V. Astakhov

Astronomy Letters, Vol. 31, No. 12, 2005, pp. 824–831. Translated from Pis'ma v Astronomicheskiĭ Zhurnal, Vol. 31, No. 12, 2005, pp. 922–930.

Study of the Apsidal Motion in the Eclipsing Binary MZ Lac

V. S. Kozyreva[1]*, A. V. Kusakin[1], and M. Wolf[2]

[1] *Sternberg Astronomical Institute, Universitetskiĭ pr. 13, Moscow, 119992 Russia*

[2] *Astronomical Institute, Charles University, V Holešovičkách 2, Prague 8, 18000 Czech Republic*

Received May 11, 2005

Abstract—A series of highly accurate photoelectric observations of the eclipsing binary MZ Lac was obtained with a 48-cm AZT-14 reflector at the Tien-Shan High-Altitude Station of the Sternberg Astronomical Institute from 1985 to 2004 to study its apsidal motion. We constructed a consistent system of physical and geometrical parameters of the components and the binary's orbit: we determined their masses ($M_1 = 1.50M_\odot$, $M_2 = 1.29M_\odot$), radii ($R_1 = 1.86R_\odot$, $R_2 = 1.35R_\odot$), luminosities ($L_1 = 0.79L_\odot$, $L_2 = 0.45L_\odot$), surface gravities ($\log g_1 = 4.06$, $\log g_2 = 4.27$), age ($t = 1.9 \times 10^9$ yr), and the distance to the binary ($d = 510$ pc). The binary exhibits apsidal motion with the period $U_{\rm obs} = 480 \pm 40$ yr, while its theoretically expected value is $U_{\rm th} = 450 \pm 40$ yr. Spectroscopic studies of MZ Lac and calculations of the absolute parameters of the components are required to test our conclusions. © *2005 Pleiades Publishing, Inc.*

Key words: *eclipsing binaries, apsidal motion, apsidal-motion parameter, photometric elements.*

INTRODUCTION

Observations of the apsidal motion in eclipsing binaries provided a wealth of information to test theoretical models for the internal structure of stars at various evolutionary stages. The work on the determination of apsidal periods was begun more than 70 years ago, and Y Cyg was the first object in which this motion was searched for. At present, the number of objects for which at least one determination of the apsidal period was published exceeds 120 (Petrova and Orlov 1999). Unfortunately, however, reliable determination of the apsidal period confirmed by other studies have been made so far for less than half of the binaries in this list. The set of observational data on each of these binaries is important in any case, even after the determination of its apsidal period, since, occasionally, for example, through analysis, a third body can be discovered in the binary under study, or instability of the component stars will be revealed. MZ Lac is the eclipsing binary that became the object of our studies.

The eclipsing binary MZ Lac (GSC 3983.1644; Sp = A9.5V + F3.5V; $V_{\max} = 11\overset{m}{.}56$) was discovered by Miller and Wachmann (1971) based on the reduction of photographic plates from the Vatican Observatory. The shift of the secondary minimum from a phase of 0.5 ($\phi_{\rm II} = 0\overset{\rm p}{.}713$) pointed to a high orbital eccentricity. These authors estimated the spectral type of MZ Lac to be A0.

MZ Lac was studied in detail by Šilhán (1990, 1992) using plates from the Sonneberg plate collection. Analyzing the plates taken from 1927 to 1988, the author derived a number of times of minima. He determined the star's new linear ephemerides, discovered its apsidal motion, and estimated the apsidal period ($U = 570 \pm 170$ yr) and the orbital eccentricity ($e = 0.47 \pm 0.12$) rather accurately.

Wolf *et al.* (1998) studied all of the times of minima found by Šilhán and ten times of minima computed from the photoelectric light curves obtained from 1985 to 1996 at the Tien-Shan Observatory and from the CCD observations at the Ondřejov Observatory (Czech Republic) and the Metzerlen Observatory (Switzerland), a total of 101 times of minima, using a method based on analysis of the $O-C$ diagram (Gimenez and Garcia-Pelayo 1982). The following ephemerides of the primary minimum were derived:

Min I = HJD2438264.3452 + 3.1588204E, the eccentricity $e = 0.421 \pm 0.005$, and the apsidal period $U = 444 \pm 25$ yr.

In this study, our objective was to compute the photometric elements from the light curves of MZ Lac, to determine the rate of apsidal motion, and to compare the result with the theoretical value obtained from evolutionary stellar models.

Unfortunately, there are no spectroscopic observations of MZ Lac; therefore, there are no data on the spectral types and masses of the components. This makes it very difficult to compare the parameters derived from observations with their values computed

*E-mail: valq@sai.msu.ru

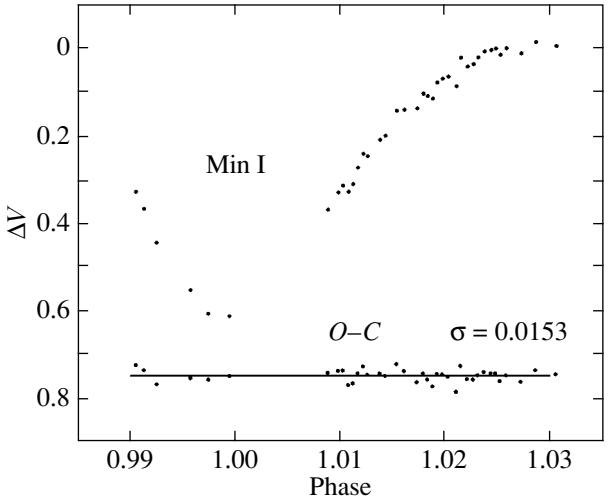

Fig. 1. V-band light curve of MZ Lac near the primary minimum from our photoelectric observations in 1985. The residuals of the observations (O) from the theoretical curve (C) constructed with the photometric elements from Table 2 are given at the bottom.

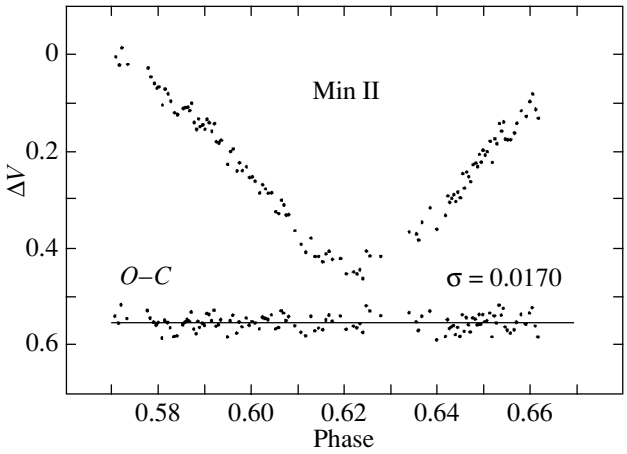

Fig. 2. Same as Fig. 1, but near the secondary minimum.

using the theory of stellar evolution, but we made an attempt to do this.

OBSERVATIONS

The first photoelectric measurements of MZ Lac in the $WBVR$ photometric system were performed by V.S. Kozyreva in 1985 using a 48-cm AZT-14 reflector at the Tien-Shan High-Altitude Observatory of the Sternberg Astronomical Institute (Moscow State University). Subsequently, the measurements at this observatory were continued in the period 1992–2004 with the same instrumentation and mainly with the same comparison star, GSC 3983.911. Only the observations in December 1992 were carried out with the comparison star GSC 3983.1656 using a Zeiss-1000 telescope. The star 2MASS22280135 + 5340557 lies at a distance of $\sim 6''$ from MZ Lac; it is fainter than MZ Lac by more than $3^m.5$ in the V band. For the overwhelming majority of our photometric observations, this star was measured together with MZ Lac, except the Zeiss-1000 observations on September 1, 1992. On this night, the observations were carried out in the V band alternately with two apertures; the contribution from the neighboring object is almost equal to zero in the smaller aperture, while in the larger aperture both objects were observed together. A comparative analysis of these measurements showed that the contribution from the neighboring object to the total (including MZ Lac) light in the V band is $\sim$3%. This result was confirmed by our light-curve solution (see Table 2 below).

The results of our differential measurements of MZ Lac are accessible on the web page http://lnfm1.sai.msu.ru/~valq (broad-band photometry). They were corrected for atmospheric extinction using a technique described by Moshkalev and Khaliullin (1985) and reduced to the system of the $WBVR$ catalog (Kornilov *et al.* 1991). The light curves of MZ Lac near its primary and secondary minima constructed from our V-band observations in 1985 are shown in Figs. 1 and 2, respectively. The $O-C$ residuals of the individual observational data points from the theoretical curve constructed with our derived photometric elements are given at the bottom. The $O-C$ values exhibit no systematic deviations from the mean.

In addition to the photoelectric observations, Wolf obtained V- and R-band CCD data at the primary and secondary minima of MZ Lac at the Ondřejov Observatory (Czech Republic) and the Metzerlen Observatory (Switzerland) in 2001 and 2002.

PHOTOMETRIC AND ABSOLUTE ELEMENTS

To derive the magnitudes of MZ Lac and the comparison star GSC 3983.911 in the standard $WBVR$ system, we performed simultaneous observations of these stars and standard stars from the *Catalog of WBVR Magnitudes for Bright Stars of the Northern Sky* (Kornilov *et al.* 1991). The magnitudes of the other comparison star, GSC 3983.1656, given in Table 1 were derived from the differences between its $WBVR$ magnitudes and those of the comparison star GSC 3983.911. We used two-color diagrams based on the catalog to estimate the spectral types of the comparison stars and the components of MZ Lac (Table 1).

Despite the rather large number of observations at the minima collected by the authors over the entire

Table 1. Magnitudes, color indices, and spectral types of MZ Lac and the comparison stars obtained using standard stars from the $WBVR$ catalog as reference objects

Star	W	B	V	R	Sp
MZ Lac	12.12(4)	12.03(3)	11.56(2)	11.23(3)	A9V+F3V
GSC 3983.911	10.70(3)	10.76(3)	10.41(3)	10.09(3)	F2V
GSC 3983.1656	15.45(7)	13.65(5)	12.03(5)	10.79(5)	K8III

Table 2. Photometric elements of MZ Lac derived by analyzing the V-band observations of different authors in an independent search for r_1, r_2, and e (the first column) and at fixed r_1, r_2, and e (the remaining columns)

Parameter	Kozyreva 1985 (V)	Kozyreva 1993 (V)	Wolf and Kusakin 2002–2004 (V)	Wolf and Kozyreva 2002–2004 (V)
$\mathbf{r}_1$	0.138(2)	"	"	"
r_1	0.110(2)	"	"	"
i	88°.4(2)	88°.7(5)	88°.0(5)	87°.4(6)
e	0.420(3)	"	"	"
ω	64°.6(3)	69°.9(5)	77°.1(6)	76°.5(6)
L_1	0.630(10)	0.66(2)	0.61(2)	0.62(3)
L_2	0.340(10)	0.34(2)	0.38(3)	0.35(3)
u_1	0.45 (fixed)	"	"	"
u_2	0.45 (fixed)	"	"	"
$r_1 + r_2$	0.248	"	"	"
L_2/L_1	0.540	0.524	0.628	0.557
J_2/J_1	0.844	0.806	0.975	0.883
$k = r_2/r_1$	0.797	"	"	"
σ_{O-C}	$0^m.016$	$0^m.025$	$0^m.015$	$0^m.021$

time interval, our first V-band photoelectric observations in 1985 (Figs. 1 and 2) turned out to be most complete and compact in time.

Since the reflection and ellipticity effects are negligible (<0.01), we used standard light-curve rectification methods (Martynov 1971).

Table 2 presents, in standard notation, the photometric elements of MZ Lac that we determined using a quasi-Newtonian method with analytical calculations of the derivatives of the functional as a minimizing algorithm for the photometric phase of the eclipses (Gill and Murrei 1978).

The binary's brightness at any time during the eclipse of one star by the other can be determined by analytical integration. At the contacts of the stellar disks, when the second derivatives change abruptly, the derivatives are calculated from an analytical expansion in terms of a small parameter. This method was used to derive the photometric elements of the eclipsing binary IT Cas (Kozyreva and Zakharov 2001).

The influence of the limb-darkening coefficients u_1 and u_2 on the brightness of the binary manifests itself in the segments of the light curve immediately adjacent to the points of contact of the stellar disks. Experience shows that, since these parameters affect weakly the light curve, they can be reliably determined only from observations with a high accuracy ($\sigma_{O-C} \leq 0^m.005$) and with the required completeness in these segments of the light curve. The accuracy of the light curves for MZ Lac is considerably lower; therefore, in our calculations, we used the theoretical values of u_1 and u_2 (Wade and Rucinski 1985) corresponding to the components' spectral types and the bands of the observations.

The set of photometric data for the star consists

Table 3. Relative luminosities L_1 and L_2, magnitudes m_1 and m_2, surface-brightness ratios J_2/J_1, and color indices for the primary (1) and secondary (2) components of MZ Lac derived by analyzing the $WBVR$ light curves

Parameter	W	B	V	R
L_1	0.66(4)	0.65(3)	0.63(2)	0.58(3)
L_2	0.34(4)	0.32(3)	0.34(2)	0.35(3)
L_2/L_1	0.515	0.492	0.540	0.603
$-2.5\log(L_2/L_1)$	0.72	0.77	0.67	0.55
m_{1+2}	12.12(4)	11.98(3)	11.51(2)	11.20(3)
m_1	12.57(5)	12.42(4)	11.98(3)	11.72(4)
m_2	13.29(5)	13.19(4)	12.65(3)	12.26(4)
J_2/J_1	0.805	0.769	0.844	0.942
Component	$W-B$	$B-V$	$B-R$	$V-R$
Primary	0.16(5)	0.44(4)	0.70(3)	0.26(4)
Secondary	0.11(5)	0.54(4)	0.92(3)	0.39(4)

of a series of high-quality observations at the secondary minima, but the observations at the primary minima are fragmentary: there are no observation that would completely cover both branches of the minimum. This can introduce systematic errors into the photometric elements derived by analyzing such data. We used the method of a free search for all elements only for the minima of 1985, since these data cover better the light curve than all of the remaining observations and have a comparatively small error of individual measurements (σ_{O-C}) without any systematic deviations from the mean. The results of our calculations are presented in the second column of Table 2. Below, we fixed the stellar radii and the orbital eccentricity derived in these calculations. The results of our analysis of the light curves obtained in different years are given in columns 3–5 of Table 2. The last two columns were computed for the data set composed of the CCD observations of a primary minimum obtained by M. Wolf in 2002 and the photoelectric observations of two secondary minima performed in September 2004 by V.S. Kozyreva and in December 2004 by A.V. Kusakin. We see from the table that the binary exhibits a rapid apsidal motion (variation in the periastron longitude ω).

The observations in 1985 were performed mainly in the V band, but, in addition, there are observations in the W, B, and R bands outside and inside the secondary minimum. This allowed us to find light-curve solutions for MZ Lac for fixed geometry of the binary, which are presented in Table 3 together with the data for the V band. The geometrical parameters were fixed at the values in the second column of Table 2, since there is no reason to believe that these parameters can depend on the spectral band of the observations. This implies that, when analyzing our multicolor measurements, we varied only the relative luminosities of the components (L_1 and L_2); the linear limb-darkening coefficients (different for different components and different spectral bands) were fixed at their theoretical values (Wade and Rucinski 1985). Using the solutions given in Table 3 and the two-color diagram based on the $WBVR$ catalog mentioned above, we can estimate the spectral types of the components. The derived $W-B$, $B-V$, and $V-R$ colors of the components correspond most closely to A9V and F3V stars for the primary and secondary components, respectively.

Unfortunately, no spectroscopy is available for the binary; therefore, to estimate the masses of the components, we have to use a semiempirical method (Khaliullin 1985) based on the photometric elements and the effective temperatures of the components. Assuming the effective temperature for the primary (Straizys 1982) to correspond to its spectral type (Table 1) and using the surface-brightness ratio of the components J_2/J_1 (Table 3), we can determine the effective temperature of the secondary component from the Planck function. Since the observations were performed mainly in the V band, we took J_2/J_1 calculated for these observations (Table 3, column 4).

Using the derived masses as input parameters and taking into account all of the remaining data on the components computed above, we can find the positions of the stars on the evolutionary tracks by the method of successive approximations from the stellar models by Claret and Gimenez (1989, 1992), given that the ages of the components are equal with a high

Table 4. Basic physical and geometrical parameters of the eclipsing binary MZ Lac and its components

Parameter, units	Primary	Secondary
Mass $M/M_\odot$	1.50 ± 0.05	1.29 ± 0.04
Radius $R/R_\odot$	1.86 ± 0.15	1.35 ± 0.10
Luminosity $\log(L/L_\odot)$	0.79 ± 0.05	0.45 ± 0.04
Effective temperature T, K	6610 ± 70	6380 ± 90
Spectral type Sp	A9V	F3V
Surface gravity, $\log g$	4.06 ± 0.07	4.27 ± 0.04
Apsidal parameter, $\log k_2$	-2.489^{+25}_{-5}	-2.226^{+13}_{-40}
Bolometric absolute magnitude $M_{\rm bol}$	$2\overset{m}{.}75 \pm 0\overset{m}{.}12$	$3\overset{m}{.}60 \pm 0\overset{m}{.}15$
Visual absolute magnitude M_v	$2\overset{m}{.}76 \pm 0\overset{m}{.}12$	$3\overset{m}{.}60 \pm 0\overset{m}{.}15$
Relative radius r, a	0.1380 ± 0.0015	0.1106 ± 0.0015
V	$11\overset{m}{.}98 \pm 0\overset{m}{.}03$	$12\overset{m}{.}65 \pm 0\overset{m}{.}03$
$W-B$	$0\overset{m}{.}16 \pm 0\overset{m}{.}05$	$0\overset{m}{.}11 \pm 0\overset{m}{.}05$
$B-V$	$0\overset{m}{.}44 \pm 0\overset{m}{.}04$	$0\overset{m}{.}54 \pm 0\overset{m}{.}04$
$V-R$	$0\overset{m}{.}26 \pm 0\overset{m}{.}04$	$0\overset{m}{.}39 \pm 0\overset{m}{.}04$
Color excess E_{b-v}	$0\overset{m}{.}156 \pm 0\overset{m}{.}007$	$0\overset{m}{.}153 \pm 0\overset{m}{.}007$
Extinction A_v	$0\overset{m}{.}53 \pm 0\overset{m}{.}02$	$0\overset{m}{.}52 \pm 0\overset{m}{.}02$
Orbital period P_a, days	3.1587715(5)	
Semimajor axis of relative orbit a, $R_\odot$	13.3 ± 1.1	
Orbital inclination, i, deg	$86\overset{\circ}{.}6 \pm 0\overset{\circ}{.}7$	
Theoretically expected apsidal period $U_{\rm th}$, yr	450 ± 40	
Observed apsidal period, $U_{\rm obs}$, yr	480 ± 40	
Age of binary t, yr	$(1.9 \pm 0.4) \times 10^9$	
Distance to binary d, pc	510 ± 40	

probability. The position of a star on the evolutionary track determines a number parameters: its luminosity (L), surface gravity (g), and apsidal parameter (k_2). These data, along with other absolute parameters of MZ Lac computed by taking them into account, are given in Table 4. To compute the data in Table 4, we used information from Table 1 as well as the normal colors and color excesses corresponding to the spectral types of the components from the tables by Straizys (1977).

Our calculations yielded the following masses of the components: $M_1 = (1.50 \pm 0.05)M_\odot$ and $M_2 = (1.29 \pm 0.04)M_\odot$, which, within the error limits, correspond to the masses of stars of their spectral types tabulated by Straizys (1982).

Figure 3 shows the $\log g(t)$ diagram, i.e., the evolutionary tracks for stars of normal chemical composition ($Z = 0.02$) and with masses of $M_1 = (1.50 \pm 0.5)M_\odot$ and $M_2 = (1.29 \pm 0.4)M_\odot$ constructed by Claret and Gimenez (1992). This diagram was chosen to determine the age, because the gravity ($g \propto M/R^2$) is very sensitive to the age and because the radii required to compute it are determined from the light curves more accurately than, for example, the luminosities or other stellar parameters. In this diagram, the widths of the bands of the components' evolutionary tracks reflect the uncertainties in their masses. The intersection of the evolutionary track with the $y = \log g_{\rm obs}$ straight line gives the sought-for stellar age. The ages of the components determined in this way are in good agreement. Since the age of the primary component can be determined more accurately, and we took it as the age of the binary MZ Lac:

$$t = (1.9 \pm 0.4) \times 10^9 \text{ yr}.$$

This age of MZ Lac suggests that the component stars have not yet gone far from the zero-age main sequence, although the rather high orbital eccen-

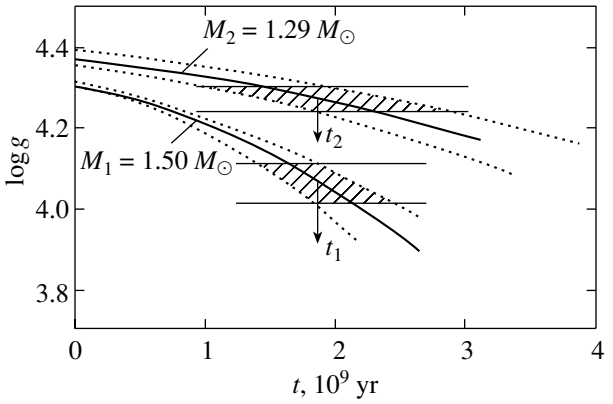

Fig. 3. Evolutionary tracks in the $\log g - t$ diagram for stars with normal chemical composition ($Z = 0.02$) and with masses of $M_1 = (1.50 \pm 0.05)M_\odot$ and $M_2 = (1.29 \pm 0.05)M_\odot$ corresponding to the masses of the components of MZ Lac to determine their ages t_1 and t_2.

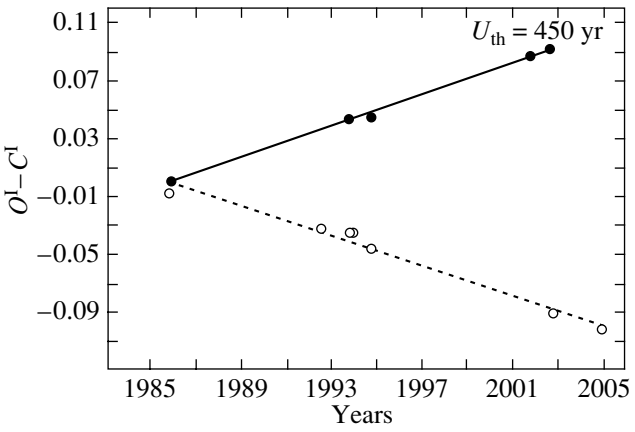

Fig. 4. Time dependence of $(O-C^{\rm I})$. Here, $(O-C^{\rm I})$ are the residuals of the observed times of the primary (filled circles) and secondary (open circles) minima of MZ Lac from the linear ephemerides (2).

tricity ($e = 0.42$) may point to a younger age of the binary, when it only approaches the main sequence. The orbits of the stars in binaries are known to tend to become circular during their evolution (Zahn 1977).

APSIDAL MOTION

Since the minima of light curves with elliptical orbits are asymmetric, different methods for determining the times of minima and different parts of the minima yield different results due to intrinsic brightness fluctuations and measurement errors.

For an ideal eclipsing binary of two spherical stars without any intrinsic brightness fluctuations and measurement errors, the times of conjunctions coincide with those of primary (Min I) and secondary (Min II) minima. Recall that the conjunctions of an eclipsing star are the positions at which the projected separations between the centers of the binary's components are at a minimum. To determine the times of conjunctions, we used the entire set of measurements of the minima supplemented with additional information from the solutions of other light curves by assuming that some of the elements were constant. In our opinion, this technique allows the times of conjunctions to be determined more accurately than in the case where the times of brightness minima are obtained using only the data points on the light curve of an individual brightness minimum.

When the individual (often incomplete) light curves are solved, there is no need to search for all photometric elements. Therefore, some of them may be fixed in accordance with the solution of the most complete and accurate light curve for the eclipsing variable in question.

Since the star's out-of-eclipse brightness exhibits a rather large spread, $\delta m \approx 0\overset{m}{.}03$, which is probably attributable to the variability of either the star MZ Lac itself or the comparison star GSC 3983.911, we varied the relative luminosities of the components (L_1 and L_2) and the binary's out-of-eclipse brightness (m_V^0). The main sought-for parameters were the time of conjunction of the components at the primary eclipse (T_1) and the rate of change in the periastron longitude of the primary component ($\dot\omega$). Via the well-known relation from Kopal (1978) under the assumption of a linear change in the periastron longitude (ω),

$$T_2 = T_1 + \frac{P}{2} + \frac{2Pe\cos\omega}{\pi} - \frac{2Pe^3(1+3\sqrt{1-e^2})}{3\pi(1+\sqrt{1-e^2})^3}\cos 3\omega + \ldots, \quad (1)$$

$$\omega = \omega_0 + \dot\omega(t - t_0),$$

these quantities determine the time of the secondary conjunction (T_2). Here, P is the orbital period of the close binary, t is the time of the corresponding eclipse, and t_0 is the time the periastron longitude is equal to ω_0. These values of T_1 and T_2 are given in heliocentric Julian days in Table 5. To illustrate the behavior of the minima with time, T_1 and T_2 from Table 5 are shown in Fig. 3 in the form of $(O-C^{\rm I})$, where O are the observed values of T_1 and T_2, $C^{\rm I}$ are the theoretical times computed using the linear ephemerides for both minima, and E is the number of the minimum:

$$C_1^{\rm I} = {\rm JD}_\odot 2446442.5299 + 3.1587715E, \quad (2)$$

$$C_2^{\rm I} = {\rm JD}_\odot 2446444.5060 + 3.1587715E.$$

We see from Fig. 4 that the repetition periods of the primary, P_1, and secondary, P_2, eclipses differ

Table 5. Observed heliocentric times of the primary (I) and secondary (II) minima of MZ Lac.

$JD_\odot$ 2400000+	$O-C^{II}$	Min	Author, year	$JD_\odot$ 2400000+	$O-C^{II}$	Min	Author, year
46354^d.08527	0^d.00093	I	Kozyreva, 1985	48867.25021	0.00206	II	Kozyreva, 1985
49244.40475	0.00158	I	Kozyreva, 1993	49224.18934	0.00510	II	Kozyreva, 1993
49623.45760	−0.00378	I	Kozyreva, 1994	49246.30073	0.00541	II	Kozyreva, 1993
52188.42245	0.00053	I	Wolf, 2001	49622.18398	0.00620	II	Kozyreva, 1994
52507.46337	0.00079	I	Wolf, 2002	52569.27274	−0.00286	II	Kozyreva, 2004
46340.26041	−0.00653	II	Kozyreva, 1985	53324.20935	−0.00188	II	Kusakin, 2004

Note. Here, $(O-C^{II})$ are the residuals of the observations from ephemerides (3).

markedly, because the $(O-C^{I})$ values for different minima begin to differ greatly with time. The reason is known to be the rotation of the major axis of the elliptical orbit (the line of apsides) in the binary. In this case, the $(O-C^{I})$ values undergo out-of-phase long-period variations for Min I and Min II. However, since the apsidal period is much longer than the interval of the photoelectricobservations, the $(O-C^{I})$ variations for both Min I and Min II can be represented as linear relations without any appreciable loss of accuracy. The following linear ephemerides were obtained by the least-squares method:

$$\begin{aligned} C_1^{II} &= JD_\odot 2446354.0845 \ \ +3.1587764E, \\ &\qquad\pm 2 \qquad\qquad\ \pm 2 \\ C_2^{II} &= JD_\odot 2446356.0606 \ \ +3.1587473E. \\ &\qquad\pm 4 \qquad\qquad\ \pm 12 \end{aligned} \tag{3}$$

The $(O-C^{II})$ values computed with these ephemerides are also presented in Table 5.

According to the derived ephemerides (3), the difference between the periods of the primary (P_I) and secondary (P_{II}) minima is

$$\Delta P = P_I - P_{II} = 0^d.0000291 = 2^s.51 \pm 0^s.10. \tag{4}$$

The theory of apsidal motion yields the following relation for the difference between the periods P_I and P_{II} (Rudkjobing 1959):

$$\frac{\Delta P}{P} = \frac{2P\sqrt{1-e^2}}{\pi(1-e^2\sin^2\omega)^2} e(1-e^2)\sin\omega\frac{d\omega}{dt}. \tag{5}$$

Substituting our values of ΔP and P, along with the eccentricity e and the periastron longitude ω, into this relation yields the rate of apsidal motion: $\dot\omega_{obs} = 75^\circ \pm 6^\circ$ per 100 yr.

At the same time, the theoretically expected rate of apsidal motion computed with the parameters (Tables 2–4) found for this binary is

$$\dot\omega_{th} = \dot\omega_{cl} + \dot\omega_{rel} = 80^\circ \pm 7^\circ \quad \text{per} \quad 100 \quad \text{yr}.$$

Based on this solution, we found the mean apsidal parameter k_2 derived from observations and computed using the data from Tables 2 and 3 under the assumption of equal orbital and rotational velocities of the component stars to be $k_2^{obs} = 0.0051 \pm 0.0005$.

Table 4 presents the logarithms of the apsidal parameters k_2 for both components of MZ Lac determined from the tables by Claret and Gimenez (1992). For the primary and secondary components, they were found to be $k_2^1 = 0.0032$ and $k_2^2 = 0.0059$, respectively. To compare them with the parameter k_2^{obs} derived from observations, it is necessary to calculate the contribution from each component. It is equal to the reciprocal of the coefficients $S_1$and S_2, which depend on the binary's geometrical and physical parameters as follows:

$$S_i = r_i^5\left[\frac{m_{3-i}}{m_i}15f(e) + \left(\frac{\omega_{r,i}}{\omega_k}\right)^2\left(1+\frac{m_{3-i}}{m_i}\right)g(e)\right], \tag{6}$$

where

$$f(e) = \left(1+\frac{3}{2}e^2+\frac{1}{8}e^4\right)\frac{1}{(1-e^2)^5},$$
$$g(e) = (1-e^2)^{-2}.$$

Here, r_i, m_i, and $\omega_{r,i}$ are the relative radii, masses, and angular velocities of axial rotation of the components, respectively; e is the orbital eccentricity; and

ω_k is the mean angular velocity of orbital motion. The vectors of the axial rotation and the orbital motion are assumed to be parallel. Since there are no data on these velocities, we assume that the motion is synchronous and that the velocity ratio is equal to unity.

Thus, we can calculate the theoretical value of $k_2^{\rm th}$ from the formula

$$k_2^{\rm th} = \frac{S_1 k_{2,1}^{\rm th} + S_2 k_{2,2}^{\rm th}}{S_1 + S_2}. \qquad (7)$$

For MZ Lac, we obtained almost equal weights for both components, $S_1 = 2.74$ and $S_2 = 3.18$, and, hence, the weighted mean parameter is $k_2^{\rm tr} = 0.0047 \pm 0.0005$.

Thus, we see that the observed, $k_2^{\rm obs}$, and computed, $k_2^{\rm th}$, parameters are in good agreement.

CONCLUSIONS

The eclipsing binary MZ Lac is a system with a rather large, reliably determined orbital apsidal motion. Our calculations of the magnitudes and colors for the components ($W-B$, $B-V$, and $V-R$) in the standard system based on its comparison with standard stars from the $WBVR$ catalog of northern-sky stars (Kornilov *et al.* 1991) allowed us to estimate the spectral types of the components from two-color diagrams ($W-B$, $B-V$; $B-V$, $V-R$). The star consists of two components of spectral types A9V and F3V rather than A0, as suggested by Miller and Wachmann (1971). The photometric elements found from our light-curve solution, along with the estimated spectral types of the components, made it possible to compute their masses and effective temperatures. Using the evolutionary tracks by Claret and Gimenez (1992) under the assumption of equal ages for both components, we were able to refine the derived effective temperatures and masses of the stars and other absolute parameters of the binary: the luminosity, the surface gravity, and the apsidal parameter k_2, which characterizes the concentration of matter to the stellar center. The theoretical parameter $k_2^{\rm th}$ is almost equal, within the error limits, to the apsidal parameter found from observations $k_2^{\rm obs}$.

This leads us to the following conclusion: to within the parameters that we found for MZ Lac, the theoretical calculations of stellar characteristics in the course of evolution performed by Claret and Gimenez (1992) for this binary are consistent with the observational data. Thus, if our computed masses and spectral types of the components closely agree with the results of spectroscopic observations, then this binary would be a good confirmation for the validity of the theory of stellar evolutionary tracks.

ACKNOWLEDGMENTS

This work is based mainly on observations performed at the Tien Shan High-Altitude Observatory, the operation of which is currently maintained by the indefatigable efforts of the entire staff of the Observatory and its director, K.S. Kuratov. The study was supported by a grant from the "Astronomy" federal science and technology program.

REFERENCES

1. A. Claret and A. Gimenez, Astron. Astrophys., Suppl. Ser. **81**, 1 (1989).
2. A. Claret and A. Gimenez, Astron. Astrophys., Suppl. Ser. **96**, 255 (1992).
3. M. Gill and R. Murrei, Math. Program. **14**, 349 (1978).
4. A. Gimenez and J. M. Garcia-Pelayo, in *Proceedings of the 68th Colloquium: Binary and Multiple Stars as Tracers of Stellar Evolution, Bamberg, West Germany, 1981,* Ed. by Z. Kopal and J. Rahe (Reidel, Dordrecht, 1982), pp. 37–46.
5. Kh. F. Khaliullin, Astrophys. J. **299**, 668 (1985).
6. Z. Kopal, *Dynamics of Close Binary Systems* (Reidel, Dordrecht, 1978).
7. V. G. Kornilov, I. M. Volkov, A. I. Zakharov, *et al.*, Tr. Gos. Astron. Inst. im. P. K. Shternberga **63**, 1 (1991).
8. V. S. Kozyreva and A. I. Zakharov, Pis'ma Astron. Zh. **27**, 834 (2001) [Astron. Lett. **27**, 712 (2001)].
9. D. Ya. Martynov, *Eclipsing Variable Stars* Ed. by V. P. Tsesevich (Nauka, Moscow, 1971) [in Russian].
10. W. J. Miller and A. A. Wachmann, Specola Vat. Ric. Astron. **8**, 220 (1971).
11. V. G. Moshkalev and Kh. F. Khalliulin, Astron. Zh. **62**, 393 (1985) [Sov. Astron. **29**, 227 (1985)].
12. A. V. Petrova and V. V. Orlov, Astron. J. **117**, 587 (1999).
13. M. Rudkjobing, Ann. D'Astrophys. **22**, 111 (1959).
14. J. Silhan, J. Am. Assoc. Var. Star Obs. **19**, 12 (1990).
15. J. Silhan, Contrib. Nicholas Copernicus Obs. Brno **30**, 51 (1992).
16. V. Straizys, *Multicolor Stellar Photometry* (Mokslas, Vil'nyus, 1977; Pachart Publ. House, Tucson, 1992).
17. V. Straizys, *Metal-Poor Stars* (Mokslas, Vil'nyus, 1982) [in Russian].
18. R. A. Wade and S. M. Rucinski, Astron. Astrophys. **60**, 471 (1985).
19. M. Wolf, R. Diethelm, V. S. Kozyreva, and L. Sarounova, Astron. Astrophys. **334**, 840 (1998).
20. J. P. Zahn, Astron. Astrophys. **57**, 383 (1977).

Translated by N. Samus'

Astronomy Letters, Vol. 31, No. 12, 2005, pp. 832–835. Translated from Pis'ma v Astronomicheskiĭ Zhurnal, Vol. 31, No. 12, 2005, pp. 931–934.

Manifestation of the 399-Day Variations in Solar Wind Parameters

N. G. Skryabin[1], V. E. Timofeev[1], L. I. Miroshnichenko[2], and S. N. Samsonov[1]*

[1] *Institute of Cosmophysical Research and Aeronomy, Siberian Division, Russian Academy of Sciences, pr. Lenina 31, Yakutsk, 677891 Russia*

[2] *Institute of Terrestrial Magnetism, Ionosphere, and Radiowave Propagation, Russian Academy of Sciences, Troitsk, Moscow oblast, 142190 Russia*

Received December 10, 2004

Abstract—Based on a large series ($N = 14\,038$) of daily solar wind densities, we obtained the fluctuation power spectrum. The spectrum shows that the 399-day variation (the synodic period of Jupiter) has the largest amplitude in the interval of periods from 20 to 800 days. It is second in magnitude only to the secular, 22-, and 11-year variations. The amplitudes of the 399-day variations in solar wind density, temperature, and speed were determined by a superposed-epoch analysis: ≈ 0.5 cm^{-3}, ≈ 8000 K, and 2.8 km s^{-1}, respectively, at a more than 95% confidence level. This leads us to conclude that Jupiter may affect the solar wind parameters, since only Jupiter has a 399-day periodicity in our planetary system.

Key words: *Sun, Jupiter, solar wind.*

INTRODUCTION AND FORMULATION OF THE PROBLEM

Jupiter is an intense source of high-energy (0.2–40 MeV) electrons. McDonald and Treinor (1979) provided their energy spectrum, which indicates that, on average, the injection of high-energy electrons by Jupiter exceeds the injection of such particles by the Sun by several orders of magnitude. Many papers have been published in which it is pointed out that intense Jovian electrons manifest themselves in the vicinity of the Earth (Chenette *et al.* 1974; Eraker 1982; Hill *et al.* 1974; Freegarden *et al.* 1974; Van Allen *et al.* 1975; Lopate 1991; Skryabin *et al.* 2001). This indirectly suggests that Jupiter can affect the solar wind parameters by injecting a considerable number of charged particles. This phenomenon has not yet been studied. Even the very fact of the manifestation of this effect has been barely covered in scientific literature. However, papers on this subject have appeared in recent years (Lopate 1991; Skryabin *et al.* 2001; Timofeev *et al.* 2003).

This paper is devoted to the detection of a correlation between the solar wind parameters and Jupiter's synodic period (399 days).

ANALYSIS OF THE OBSERVATIONAL DATA

Below, we analyze the observational data to reveal a 399-day variation in some of the solar wind parameters and to determine its amplitude and phase characteristics. For this purpose, we used the experimental series of daily solar wind densities (cm^{-3}), temperatures (K), and speeds (km s^{-1}) for the period from July 26, 1965, through December 31, 2003 (OMNI Database 2003). Each series consisted of $N = 14\,038$ daily values. Since these data had gaps, we wrote a program that allowed the segments with gaps to be replaced by the values obtained by linear interpolation between the gap ends. The gap lengths were mainly several days; i.e., they were considerably shorter than Jupiter's synodic period and even shorter than the period of the 27-day variations. Since we are interested in time intervals comparable to 399 days, one might expect the gaps to have no effect on the results of our analysis. Ten data points are enough to describe the 399-day variation. Even in the presence of gaps, the number of data points that describe the 399-day variation is more than three hundred. After this preliminary data reduction, we obtained the mean values for the solar wind density, temperature, and speed 7.45 cm^{-3}, 115 790 K, and 442 km s^{-1}, respectively.

Figure 1 shows the power spectrum constructed from the experimental data for the solar wind density fluctuations after this preliminary data reduction. As we see from the figure, the 399-day variation has the largest amplitude in the interval of periods 20–800 days. It is second in magnitude only to the secular, 22-, and 11-year variations and their higher modes. For comparison, this figure shows the 27-day

*E-mail: s_samsonov@ikfia.ysn.ru

and semi-annual (183-day) variations. The amplitude of the annual variation is much lower than that of the biannual one. It shows up as a dip before the 399-day variation (due to its low amplitude, the annual variation is not marked in the figure, but it is noticeable).

Interestingly, the 399-day variation, like other variations, is seen in Fig. 1 not as an isolated pulse, but as a packet of pulses distributed near the true value. This is because we observe the 399-day variation through the response of the medium, whose properties change all the time during Jupiter's synodic period. In each individual period, the response can be delayed by a greater or smaller value. Besides, the synodic period itself changes by ≈1–2%. If the computational scheme has a high resolution, then we will always have several pulses distributed near the true value due to such fluctuations.

This effect is prominent, for example, in the 27-day variation. This variation is associated with the formation of active regions on the Sun. They can be formed at any point along the circumference of the Sun from 0 to 2π radians almost uniformly. For their uniform distribution, the mean interval of the fluctuations in the period of the 27-day variations is equal to half the length of the circumference of the Sun, i.e., π radians, or, on the scale of Fig. 1, ∼13 days. Indeed, the half-width of the envelope around the 27-day variation is approximately equal to this value. The period of the 11-year variations also fluctuates about its mean value. However, the fluctuations do not show up in Fig. 1, because the resolution of any computational scheme decreases considerably at low frequencies (long periods).

The superposed-epoch technique averages out the small fluctuations of the periods. As a result, when the series in which the period fluctuations about their mean values manifest itself is processed by this technique, the mean period itself will be distinguished reliably, because all of the values are averaged during the superposition. In addition, in contrast to spectral analysis, this technique allows the amplitude, phase, and overall shape of the effect (a sine wave, a trident, an isolated pulse, etc.) to be determined. Therefore, in what follows, we will analyze the data by the superposed-epoch technique to determine the amplitude and phase of the effect. In this case, the fluctuations, the 27-day variations, the Forbush effects, flares, etc., should be taken into account.

The entire class of pulsations with periods up to ≈100 days (class-I variations) is of no importance in revealing the 399-day variation. However, if these pulsations are not removed, then, when the epochs are superposed, most of the pulsations will necessarily "leak" into the interval near the 399-day period. The class-II variations (the secular, 22-, and 11-year variations and their higher modes) have periods of ≈700 days or longer and exhibit a high power. If they are not subtracted, then they will necessarily affect the superposition results. To remove these

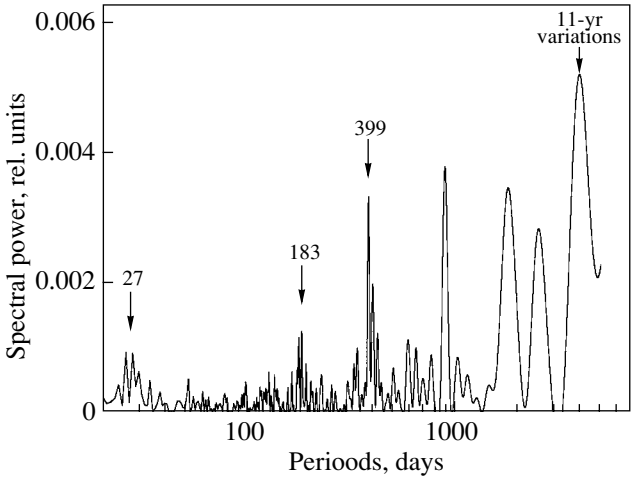

Fig. 1. Fluctuation power spectrum for the solar wind density in relative units.

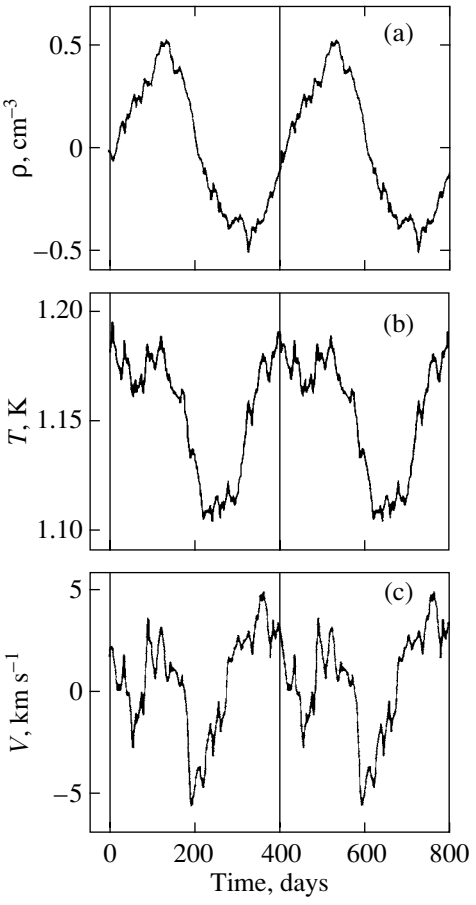

Fig. 2. General view of the effects obtained by the superposed-epoch technique: (a) the solar wind particle density in the Earth's orbit, (b) the solar wind particle temperature, and (c) the solar wind speed.

Earth–Jupiter opposition dates and reference point numbers

Date	Reference point number	Date	Reference point number	Date	Reference point number
December 17, 1965	145	February 24, 1980	5327	March 30, 1993	10 110
January 19, 1967	543	March 28, 1981	5725	May 1, 1994	10 507
February 21, 1968	941	April 26, 1982	6119	June 1, 1995	10 903
March 22, 1969	1336	May 25, 1983	6513	July 7, 1996	11 305
April 23, 1970	2128	June 30, 1984	6915	August 8, 1997	11 702
June 6, 1972	2528	August 4, 1985	7315	September 9, 1998	12 099
August 1, 1973	2929	September 10, 1986	7717	October 16, 1999	12 501
September 5, 1974	3329	October 18, 1987	8120	November 28, 2001	12 910
October 12, 1975	3731	November 22, 1988	8521	January 1, 2002	13 309
November 16, 1976	4132	December 27, 1989	8921	February 4, 2003	13 708
December 21, 1977	4532	January 29, 1991	9319		
January 23, 1979	4930	February 27, 1992	9713		

"unnecessary" variations, we have filtered all of the experimental data. The chosen filtering interval was 100–700 day. The filter is quite simple; it is the difference between two probabilistic trends with averaging over ≈100 and ≈700 day (this corresponds to the parameters of probabilistic trends with $\sigma = 25$ day and $\sigma = 175$ day).

The periods of the annual and 399-day variations differ by only ≈10%. To eliminate the annual variation, it was first found by the superposed-epoch technique in the filtered data for one period. Subsequently, using software, we obtained a series of 365-day variations ($N = 14\,038$) by adjunction, which was subtracted from the filtered data set. In this way, we reduced the data in all parameters. As a result, we obtained data sets in which the 399-day variation dominated and the 365-day variation was absent. To implement the superposed-epoch technique (in determining the 399-day variation), we first compiled a list of reference points, i.e., determined the ordinal numbers of the Jupiter–Earth opposition dates by taking July 26, 1965, as the first number. This list compiled from data of the *Astronomical Yearbook* for 1965–2002 is given in the table.

If we take the differences of the ordinal numbers (reference-point numbers), then we will obtain periods that, as can be seen from the table, will vary in the interval from 394 to 403 days, i.e., within ≈1.2% relative to the 399-day period. Such variations also introduce an additional number of small peaks to the "packet effect" in the spectrum of Fig. 1. Therefore, the number of such peaks near the 399-day period will increase even further. It is this picture that is seen in Fig. 1: a series of small peaks with different amplitudes is present in the vicinity of the 399-day period.

We perform the superposition relative to the reference point by assuming it to be the first number by a 399-day interval. Figure 2 shows the result (for clarity, two periods are shown). Figure 2a presents the superposition results for the solar wind density, Fig. 2b reflects the sum of the temperature in the superposition effect and its mean value, and Fig. 2c illustrates the effect on the solar wind speed. The solid vertical lines mark the opposition dates.

We estimated the effect of the neighboring variations as follows. We constructed sine waves with periods that differed from 399 days by 2, 5, and 10% with a series length of 14 038 values. Subsequently, we superposed them on the 399-day period. As a result, we found that their amplitudes decreased by factors of 3, 33, and 40, respectively. This means that the nearest variations that differ in period by 10% or more will decrease by more than a factor of 40 when superposed on the 399-day period. We carried out our calculations with and without the subtraction of the annual variation and obtained almost identical results. This is because the annual variations decreased by a factor of 40 when superposed on the 399-day period, while they were small anyway.

As we see from Fig. 2a, the total effect in the density variation is ≈1 cm^{-3} (this corresponds to a maximum variation amplitude of ≈0.5 cm^{-3}). The temperature (Fig. 2b) varies over the range (1.1–1.2) ×

10^5 K, and the solar wind speed (Fig. 2c) varies about 5.6 km s^{-1} (≈2.8 km s^{-1}). As percentages, these variations are ≈13 (6), ≈5 (2.5), and ≈1.3% (0.6%), respectively, for the above quantities. The errors were calculated using a technique that was specially developed for superposed-epoch technique (Jamison and Regal 1982). In Figs. 2a–2c, they are ±0.13 cm^{-3}, ±2107 K, and ±0.8 km s^{-1}, respectively. The effects shown in Fig. 2 exceed the errors by a factor of 4 (i.e., their amplitude is twice the errors). According to Jamison and Regal (1982), it thus follows that the above results were obtained at a more than 95% confidence level. Thus, based on our analysis of the experimental series for the solar wind density, temperature, and speed, we can assume that Jupiter's influence manifests itself in the solar wind parameters with a confidence higher than 95%.

CONCLUSIONS

(1) The synodic period of Jupiter is 399 days. No other source or process that produces this period is known to date. Since the 399-day variation manifests itself with a 95% confidence in some of the solar wind parameters, we conclude that Jupiter may affect the solar wind.

(2) The amplitudes of the 399-day variations in the solar wind density, temperature, and speed are 6, 2.5, and 0.6%, respectively.

ACKNOWLEDGMENTS

This work was supported in part by INTAS (grant no. 03-51-5359), the Russian Foundation for Basic Research (project nos. 03-02-96026 and 03-05-65670), and the "Program for Support of Leading Scientific Schools of Russia" (project no. NSh-422.2003.2).

REFERENCES

1. *Astronomical Yearbook for 1965–2002* (Inst. Prikl. Astron., Nizhni Novgorod, 2001) [in Russian].
2. D. L. Chenette, T. F. Conlon, and G. A. Simpson, J. Geophys. Res. **79**, 3551 (1974).
3. J. H. Eraker, Astrophys. J. **257**, 862 (1982).
4. B. J. Freegarden, F. B. McDonald, J. H. Frainaz, *et al.*, J. Geophys. Res. **79**, 3615 (1974).
5. T. W. Hill, J. F. Carbary, and A. J. Dessler, Geophys. Res. Lett. **1**, 333 (1974).
6. B. Jamison amd R. Regal, *Solar–Terrestrial Relationships, Weather, and Climate,* Ed. by B. McCartman and T. Selig (Mir, Moscow, 1982), p. 204.
7. C. Lopate, in *Proceedings of the 22nd International Cosmic Ray Conference, Dublin, 1991*, Ed. by D. D'Sullivan, Vol. 2, p. 149.
8. F. B. McDonald and J. G. Treinor, *Jupiter III. Magnetosphere. Radiation Belts,* Ed. by T. Gerls (Mir, Moscow, 1979), p. 436.
9. *OMNI Database*, http://nssdc.nasa.gov/omniweb/ow.html (2003).
10. N. G. Skryabin, I. P. Bezrodnykh, I. Ya. Plotnikov, and O. P. Ivanov, Geomagn. Aéron. **41**, 450 (2001) [Geomagn. Aeron. **41**, 432 (2001)].
11. V. E. Timofeev, V. G. Grigoryev, I. Ya. Plotnikov, *et al.*, in *Proceedings of the 28th International Cosmic Ray Conference. Under the Auspices of the International Union of Pure and Applied Physics (IUPAP) Conference, Trukuba, Japan, 2003,* Ed. by T. Kawachi, V. Matsubara, and M. Sasaki (Tokyo Univ. Acad. Press, Tokyo, 2003), p. 4073.
12. J. A. Van Allen, B. A. Randell, D. N. Baker, *et al.*, Science **188**, 459 (1975).

Translated by G. Rudnitskiĭ

Astronomy Letters, Vol. 31, No. 12, 2005, pp. 836–843. Translated from Pis'ma v Astronomicheskiĭ Zhurnal, Vol. 31, No. 12, 2005, pp. 935–942.

Acceleration of Anomalous Cosmic Rays at the Heliospheric Termination Shock

E. G. Berezhko* and L. T. Ksenofontov

Institute of Cosmophysical Research and Aeronomy, Siberian Division, Russian Academy of Sciences, pr. Lenina 31, Yakutsk, 677891 Russia

Received May 23, 2005

Abstract—The acceleration of anomalous cosmic rays (ACRs) at the heliospheric termination shock and their influence on the shock structure and location are analyzed in terms of a self-consistent nonlinear kinetic model. The ACR spectrum, the structure of the heliospheric termination shock, and its location are shown to be very sensitive to the ACR acceleration efficiency, i.e., to the injection rate of the pick-up ions produced by the ionization of interstellar neutral atoms penetrating into the heliosphere. A relatively high injection rate of pick-up protons, when ~1% of the pick-up ions are drawn into the acceleration process, is required to reproduce the observed ACR proton spectrum. © *2005 Pleiades Publishing, Inc.*

Key words: *solar wind, heliosphere, cosmic rays.*

INTRODUCTION

Anomalous cosmic rays (ACRs), or, more precisely, the anomalous cosmic-ray component, whose existence was established in the early 1970s, got their name from the unusual shape of their energy spectrum in the energy range $\epsilon = 1-100$ MeV per nucleon, which differs radically from the spectrum of Galactic cosmic rays (see the review article by Fichtner (2001) and references therein). According to the now universally accepted viewpoint, ACRs result from the acceleration of ionized particles of the local interstellar medium at the heliospheric termination shock that bounds the supersonic solar-wind flow region. Penetrating into the Solar system, the neutral component of the interstellar medium, which consists mostly of hydrogen, helium, nitrogen, oxygen, and neon atoms, is ionized by ultraviolet solar radiation or via charge exchange with solar-wind ions. Subsequently, these pick-up ions drift into the heliospheric shock region through the solar wind and are accelerated to produce ACRs. For example, the identity between the measured chemical compositions of the neutral component of the local interstellar medium and ACRs argues for this scenario (Fichtner 2001). The diffuse acceleration at the heliospheric termination shock is considered to be the main ACR generation mechanism (Pesses *et al.* 1981). Since the energy content of ACRs is fairly high, these become an important dynamical factor that affects significantly the structure of the termination shock front (Jokipii 1990; Donohue and Zank 1993; Le Roux and Fichtner 1997). A detailed description of the ACR acceleration at the heliospheric termination shock must include the back reaction of pick-up ions and ACRs.

To describe the ACR acceleration, we use here a nonlinear kinetic theory of acceleration that was originally developed (Berezhko *et al.* 1996; Berezhko and Völk 1997, 2000) to describe the cosmic-ray acceleration in supernova remnants. The theory consistently allows for the shock modification by the accelerated-particle pressure and yields a self-consistent accelerated-particle spectrum. In a similar formulation, this problem was considered previously by Le Roux and Fichtner (1997). However, as we show below, our results differ significantly from those obtained by Le Roux and Fichtner (1997).

THE MODEL

The heliospheric configuration is formed through the slowdown of the solar wind as it interacts with the ambient interstellar medium. Allowance for the presence of distinctly different components (plasma, neutral atoms, cosmic rays) in this medium and the motion of the Solar system relative to the medium lead to a complex heliospheric structure elongated enormously along the motion of the Solar system (see, e.g., Fichtner 2001; Izmodenov 2000; Baranov 2003; Alexashov *et al.* 2004). The termination shock in the solar wind is also expected to be asymmetric, although the departures of its shape from a sphere are not so significant as those for the outer heliospheric regions (Alexashov *et al.* 2004). Since

*E-mail: berezhko@ikfia.ysn.ru

the particle acceleration at the termination shock is weakly sensitive to the structure of the outermost heliospheric regions, we use here the spherically symmetric approximation to describe the ACR dynamics, as was done in a number of similar papers (Le Roux and Fichtner 1997).

For the sake of simplicity, we restrict our analysis to hydrogen, which is the predominant type of atoms penetrating from the interstellar medium, and, accordingly, to protons in the ACR composition. Heavier ions in the ACR composition, such as helium and oxygen ions, are of indubitable interest for study. However, to a first approximation, the dynamical effect of these heavier ions on the termination shock structure can be disregarded. In addition, the considerable deviation of the parameters of the solar wind from those of a spherically symmetric one and the drift effects plays a significant role in shaping the spatial ACR distribution in the heliosphere (Florinski *et al.* 2004). Therefore, it is unlikely that spherically symmetric models similar to our model can purport to explain in detail the ACR spectra, particularly those observed far from the termination shock. For this reason, we restrict our analysis here to protons in the ACR composition and focus our attention on studying the shock modification by ACR particles and its dependence on the injection rate of pick-up ions into the acceleration process.

The ACR distribution function $f(r,p,t)$ satisfies the diffusive transport equation (Krymskiĭ 1964)

$$\frac{\partial f}{\partial t} = \frac{1}{r^2}\frac{\partial}{\partial r}\left(r^2\kappa\frac{\partial f}{\partial r}\right) - w\frac{\partial f}{\partial r} + \frac{1}{r^2}\frac{\partial}{\partial r}(r^2 w)\frac{p}{3}\frac{\partial f}{\partial p} + Q. \quad (1)$$

Here, r, p, and t are the heliocentric distance, the particle momentum, and the time, respectively; w is the solar-wind velocity; κ is the radial diffusion coefficient, which we take in the same form as that in Le Roux and Fichtner (1997):

$$\kappa = \kappa(r,p,t) = 6\times 10^{20}(p/mc)(v/c)(50\ \mu\mathrm{G}/B)\ \mathrm{cm}^2\ \mathrm{s}^{-1}, \quad (2)$$

where $B = \sqrt{B_\parallel^2 + B_\perp^2}$ is the interplanetary magnetic field strength; $B_\parallel = B\cos\Psi$ and $B_\perp = B\sin\Psi$ are the radial and tangential magnetic field components; $\Psi = \arctan(\Omega r/w)$ is the angle between the field line and the radial direction; and Ω is the angular velocity of the Sun.

The source

$$Q = \frac{u_1 N_{\mathrm{inj}}}{4\pi p_{\mathrm{inj}}^3}\delta(p-p_{\mathrm{inj}})\delta(r-R_s) \quad (3)$$

provides the injection $N_{\mathrm{inj}} = \eta N_1^{pu}$ of pick-up ions at the shock front from each unit volume that crosses the shock front. Here, $u = w - V_s$, $V_s = dR_s/dt$ is the shock velocity; the subscripts 1 and 2 correspond to the points $R_s - 0$ and $R_s + 0$ immediately upstream and downstream of the shock front, respectively. The dimensionless parameter η specifies the fraction of the total number of pick-up ions per unit volume upstream of the shock front N_1^{pu} that are drawn into the acceleration process. Here, the momentum of the injected ions is assumed to be $p_{\mathrm{inj}} = mu_1$.

The status of the current theory of a collisionless shock is such that the injection rate, i.e., the fraction of the ions of the medium drawn into the acceleration process, cannot be predicted reliably. Therefore, as in other similar cases (Berezhko *et al.* 1996; Berezhko and Völk 2000), η is a free parameter, and one of the questions explored below is the sensitivity of the shock structure and the ACR spectrum to η.

When pick-up ions are produced, the energy of their motion relative to the solar-wind plasma, $\sim$1 keV, is transformed into their thermal energy. Therefore, the thermal energy of the pick-up ions is considerably higher than that of the solar-wind protons. Since the hypothetical injection mechanism separates the particles by their energy or rigidity, thereby preventing the acceleration of particles with energies below a certain limit, we, as in other similar papers, restrict our analysis to the acceleration of only a certain fraction η of the pick-up ions and ignore the possibility of solar-wind proton acceleration.

Since the shock is the only ACR source in the problem under consideration and since the ACR diffusion coefficient tends to zero as the heliocentric distance decreases, ($\kappa(r,p) \to 0$ for $r \to 0$), the following boundary conditions should be taken for the ACR distribution function:

$$f(r,p,t) = 0 \text{ at } r = 0 \text{ and } r = \infty. \quad (4)$$

The distribution of the solar-wind parameters, density ρ, velocity w, and pressure P_{g}, can be determined from the system of gasdynamic equations

$$\frac{\partial \rho}{\partial t} + \frac{1}{r^2}\frac{\partial}{\partial r}(r^2\rho w) = Q_\rho, \quad (5)$$

$$\rho\frac{\partial w}{\partial t} + \rho w\frac{\partial w}{\partial r} + \frac{\partial}{\partial r}(P_{\mathrm{g}} + P_{\mathrm{c}}) = Q_p, \quad (6)$$

$$\frac{\partial P_{\mathrm{g}}}{\partial t} + w\frac{\partial P_{\mathrm{g}}}{\partial r} + \frac{\gamma}{r^2}\frac{\partial}{\partial r}(r^2 w)P_{\mathrm{g}} = Q_P, \quad (7)$$

where γ is the adiabatic index of the medium, $P_{\mathrm{c}} = \frac{4\pi}{3}\int\limits_{p_{\mathrm{inj}}}^{\infty} dpp^3 vf$ is the ACR pressure, and the right-hand sides (sources) describe the changes in the density,

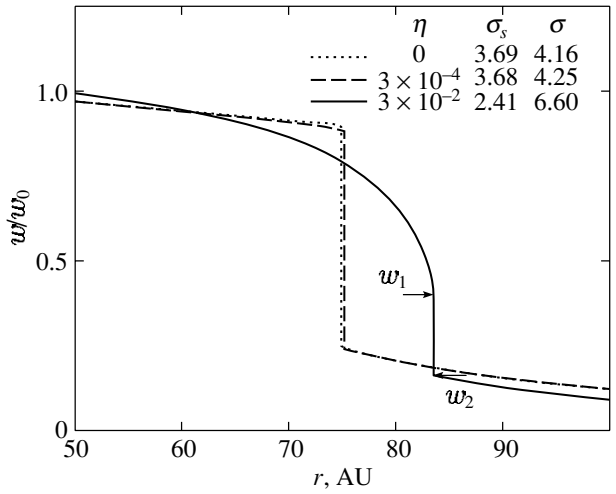

Fig. 1. Radial profiles of the solar-wind velocity w for three different injection rates: $\eta = 0$, 3×10^{-4}, and 3×10^{-2}.

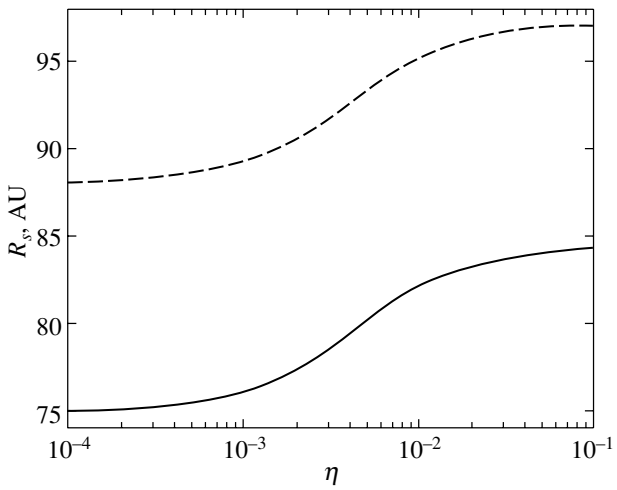

Fig. 2. Radius of the heliospheric termination shock R_s versus injection rate of pick-up protons η for two different solar-wind densities: $n_0 = 5\ \mathrm{cm}^{-3}$ (solid curve) and $n_0 = 7\ \mathrm{cm}^{-3}$ (dashed curve).

momentum, and pressure of the medium due to the photoionization and charge exchange of interstellar hydrogen atoms. As we show below, the ACR spectrum is steeply cut off at subrelativistic energies. Therefore, we use the adiabatic index $\gamma = 5/3$ in our calculations. Note also that the parameters of the medium (gas) ρ, w, and P_g also include the contribution from the pick-up ions. The expressions for the sources in Eqs. (5)–(7) were taken in complete agreement with the paper by Le Roux and Fichtner (1997):

$$Q_\rho = mN_\mathrm{H}\nu_\mathrm{ph}, \tag{8}$$

$$Q_p = -mw\nu_{ce}N_\mathrm{H} - wQ_\rho, \tag{9}$$

$$Q_P = (\gamma - 1)\left[(w^2/2)Q_\rho - Q_E + mw^2\nu_{ce}N_\mathrm{H}\right], \tag{10}$$

where m is the proton mass, $\nu_\mathrm{ph} = 9 \times 10^{-8} \times (1\ \mathrm{AU}/r)^2\ \mathrm{s}^{-1}$ is the photoionization rate of hydrogen atoms, $N_\mathrm{H} = 0.077 \exp(-3.74\ \mathrm{AU}/r)\ \mathrm{cm}^{-3}$ is the number density of interstellar hydrogen in the heliosphere, $\nu_{ce} = 10^{-15}[w/(1\ \mathrm{cm\ s}^{-1})][n/(1\ \mathrm{cm}^{-3})] \times \{7.5 - 2.1\log[w/(1\ \mathrm{km\ s}^{-1})]\}\ \mathrm{s}^{-1}$ at $r < R_s$ and $\nu_{ce} = 1.23 \times 10^{-15}[v_\mathrm{T}/(1\ \mathrm{cm\ s}^{-1})][n/(1\ \mathrm{cm}^{-3})] \times \{7.5 - 2.1 \times \log[1.23v_\mathrm{T}/(1\ \mathrm{km\ s}^{-1})]\}\ \mathrm{s}^{-1}$ at $r > R_s$ is the charge exchange rate for hydrogen atoms as they collide with solar-wind protons, v_T is the mean thermal velocity, $n = \rho/m$ is the solar-wind proton number density, and $Q_E = mw^2\nu_{ce}N_\mathrm{H}/2$ at $r < R_s$ and $Q_E = mv_\mathrm{T}^2\nu_{ce}N_\mathrm{H}/2$ at $r > R_s$ is the energy source. As in the paper by Le Roux and Fichtner (1997), we took $Q_i = 0$ at $r > r_\mathrm{max} = 120$ AU.

The pick-up ion number density is given by the equation

$$\frac{\partial N^{pu}}{\partial t} + \frac{1}{r^2}\frac{\partial}{\partial r}(r^2 w N^{pu}) = (\nu_\mathrm{ph} + \nu_{ce})N_\mathrm{H}. \tag{11}$$

The properties of the solar wind can be specified in the form of boundary conditions at the inner boundary r_0 if the size r_0 is chosen to be small enough, $r_0 \ll R_s$, for the ACR effect on the medium at $r \le r_0$ to be negligible. As in the paper by Le Roux and Fichtner (1997), we took

$$w_0 = 400\ \mathrm{km\ s}^{-1}, \quad \rho_0 = 5m\ \mathrm{cm}^{-3}, \quad T_0 = 10^5\ \mathrm{K} \tag{12}$$

at $r = r_0 = 1$ AU.

The conditions at the outer boundary $r = \infty$ specify the shock location. We used

$$w = 0, \quad P = P_\mathrm{ISM} \tag{13}$$

at $r = \infty$, where $P_\mathrm{ISM} = 1\ \mathrm{eV\ cm}^{-3}$ is the pressure of the interstellar medium. These conditions slightly differ from those used by Le Roux and Fichtner (1997), who solved the problem in the region $r < r_\mathrm{max}$ and took a free boundary condition at $r = r_\mathrm{max}$. However, since the region $r > R_s$ is nearly isobaric, this difference is not very significant. In addition, in contrast to Le Roux and Fichtner (1997), we disregard here the influence of Galactic cosmic rays on the structure of the heliosphere. This approach is justified by the results of Le Roux and Fichtner (1997): the influence of Galactic cosmic rays on the shock location and structure is much weaker than that of pick-up ions and ACRs.

The interaction of a supersonic solar wind with the ambient interstellar medium is accompanied by the

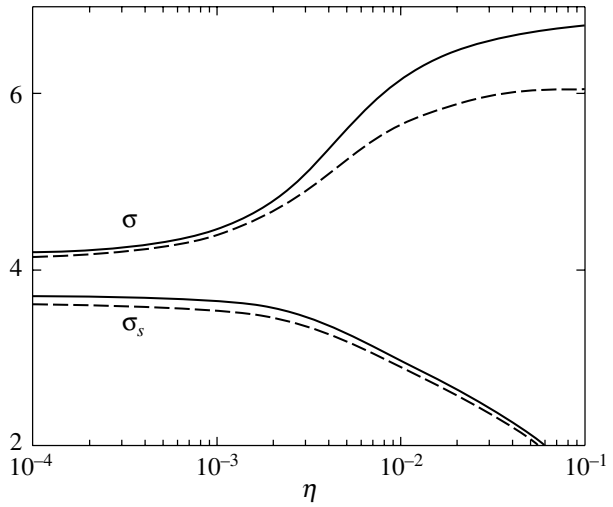

Fig. 3. Total compression ratio of the heliospheric termination shock σ and compression ratio at the shock transition σ_s versus injection rate of pick-up protons η for the same two cases as those in Fig. 2.

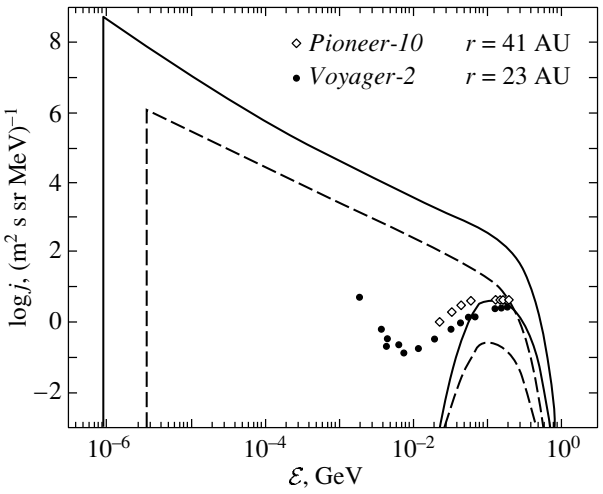

Fig. 4. Differential ACR intensity versus kinetic energy for high ($\eta = 3 \times 10^{-2}$, solid curves) and low ($\eta = 3 \times 10^{-4}$, dashed curves) injection rates. The thick and thin lines correspond to heliocentric distances of $r = R_s$ and $r = 40$ AU, respectively. The ACR proton flux measurements from *Pioneer 10* at $r = 41$ AU and *Voyager 2* at $r = 23$ AU (McDonald *et al.* 1995) are indicated by the diamonds and dots, respectively.

formation of a shock. Under the steady-state conditions that we considered here, this shock is stationary. Since the region $r > R_s$ downstream of the shock front is nearly isobaric, the location of the shock front is specified by the condition $\rho w^2 \simeq P_{\rm lSM}$.

The shock front is treated as a discontinuity at which the gas parameters change abruptly:

$$u_2 = u_1/\sigma_s, \quad \rho_2 = \sigma_s \rho_1, \tag{14}$$

where

$$\sigma_s = 4/(1 + 3/M_1^2) \tag{15}$$

is the compression ratio at the shock front, $M = u/c_s$ is the Mach number, and $c_s = \sqrt{\gamma P/\rho}$ is the speed of sound.

In the case under consideration, the solar wind also slows down significantly in the region $r < R_s$ upstream of the shock front through its loading with pick-up ions and under the ACR pressure. The forming extended slowdown segment, the preshock region, in which the solar-wind velocity changes from u_0 to u_1, can also be considered as part of the shock transition. Therefore, in addition to the compression ratio at the shock front σ_s, we will also use $\sigma = u_0/u_2$, which may be arbitrarily called the total compression ratio. Note that $V_s = 0$ and $w_i = u_i$ in the steady state. Although we present below the results of our calculations for the steady state, in fact, we solved a nonstationary problem with initial conditions ($t = 0$): $f(r, p) = 0$, $w(r < R_s) = w_0$, $\sigma = \sigma_0$, $w(r > R_s) = w_2(R_s/r)^2$, and $R_s = r_0\sqrt{3\rho_0 w_0^2/(4P_{\rm lSM})}$.

Since the adopted initial shock location is only an approximation of the exact location and due to the influence of the accelerated ACRs, the shock at $t > 0$ acquires a velocity V_s and is gradually displaced to the true equilibrium location, upon reaching which the shock velocity again tends to zero ($|V_s| \to 0$ for $t \to \infty$). Our method of solving the problem allows it to be also solved in a nonstationary formulation that includes the change in solar-wind parameters in the solar cycle, which we plan to do in our subsequent papers.

RESULTS AND DISCUSSION

The results of our calculations are presented in Figs. 1–4. As can be seen from these figures, pick-up ions and ACRs modify the termination shock in the solar wind. These factors produce an extended preshock region at $r < R_s$ and change the shock compression ratio and its location (radius R_s).

To analyze our numerical solutions of the problem and since the solutions differ significantly from those obtained by Le Roux and Fichtner (1997), let us turn to their qualitative analysis. For this purpose, we integrate Eqs. (5)–(7) over $r^2 dr$ from r_0 to $R_s + 0$ for the stationary case to give

$$\rho_2 w_2 = \rho_R w_0 + F_\rho, \tag{16}$$

$$\rho_2 w_2^2 = \rho_R w_0^2 + \rho_R P_0/\rho_0 - P_2 - F_p, \tag{17}$$

$$w_2\left(\frac{\rho_2 w_2^2}{2}+\frac{\gamma}{\gamma-1}P_2\right) \quad (18)$$
$$=\left(\frac{\rho_R w_0^2}{2}+\frac{\gamma}{\gamma-1}\frac{P_0}{\rho_0}\rho_R\right)w_0-F_E,$$

where

$$F_\rho=(1/R_s^2)\int\limits_{r_0}^{R_s}drr^2Q_\rho, \quad (19)$$

$$F_p=(1/R_s^2)\int\limits_{r_0}^{R_s}drr^2Q_p-(2/R_s^2)\int\limits_{r_0}^{R_s}drr(P_\mathrm{g}+P_\mathrm{c}), \quad (20)$$

$$F_E=(1/R_s^2)\int\limits_{r_0}^{R_s}drr^2Q_E+F_D \quad (21)$$

are, respectively, the matter, momentum, and energy flux densities attributable to the pick-up ions and ACRs; $F_\mathrm{D}=-4\pi\int dp\,p^2\epsilon\kappa(\partial f/\partial r)$ is the ACR diffusive energy flux density, ϵ is the kinetic energy of the ACR particles and $\rho_R=\rho_0(r_0/R_s)^2$.

Relations (16)–(18) allow us to determine the total compression ratio

$$\sigma=\left(\frac{1+F'_\rho}{1+1/(\gamma M_0^2)-F'_p}\right)\frac{\gamma+1}{\gamma-x}, \quad (22)$$

where

$$x=\left\{1-(\gamma^2-1)\left[2\left(\frac{1}{\gamma M_0^2}-F'_p\right)+\left(\frac{1}{\gamma M_0^2}-F'_p\right)^2-F'_E-\frac{2}{(\gamma-1)M_0^2}-F'_\rho\left(1+\frac{2}{(\gamma-1)M_0^2}-F'_E\right)\right]\times\left(1+\frac{1}{\gamma M_0^2}-F'_p\right)^{-2}\right\}^{1/2},$$

$F'_\rho=F_\rho/(\rho_R w_0)$, $F'_p=F_p/(\rho_R w_0^2)$, $F'_E=F_E/(\rho_R w_0^3/2)$. In the absence of pick-up ions and ACRs ($P_\mathrm{c}=0$), Eq. (22) with the term $F_p=-(2/R_s^2)\int\limits_{r_0}^{\infty}drrP_\mathrm{g}$, which ensures adiabatic cooling of the solar wind as it propagates from $r=r_0$ to $r=R_s$, yields

$$\sigma_0=4/(1+3/M_1^2), \quad (23)$$

where $M_1=M_0(\rho_1/\rho_0)^{4/3}=M_0(R_s/r_0)^{2/3}$ is the Mach number of the shock. Since $M_0\simeq 10$ and $M_1\gg 10$, the compression ratio in this case is close to $\sigma_0=4$.

To simplify our analysis of the influence of ACRs and pick-up ions on the shock, let us consider the case of small perturbations where $F'_i\ll 1$. In this case, Eq. (22) yields

$$\sigma=\sigma_0\left(1+\frac{4}{3}F'_E-\frac{5}{3}F'_p-\frac{1}{3}F'_\rho\right). \quad (24)$$

Setting $w=w_0$ in the expressions for Q_i, we obtain

$$\sigma=\sigma_0\left[1+\frac{4}{3}F'_D-\frac{1}{3R_s^2\rho_R w_0^2}\times\int\limits_{r_0}^{R_s}drr(rQ_p+rw_0Q_\rho+P_\mathrm{g}+P_\mathrm{c})\right]. \quad (25)$$

Let us consider the case of $P_\mathrm{c}=0$. To estimate $\int\limits_{r_0}^{R_s}drrP_\mathrm{g}=LRP_{\mathrm{g}1}$ (here, L is the scale length of the preshock region), we integrate Eq. (7) over r^2dr from r_0 to R_s-0 to give

$$LRP_{\mathrm{g}1}=\frac{L}{3R}\left(w_0\int\limits_{r_0}^{R_s}drr^2Q_\rho+\int\limits_{r_0}^{R_s}drr^2Q_p\right). \quad (26)$$

Using this relation, we obtain

$$\sigma=\sigma_0\left[1+\frac{\left(\frac{10}{3}\frac{L}{R}-1\right)}{3R^2\rho_R w_0}\int\limits_{r_0}^{R_s}drr^2Q_\rho+\frac{\left(\frac{10}{3}\frac{L}{R}-1\right)}{3R^2\rho_R w_0}\int\limits_{r_0}^{R_s}drr^2Q_p\right]. \quad (27)$$

As can be seen from this equation, if the scale length of the preshock region $L>0.3R_s$, then the shock compression ratio due to the influence of pick-up ions increases. This condition means the following: the larger the value of L, the more significant the cooling of the pick-up ions produced by ionization and charge exchange during their transport from the formation site to the shock and, hence, the higher the compression ratio of the shock front σ_s.

In the absence of pick-up ions, the shock radius is $R_s\simeq 80$ AU. According to our calculations, $L\simeq 35$ AU, i.e., $L\simeq 0.44R_s$; therefore, $\sigma>\sigma_0\simeq 4$ (see Fig. 1).

As can be seen from Eqs. (17) and (18), the increase in compression ratio σ is accompanied by an

increase in the gas pressure downstream of the shock front,

$$P_2 \simeq \rho_1 u_1^2 (1 - 1/\sigma). \quad (28)$$

To maintain isobaricity, $P \simeq P_{\rm ISM}$, at $r > R_s$, the shock should have moved into the region of large R_s, since, as follows from Eq. (28), $R_s \simeq r_0\sqrt{P_{\rm ISM}/[\rho_0 w_0^2(1-1/\sigma)]}$. However, as we see from Fig. 2, when the influence of pick-up ions is taken into account and in the absence of ACRs (more precisely, at low injection rates, $\eta \lesssim 10^{-4}$) the shock radius $R_s \simeq 75$ AU is smaller than that in the absence of ions. This is because $Q_P < 0$ downstream of the shock front; i.e., the formation of pick-up ions here causes the gas pressure to decrease. As follows from our calculations, this effect is stronger than the effect of the increase in compression ratio σ. Therefore, maintaining isobaricity requires a displacement of the shock toward the smaller R_s.

As we see from Figs. 1–3, the effect of ACRs on the shock structure and location increases with injection rate. As can be seen from Eq. (22), the diffusive ACR flux downstream of the shock front $F_D > 0$ and the adiabatic ACR deceleration at $r < R_s$ with which the term $\int_{r_0}^{R_s} drrP_{\rm c}$ is associated cause the compression ratio σ and the shock radius R_s to increase. Both these effects lead to an outflow of part of the energy from the shock transition region, much as is the case with a radiative shock. As we see from Figs. 2 and 3, the parameters σ and R_s increase particularly significantly with increasing injection rate in the range $\eta = 10^{-3}$–10^{-1}.

The rise in total compression ratio σ is attributable solely to the solar-wind slowdown in the preshock region, i.e., to the rise in the compression ratio $\sigma_p = u_0/u_1$ of the preshock region. In this case, as we see from Fig. 3, the compression ratio at the shock front σ_s decreases with increasing η. The latter is attributable to a decrease in the Mach number $M_1 = u_1/c_{s1}$ due to a decrease in the velocity u_1 and an increase in the speed of sound c_{s1} through heating of the solar-wind matter in the preshock region. Note that our results disagree significantly with those obtained by Le Roux and Fichtner (1997). Thus, for example, at $\eta = 0$, 3×10^{-4} and 0.9, we have $\sigma = 4.16$, $R_s = 75$ AU; $\sigma = 4.25$, $R_s = 75.3$ AU; and $\sigma = 6.7$, $R_s = 89$ AU, respectively, while Le Roux and Fichtner (1997) obtained $\sigma = 4.01$, $R_s = 73.7$ AU; $\sigma = 4.24$, $R_s = 74.3$ AU; and $\sigma = 2.73$, $R_s = 73.8$ AU, respectively. As we see, the difference is particularly large at high injection rates. Our calculations (see Fig. 3) show a monotonic increase in compression ratio σ with injection rate η, which is similar to the situation with shocks from supernova explosions (Berezhko *et al.* 1996), while, according to Le Roux and Fichtner (1997), $\sigma(\eta)$ is a nonmonotonic function.

The compression ratio $\sigma = 2.73$ that, according to Le Roux and Fichtner (1997), corresponds to the injection rate $\eta = 0.9$ is considerably lower than $\sigma \simeq 4$ that corresponds to $\eta = 0$. This is in conflict with Eq. (22), which suggests that the compression ratio σ in the presence of ACRs is always higher than that in their absence.

Note also that the significant influence of ACRs on the shock radius R_s that we revealed (see Fig. 2) is in qualitative agreement with the results by Alexashov *et al.* (2004), who described the ACR dynamics in terms of a simplified hydrodynamic approach, and with the results by Florinski *et al.* (2004), who solved a similar problem by taking into account the drift effects and the nonspherical distribution of solar-wind parameters. Unfortunately, it is difficult to make a more detailed comparison with the results by Florinski *et al.* (2004), since these authors did not analyze the effect of the injection rate on the shock modification and the ACR spectrum and did not give the adopted injection rate for the specific solutions presented in their paper. It can only be noted that the modification effects determined by Florinski *et al.* (2004), the decrease in the compression ratio of the termination shock front $\Delta\sigma_s = 0.1$–0.2 and the increase in the shock radius by $\Delta R_s \sim 1$ AU, correspond to our injection parameter $\eta \simeq 3 \times 10^{-3}$ (see Figs. 2 and 3).

The ACR spectra exhibit the same significant difference. According to Le Roux and Fichtner (1997), the ACR spectra corresponding to significantly different injection rates, $\eta = 3 \times 10^{-4}$ and $\eta = 0.9$, differ only slightly at energies $\epsilon \gtrsim 1$ MeV. Our calculated differential (in kinetic energy) ACR intensities $j = p^2 f$ as functions of the kinetic energy $\epsilon = p^2/(2m)$ (see Fig. 4) change significantly in both amplitude and shape with injection rate. At a low injection rate, $\eta = 3 \times 10^{-4}$, the shock is modified weakly; therefore, the ACR spectrum is close to a purely power-law spectrum with an index of $q = 3\sigma_s/(\sigma_s - 1) \simeq 4$, which yields $j \propto \epsilon^{-(q-2)/2} \simeq \epsilon^{-1}$ in the entire energy range from the injection energy $\epsilon_{\rm inj} = p_{\rm inj}^2/(2m) \sim 1$ keV to the maximum energy $\epsilon_{\rm max} \simeq 200$ MeV. In this case, as we see from Fig. 4, the intensity of ACRs with energies 10–300 MeV expected at a distance of $r = 23$ AU is much lower than the experimentally observed one.

At a much higher injection rate, $\eta = 3 \times 10^{-2}$, the ACR spectrum is no longer a purely power-law spectrum due to significant shock modification. At low energies, 1 keV $< \epsilon <$ 100 keV, for a power-law fit $f \propto p^{-q}$, the index $q = q_s = 3\sigma_s/(\sigma_s - 1) \simeq 5.1$

is considerably higher than its canonical value of 4; accordingly, the energy dependence of the differential flux is $j \propto \epsilon^{-1.6}$. At higher energies, 20 MeV $< \epsilon <$ 200 MeV, the ACR spectrum is considerably harder, $j \propto \epsilon^{-1}$. As we see from Fig. 4, the ACR intensity at energies $\epsilon \sim 100$ MeV expected at a distance of $r =$ 40 AU corresponds to the experimentally observed one (McDonald *et al.* 1995).

As we see from Fig. 4, the theory in its present simplified form by no means ideally reproduces the ACR spectra observed in the heliosphere. We can only say that our calculations confirm that the observed ACR fluxes with energies $\epsilon = 10$–100 MeV can be produced in principle through the diffuse acceleration of pick-up ions at the termination shock in the solar wind.

Since analysis of the ACR flux measurements and anisotropy suggested that the *Voyager-1* spacecraft has repeatedly crossed the termination shock since August 1, 2002 (Krimigis *et al.* 2003), comparing the shock radius R_s predicted by our model with its measured value is of considerable interest. The measurements show that the first crossing of the termination shock corresponds to $R_s \simeq 85$ AU and its second crossing recorded half a year later corresponds to $R_s \simeq 87$ AU. According to Fig. 3, these values slightly exceed the shock radius R_s that corresponds to extremely high injection rates η. Note, however, that the solar-wind proton number density $n_0 = n(r = 1 \text{ AU}) = 5$ cm^{-3} that we adopted to make a detailed comparison with the results by Le Roux and Fichtner (1997) is clearly an underestimate. According to numerous measurements, $n_0 =$ 7 cm^{-3} should be considered a typical number density (Toptygin 1983). Our calculations for $n_0 = 7$ cm^{-3} at fixed remaining parameters are also presented in Figs. 2 and 3. As we see from Fig. 3, the shock radius $R_s(\eta)$ increased compared to the previous case of $n_0 = 5$ cm^{-3} by 13 AU. Taking $\eta = 10^{-2}$ as a plausible injection rate, we may conclude that the shock radius is expected to be within the range $R_s =$ 82–96 AU corresponding to the solar-wind density $n_0 = 5$–7 cm^{-3}, in agreement with the measurements (Krimigis *et al.* 2003). The actual R_s range must be even wider due to the variations in both the solar-wind density $n_0 = 5$–10 cm^{-3} and the solar-wind velocity w.

Since the ACR spectra at the termination shock front, $r = R_s$, and at smaller distances, $r < R_s$, for $n_0 = 7$ cm^{-3} differ only slightly from those for $n_0 =$ 5 cm^{-3}, we do not give them here.

CONCLUSIONS

Our calculations show that the termination shock in the solar wind is affected significantly by the pick-up ions that are produced by the photoionization and charge exchange of interstellar atoms: a smooth extended preshock region is formed within the shock transition, and the termination shock front (discontinuity) is displaced inward by $\Delta R_s \simeq 5$ AU.

The ACR spectrum that is formed via the acceleration of a certain fraction η of the pick-up ions at the termination shock and the degree of shock modification due to their back reaction depend significantly on the injection rate η, i.e., on the fraction of the ions that undergo acceleration. The degree of shock modification increases with injection rate η: the total compression ratio σ increases, and the compression ratio at the termination shock front σ_s decreases; the shock radius R_s increases as a result of the increase in σ that is accompanied by a rise in the thermal pressure downstream of the shock front. Quantitatively, the increase in the shock radius can reach $\Delta R_s \simeq$ 10 AU if the injection rate $\eta \gtrsim 10^{-2}$.

The expected shock radius that corresponds to typical solar-wind parameters and injection rate of pick-up ions into acceleration $\eta = 10^{-2}$ is $R_s \simeq$ 95 AU. The radius R_s is subject to significant time variations within $\Delta R_s \simeq 10$ AU due to the variations in both the solar-wind parameters and the injection rate η.

The self-consistent ACR spectrum also depends significantly on the injection rate. At low injection rates, $\eta \lesssim 10^{-3}$, the ACRs have a purely power-law spectrum, $f \propto p^{-4}$. At considerably higher injection rates, $\eta \gg 10^{-3}$, the ACR spectrum is convex in shape: softer at low energies $\epsilon < 100$ keV and harder at the highest energies $\epsilon > 10$ MeV. Comparison with experimental data shows that a fairly high injection rate, $\eta \geq 10^{-2}$, is required to provide the ACR fluxes observed at distances of $r = 10$–40 AU.

At low injection rates, $\eta \ll 10^{-3}$, our results agree with those obtained by Le Roux and Fichtner (1997). At the same time, the results strongly disagree at high injection rates, $\eta \gg 10^{-3}$. Our qualitative analysis indicates that, contrary to the results by Le Roux and Fichtner (1997), the compression ratio σ and the shock radius R_s are monotonically increasing functions of the injection rate η, as confirmed by our calculations.

ACKNOWLEDGMENTS

This work was supported by the Russian Foundation for Basic Research (project no. 03-02-16524), INTAS (grant no. 2001-0270), and VNSh (project no. 422.2003.22).

REFERENCES

1. D. B. Alexashov, S. V. Chalov, A. V. Myasnikov, *et al.*, Astron. Astrophys. **420**, 729 (2004).
2. V. B. Baranov, *Solar Wind Ten*, Ed. by M. Velli, R. Bruno, and F. Malama (Am. Inst. Phys., New York, 2003), p. 21.
3. E. G. Berezhko, V. K. Elshin, and L. T. Ksenofontov, Zh. Éksp. Teor. Fiz. **109**, 3 (1996) [JETP **82**, 1 (1996)].
4. E. G. Berezhko and H. J. Völk, Astropart. Phys. **7**, 183 (1997).
5. E. G. Berezhko and H. J. Völk, Astron. Astrophys. **357**, 283 (2000).
6. D. J. Donohue and G. P. Zank, J. Geophys. Res. **98**, 19 005 (1993).
7. H. Fichtner, Space Sci. Rev. **95**, 639 (2001).
8. V. Florinski, G. P. Zank, J. R. Jokipi, *et al.*, Astrophys. J. **610**, 1169 (2004).
9. V. V. Izmodenov, Astrophys. Space Sci. **274**, 55 (2000).
10. J. R. Jokipii, *Physics of the Outer Heliosphere. Proceedings of the 1st COSPAR Colloquium, Warsaw, Poland, 1989*, Ed. by S. Grzedzielski and D. E. Page (Pergamon, 1990), p. 169.
11. S. M. Krimigis, R. B. Decker, M. E. Hill, *et al.*, Nature **426**, 45 (2003).
12. G. F. Krymskiĭ, Geomagn. Aéron. **4**, 977 (1964).
13. J. A. Le Roux and H. Fichtner, Astrophys. J. **477**, L115 (1997).
14. F. B. McDonald, A. Lukasiak, and W. R. Webber, Astrophys. J. **446**, L101 (1995).
15. M. E. Pesses, D. Eichler, and J. R. Jokippi, Astrophys. J. **246**, L85 (1981).
16. I. N. Toptygin, *Cosmic Rays in Interplanetary Magnetic Fields* (Nauka, Moscow, 1983; Reidel, Dordrecht, 1985).

Translated by V. Astakhov

Astronomy Letters, Vol. 31, No. 12, 2005, pp. 844–852. Translated from Pis'ma v Astronomicheskiĭ Zhurnal, Vol. 31, No. 12, 2005, pp. 943–952.

On the Stability of Particular Solutions of the Singly Averaged Hill Problem

M. A. Vashkov'yak* and N. M. Teslenko**

Keldysh Institute of Applied Mathematics, Russian Academy of Sciences, Miusskaya pl. 4, Moscow, 125047 Russia

Received June 3, 2005

Abstract—We consider the particular solutions of the evolutionary system of equations in elements that correspond to planar and spatial circular orbits of the singly averaged Hill problem. We analyze the stability of planar and spatial circular orbits to inclination and eccentricity, respectively. We construct the instability regions of both particular solutions in the plane of parameters of the problem. © *2005 Pleiades Publishing, Inc.*

Key words: *celestial mechanics, averaged Hill problem, orbital stability.*

INTRODUCTION. FORMULATION OF THE PROBLEM

This work is a continuation of our analysis of particular solutions of the averaged restricted circular problem of three mass points (Moiseev 1945a, 1945b) and its simplified version, the singly averaged Hill problem. Since this problem in its general (three-dimensional) formulation is nonintegrable, it is natural first to study its particular solutions, and our goal is to analyze their stability. In what follows, we use the formulation of the problem of the evolution of a satellite orbit given by Vashkov'yak (2005) and the standard notation for the Keplerian elements n, a, e, i, ω, Ω, and the gravitational constant μ. For the sake of consistency, we repeat the basic equations and the explanations of some of the notations from the above paper.

The evolutionary equations of the Hill problem averaged over the mean anomaly of a satellite are

$$\frac{da}{d\tau} = 0,$$

$$\frac{de}{d\tau} = 10e\sqrt{1-e^2}[\sin^2 i \sin 2\omega + (2-\sin^2 i)\sin 2\omega\cos 2\tilde{\Omega} + 2\cos i\cos 2\omega\sin 2\tilde{\Omega}],$$

$$\frac{di}{d\tau} = -\frac{2\sin i}{\sqrt{1-e^2}}\{5e^2\cos i\sin 2\omega(1-\cos 2\tilde{\Omega}) - [2+e^2(3+5\cos 2\omega)]\sin 2\tilde{\Omega}\},$$

$$\frac{d\omega}{d\tau} = \frac{2}{\sqrt{1-e^2}}\{4+e^2-5\sin^2 i + 5(\sin^2 i - e^2)\cos 2\omega + 5(e^2-2)\cos i\sin 2\omega\sin 2\tilde{\Omega} + [5(2-e^2-\sin^2 i)\cos 2\omega - 2 - 3e^2 + 5\sin^2 i]\cos 2\tilde{\Omega}\},$$

$$\frac{d\tilde{\Omega}}{d\tau} = -\nu - \frac{2}{\sqrt{1-e^2}}\{[2+e^2(3-5\cos 2\omega)]\cos i(1-\cos 2\tilde{\Omega}) - 5e^2\sin 2\omega\sin 2\tilde{\Omega}\}. \quad (1)$$

Here, in addition to the commonly used Keplerian elements, we introduce the variable $\tilde{\Omega} = \Omega - \lambda'$, the difference between the longitude of the ascending node of the satellite orbit and the mean longitude of the perturbing body. The "normalized" time $\tau = \beta n(t-t_0)$, where $\beta = \dfrac{3\mu' a^3}{16\mu a'^3}$ and the dimensionless positive parameter of the problem ν in the last equation of (1) is defined by the formula $\nu = \dfrac{n'}{n\beta}$ (the elements n', a', and the gravitational constant μ' refer to the perturbing body), is used as an independent variable. This parameter can be expressed in terms of the ratios n/n' and μ/μ' as $\nu = \dfrac{16n}{3n'}(1+\dfrac{\mu}{\mu'})$, so physically (for fixed μ and μ') it means a quantity proportional to the ratio of the mean motions of the satellite and the planet.

Equations (1) admit of the first two integrals (Moiseev 1945b):

$$a = \text{const},$$

$$V + \nu\sqrt{1-e^2}\cos i = \text{const},$$

*E-mail: vashkov@keldysh.ru
**E-mail: teslen@keldysh.ru

where

$$V = 2(e^2 - \sin^2 i) + e^2 \sin^2 i(5\cos 2\omega - 3) - 10e^2 \cos i \sin 2\omega \sin 2\tilde{\Omega} + [2\sin^2 i + 10e^2 \cos 2\omega + e^2 \sin^2 i(3 - 5\cos 2\omega)] \cos 2\tilde{\Omega},$$

and the particular solutions corresponding to planar ($\sin i = 0$) and spatial circular ($e = 0$) orbits.

PARTICULAR SOLUTIONS OF THE EVOLUTIONARY SYSTEM

(1) At $\sin i = 0$, system (1) can be transformed by introducing more convenient variables:

$$\zeta = \sqrt{1 - e^2}, \psi = \tilde{\Omega} + \sigma\omega = \Omega + \sigma\omega - \lambda',$$

where $\sigma = \mathrm{sgn}(\cos i_0) = \pm 1$, so the angle variable ψ physically means the difference between the longitude of the pericenter of the satellite orbit, $\Omega + \sigma\omega$, and the mean longitude of the perturbing body, λ'.

The system of evolutionary equations written in the new variables,

$$\frac{d\zeta}{d\tau} = 20\sigma(\zeta^2 - 1)\sin 2\psi, \quad (2)$$
$$\frac{d\psi}{d\tau} = -\nu + 4\sigma\zeta(1 + 5\cos 2\psi),$$

has the first integral

$$\zeta + \frac{2\sigma}{\nu}(1 - \zeta^2)(1 + 5\cos 2\psi) = c_1, \quad (3)$$

where the constant c_1 is determined by the initial values ζ_0 and ψ_0.

(2) At $e = 0$, introducing the new variable $z = \cos i$, we can transform system (1) to the form

$$\frac{dz}{d\tau} = 4(z^2 - 1)\sin 2\tilde{\Omega}, \quad (4)$$
$$\frac{d\tilde{\Omega}}{d\tau} = -\nu - 8z\sin^2\tilde{\Omega},$$

and its first integral is

$$z + \frac{4}{\nu}(z^2 - 1)\sin^2\tilde{\Omega} = c_2,$$

where the constant c_2 is determined by the initial values z_0 and $\tilde{\Omega}_0$.

Vashkov'yak (2005) qualitatively analyzed both particular solutions and derived analytical τ dependences of the elements ζ and ψ at $\sin i = 0$ and the elements z and $\tilde{\Omega}$ at $e = 0$ in elliptic Jacobian functions.

ON THE STABILITY OF THE PLANAR SOLUTION TO INCLINATION

The qualitative features of the evolution of planar orbits and the analytical dependences $\zeta(\tau)$ and $\psi(\tau)$ are valid only if this planar particular solution is stable to the inclination of the satellite orbit. Restricting our analysis of the stability in the linear approximation in $\sin i$, we complement system of equations (2) by two equations,

$$\frac{d\rho_1}{d\tau} = b_1(\tau)\rho_1 + b_2(\tau)\rho_2, \quad \frac{d\rho_2}{d\tau} = \nu\rho_1 - b_1(\tau)\rho_2, \quad (5)$$

which are linearized relative to the new variables

$$\rho_1 = \sqrt{\zeta}\sin i\cos\tilde{\Omega}, \quad \rho_2 = -\sqrt{\zeta}\sin i\sin\tilde{\Omega}.$$

Here, the variable coefficients $b_1(\tau)$ and $b_2(\tau)$ are defined by the formulas

$$b_1(\tau) = \frac{10\sigma}{\zeta(\tau)}[\zeta^2(\tau) - 1]\sin 2\psi(\tau),$$
$$b_2(\tau) = -\nu - \frac{4\sigma}{\zeta(\tau)}\{2 + [1 - \zeta^2(\tau)][3 + 5\cos 2\psi(\tau)]\}.$$

In what follows, we will not consider the so-called "fall trajectories" corresponding to the collision of the satellite with the central attractive body; therefore, $\zeta(\tau)$ and $\psi(\tau)$ are periodic functions of τ, which can be calculated using elliptic Jacobian functions, and the period can be calculated using complete elliptic integrals of the first kind. Furthermore, below we consider the domain of parameters ν and $e_{\max}$ that corresponds to the condition that the modulus of the elliptic functions and integrals does not exceed unity and to the circulation variation in the angle variable ψ $\left(\frac{d\psi}{d\tau} < 0\right)$. The boundary of this domain is defined by the equations

$$e_{\max} = \frac{1}{12}\sqrt{\nu(24 - \nu)} \quad (6)$$

and

$$e_{\max} = \frac{1}{8}\sqrt{\nu(16 - \nu)} \quad (7)$$

for prograde and retrograde orbits, respectively.

For system of equations (5) under consideration, we can point out the case where the coefficients b_1 and b_2 are time independent. These are planar circular orbits with $e = 0$ and $\zeta = c_1 = 1$. In this case, the roots of the characteristic equation for the linear system with constant coefficients are given by the formula

$$\lambda_{1,2} = \pm\sqrt{-\nu(\nu + 8\sigma)}.$$

Table 1. Solutions of Eq. (8) for $\sigma = 1$ and $m/m^* = l/2$

m/m^*	2/1	3/1	4/1	5/1	3/2	5/2	7/2
ν_{m/m^*}	30.2557	26.3776	25.2734	24.7974	38.6730	27.6067	25.6951

Table 2. Solutions of Eq. (8) for $\sigma = 1$ and $m/m^* \neq l/2$

m/m^*	4/3	5/3	5/4	6/5	7/3	7/4	7/5
ν_{m/m^*}	47.1764	34.4278	55.6216	64	28.2508	33.0235	42.9223

Table 3. Solutions of Eq. (8) for $\sigma = -1$ and $m/m^* = l/2$

m/m^*	2/1	3/1	3/2	4/1	5/1	5/2	6/1
ν_{m/m^*}	16.9224	16.3776	17.8730	16.2068	16.1307	16.5591	16.0902

Table 4. Solutions of Eq. (8) for $\sigma = -1$ and $m/m^* \neq l/2$

m/m^*	4/3	5/3	5/4	6/5	7/3	7/4	7/5
ν_{m/m^*}	18.6050	17.4278	19.1772	19.6364	16.6508	17.2659	18.2626

Since ν is positive by its physical meaning, the zero solution of system (5) is stable for $\sigma = 1$, while for $\sigma = -1$ it is stable only at $\nu > 8$. The frequency of the small oscillations in variables ρ_1 and ρ_2 at $e = 0$ can be determined from the formula

$$\omega^2_{\rho_1\rho_2} = \nu(\nu + 8\sigma). \tag{8}$$

Of considerable interest for the subsequent analysis of the stability of the zero solution of system (5) is the case of parametric resonance where the commensurability condition for the oscillation frequencies of the variables (ρ_1, ρ_2) and the variables (ζ, ψ) is satisfied for integer m and m^*:

$$\omega^2_{\rho_1\rho_2}/\omega^2_{\zeta\psi} = (m/m^*)^2 = L, \tag{9}$$

where $\omega^2_{\zeta\psi} = (\nu + 16\sigma)(\nu - 24\sigma)$ at $e \to 0$ (Vashkov'yak 2005).

Equation (9) defines the special (resonance) values of the parameter ν that correspond to periodic solutions of the extended system of four equations (2), (5).

At $L = 1$, the only positive resonance value of $\nu_{m=1,m^*=1} = 24$ exists only at $\sigma = -1$.

At $L \neq 1$

$$\nu_{m/m^*} = 4\Big[-\sigma(1+L) \pm \sqrt{25L^2 - 22L + 1}\Big]/(1-L).$$

Tables 1 and 2 list the resonance values of ν_{m/m^*} for prograde orbits ($\sigma = 1$) and several small m and m^*. Table 1 contains parameter values of $\nu_{m/m^*} > 8$ corresponding to the half-integer ratios $m/m^* = l/2$ ($l = 1, 2, \ldots$) with $\lim\limits_{l\to\infty} \nu_{l/2} = 24$. In the ν, e plane, each of the points $\nu_{l/2}$ at $e > 0$ will generate narrow instability regions. Table 2 contains the values of $\nu_{m/m*}$ for which $m/m^* \neq l/2$ ($l = 1, 2, \ldots$); each of these values corresponds to a periodic solution of the evolutionary system at $e \to 0$ and $\sin i \to 0$.

Tables 3 and 4 give the resonance values $\nu_{m/m^*} > 8$ for retrograde orbits ($\sigma = -1$) at $m/m^* = l/2$ and $m/m^* \neq l/2$, respectively; Table 3 should be complemented by the above value of $\nu_{2/2} = \nu_{1/1} = 24$.

According to the Floquet–Lyapunov theory, in the general case $0 \leq e_0 < 1$, the stability of the zero solution of linear system (5) with T-periodic coefficients is determined by the quantity S, where S is the trace of the monodromy or fundamental matrix $\mathbf{M}(\tau = T)$ with $\mathbf{M}(\tau = 0) = \mathbf{E}$ (see, e.g., Yakubovich and Starzhinskiĭ 1972). At arbitrary ζ_0 and ψ_0, the matrix can be calculated only numerically. In this paper, we use the method of numerical integration of system (5) for $0 \leq \tau \leq T$, although the perturbation theory can be used at low e. It is easy to show that the stability of the zero solution of system (5) at fixed σ and ν is determined only by the integration constant c_1 and does not change as the initial position of the phase

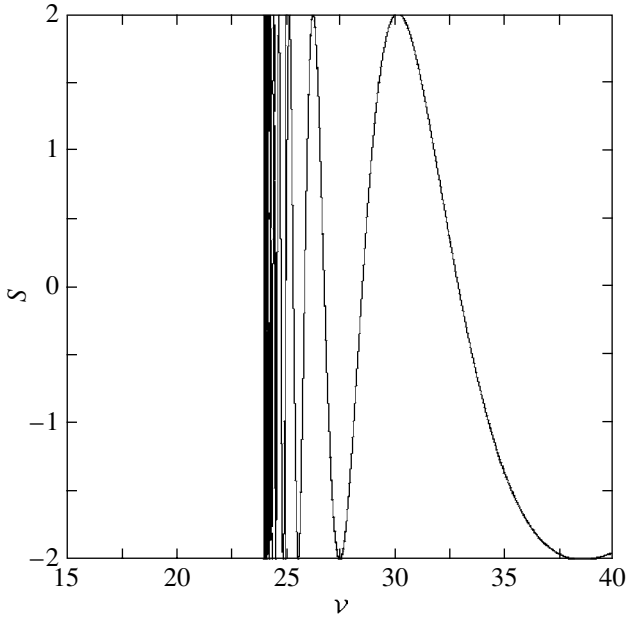

Fig. 1. Dependence of the trace of the monodromy matrix of system (5) on the parameter ν for $\sigma = 1$ and $e_0 = 0.1$.

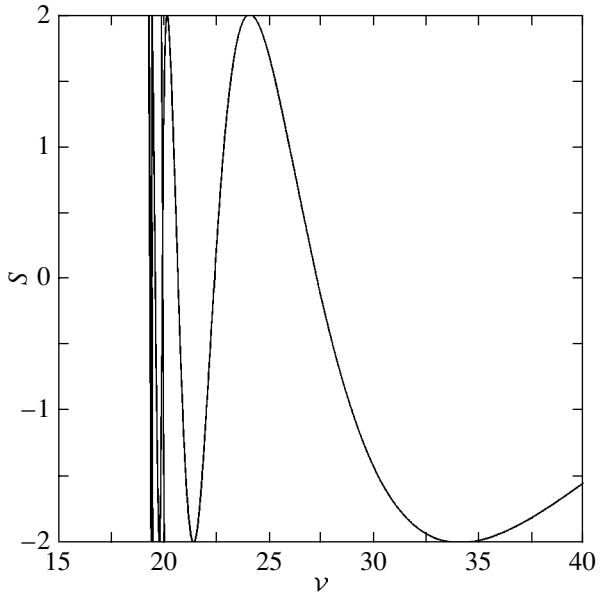

Fig. 2. Same as Fig. 1 for $e_0 \approx 0.8$.

point of system (2) changes on the integral curve (3). Therefore, in what follows, we assume that

$$\psi_0 = \frac{\pi}{4}(1-\sigma),$$

so $\zeta_0 = \sqrt{1-e_0^2}$ is equal to the minimum value of this variable, and, accordingly, e_0 is equal to the maximum value of the eccentricity, $e_{\max}$.

The stability condition for the zero solution of system (5) is

$$-2 < S(\sigma, \nu, e_0) < 2. \qquad (10)$$

Prograde Orbits ($\sigma = 1$)

Our calculations showed that condition (10) at $\sigma = 1$ and fixed e_0 is violated on a countable set of very narrow intervals within which $|S|$ differs very little from 2 and is of the order of 10^{-4}–10^{-6}. As an illustration, Figs. 1 and 2 show the dependence $S(\nu)$ for $e_0 = 0.1$ and $e_0 \approx 0.8$, respectively. The plots of the functions $S(\nu)$ virtually touch the $S = \pm 2$ straight lines, and the extrema at $e_0 = 0.1$ (Fig. 1) correspond to the ν values given in Table 1 for $e_0 = 0$ to within 0.1. These points of the ν axis generate extremely narrow instability regions the ν, e_0 plane (Fig. 3). We constructed the boundaries of these regions specified by the condition $|S| = 2$ using the general method of motion along the $f(x, y) = \text{const}$ isoline in the plane of variables x and y (Lidov *et al.* 1987). The corresponding half-integer ratio m/m^* of the frequencies of the variations of various pairs of variables—"planar" ζ, ψ and "spatial" ρ_1, ρ_2—are given near each of the regions (these are essentially lines). In Fig. 3, only the region that corresponds to the minimum resonance order $m + m^* = 3$ has a barely noticeable width, $\Delta\nu \approx 0.05$, while the value of S inside this region slightly exceeds 2. The considerably narrower adjacent instability regions to the right and to the left correspond to $S \le -2$; the signs of S at the boundaries alternate with decreasing ν, while $|S| < 2$ outside these regions. Such regions (lines) can be constructed, if necessary, for any given half-integer ratios m/m^*. The dashed line in Fig. 3 indicates the limiting curve, which is defined by Eq. (6) and emerges from the crowding point ($\nu = 24$, $e_0 = 0$). The region to the left and below this curve is of no particular interest and was not considered here. The dotted line in Fig. 3 indicates the curve defined by the equation

$$e_0 = \left(\frac{\sqrt{3}}{16}\nu\right)^{2/3} - 1. \qquad (11)$$

When condition (11) is satisfied, the apocenter of the satellite orbit touches the Hill sphere; therefore, the orbits located entirely within this sphere correspond to the region to the right and below the dotted curve, i.e.,

$$\nu > \frac{16}{\sqrt{3}}(1+e_0)^{3/2}.$$

To check the instability regions found and to illustrate the qualitatively different patterns of variation in the inclination of the orbits corresponding

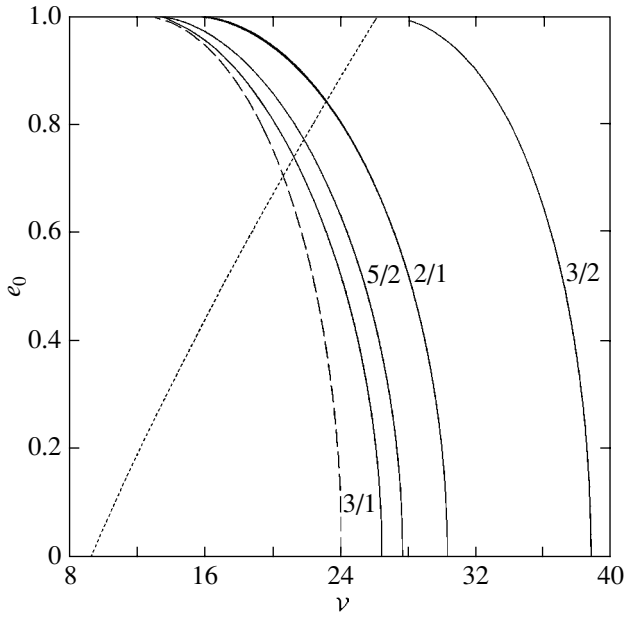

Fig. 3. Instability regions for the zero solution of system (5) in the ν, e_0 plane at $\sigma = 1$ (the dashed curve—the modulus of the elliptic functions and integrals is equal to unity; the dotted curve—the apocenter distance is equal to the radius of the Hill sphere).

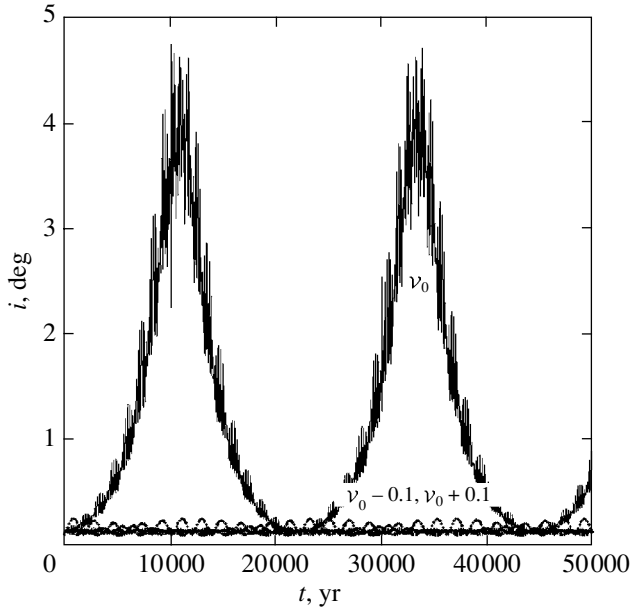

Fig. 4. Time dependences of the inclination for $i_0 = 0.^\circ1$, $e_0 = 0.78907686$, $\omega_0 = 252.^\circ035$, $\tilde{\Omega}_0 = -\omega_0$ ($\Omega_0 = 0$, $\psi_0 = 0$), $\nu_0 = 24.2$, $\nu_0 \pm 0.1$.

to different points in the ν, e_0 plane, we numerically integrated the complete (nonlinearized) system (1) at a small initial inclination $i_0 = 0.^\circ1$, $e_0 = 0.78907686$, $\omega_0 = 252.^\circ035 = \lambda'_0$, $\tilde{\Omega}_0 = -\lambda'_0$ ($\Omega_0 = 0$, $\psi_0 = 0$), and for several special values of ν. Figure 4 shows the variation in the inclination of a fictitious Saturnian satellite with an orbital semimajor axis of $a \approx 34.3$ million km perturbed by the Sun in a time interval of 50 thousand years. At given e_0, the corresponding $\nu_0 = 24.2$ corresponds to an inner point of the widest instability region; therefore, the inclination increases greatly compared to its initial value and reaches $\sim 4.^\circ7$ in the interval under consideration. However, the variation in the inclination of the orbit corresponding to this point of the instability region is limited, although it is appreciably larger than that for orbits that are stable in the linear approximation. The values of $\nu_0 \pm 0.1$ correspond to outer points near the boundary of the instability region, and, as a result, the inclination in the same interval differs only slightly from its initial value (by no more than $0.^\circ15$). The two lower dependences in Fig. 4 correspond to these ν_0. One of these dependences (for $\nu_0 + 0.1$) has a slightly larger amplitude than that for $\nu_0 - 0.1$. Note that the apocenter distances of the orbits considered do not exceed 62 million km and are located entirely within the Hill sphere of Saturn with a radius of $\sim$65 million km.

The tabular and graphic data presented here suggest that the planar prograde orbits in the problem under consideration are stable to inclination in the linear approximation virtually in the entire domain of ν and e_0 values considered. A countable set of extremely narrow regions in the plane of these parameters where the variation in inclination remains limited in a long time interval of the order of several thousand orbital periods of the planet when condition (10) is violated constitute an exception.

Retrograde Orbits ($\sigma = -1$)

Our calculations for retrograde orbits showed that condition (10) at fixed e_0 can be violated not only on a countable set of very narrow intervals, but also in fairly wide ν ranges. Only these ranges can be seen in Fig. 5, while the segments of the curves touching the $S = \pm 2$ boundaries are not shown in the figure. In addition to the extremely narrow regions (lines), the construction of the boundary curves revealed an instability region wider than that in the previous case (between the heavy solid lines in Fig. 6) within which $S > 2$. Of the entire set, Fig. 6 shows only two narrow resonance lines emerging from the points $e_0 = 0$, $\nu \approx 17.8730$ and $\nu \approx 16.9224$. The dashed line in Fig. 6, which is defined by Eq. (7), has the same meaning as that in Fig. 3, but it emerges from the point of crowding of the resonance curves ($\nu = 16$, $e_0 = 0$). We also excluded the region to the left and below this line from our analysis. The dotted curve is defined

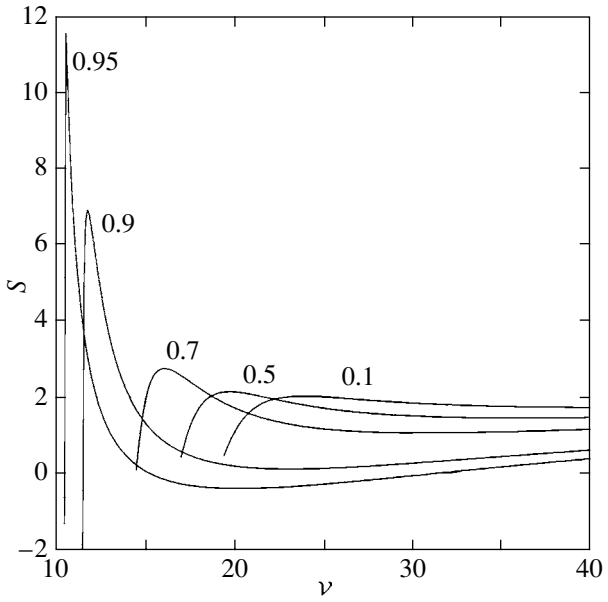

Fig. 5. Same as Fig. 1 for $\sigma = -1$ and $e_0 = 0.1, 0.5, 0.7, 0.9, 0.95$.

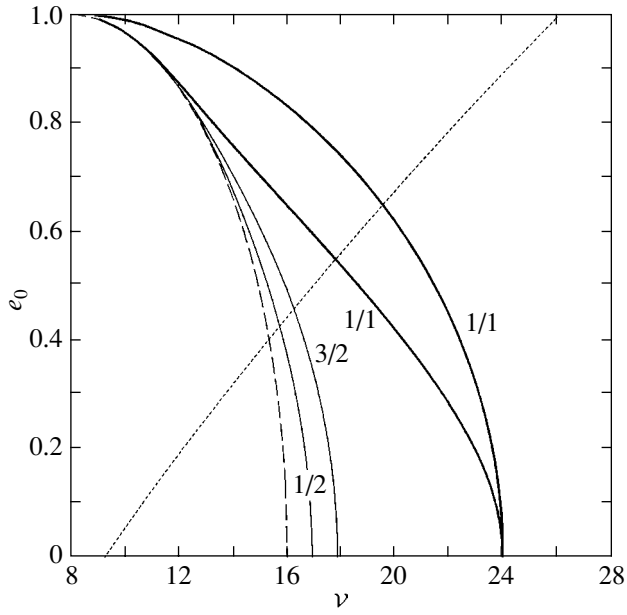

Fig. 6. Same as Fig. 3 for $\sigma = -1$ (the dashed curve—the modulus of the elliptic functions and integrals is equal to unity; the dotted curve—the apocenter distance is equal to the radius of the Hill sphere).

by Eq. (11) and follows the corresponding curve in Fig. 3. The domain of parameters e_0 and ν for which the satellite orbit lies entirely within the Hill sphere also has an identical location.

Just as in the case of prograde orbits, we performed check calculations of the evolution with the initial orbital elements $i_0 = 179.^\circ9$, $e_0 = 0.5$, $\omega_0 = 17.^\circ965 = -\lambda'_0 - 90^\circ$, $\tilde{\Omega}_0 = -\lambda'_0$ ($\Omega_0 = 0$, $\psi_0 = 90^\circ$) and for several special values of ν. The dependences $i(t)$ in Fig. 7 correspond to $\nu = \nu_0 \pm 0.15$ and $\nu_0 = 18.656$, i.e., to the immediate neighborhood of the left boundary of the instability region. The analogous dependences in Fig. 8 correspond to $\nu = \nu_0 \pm 0.15$ and $\nu_0 = 21.488$, i.e., to the immediate neighborhood of the right boundary of this region. For the above values of ν, the semimajor axes of the orbits of the fictitious Saturnian satellites are approximately 41 ± 0.2 and 37 ± 0.2 million km, respectively. We see from Figs. 7 and 8 that the change in the inclination outside the instability region does not exceed $0.^\circ3$. Inside this region, the inclination i can deviate appreciably from its initial value even near the boundary (18° in Fig. 8). The retrograde orbits considered are also located entirely within the Hill sphere of Saturn.

ON THE STABILITY OF THE CIRCULAR SOLUTION TO ECCENTRICITY

The qualitative features of the evolution of circular orbits and the corresponding analytical dependences are valid only when the particular solution itself is stable to the eccentricity of the satellite orbit. Restricting our analysis to the stability in the linear approximation in e, we complement system of equations (4) by two equations,

$$\frac{dh}{d\tau} = a_{11}(\tau)h + a_{12}(\tau)k, \qquad (12)$$
$$\frac{dk}{d\tau} = a_{21}(\tau)h - a_{11}(\tau)k,$$

linearized with respect to the variables

$$h = e\cos\omega, \quad k = e\sin\omega.$$

Here, the coefficients $a_{11}(\tau)$, $a_{12}(\tau)$, and $a_{21}(\tau)$ are periodic functions of τ defined by the formulas

$$a_{11}(\tau) = 20z(\tau)\sin 2\tilde{\Omega}(\tau),$$
$$a_{12}(\tau) = 4\{3 - 5z^2(\tau) + [1 + 5z^2(\tau)]\cos 2\tilde{\Omega}(\tau)\},$$
$$a_{21}(\tau) = 8[1 + 2\cos 2\tilde{\Omega}(\tau)].$$

The functions $z(\tau)$ and $\tilde{\Omega}(\tau)$ are periodic in τ. These functions and their period can be calculated using well-known relations.

The stability of the zero solution of system (12), like that of system (5), is determined by the trace of the monodromy matrix, which in the general case, i.e., at arbitrary values of the integration constant c_2, can be calculated only numerically.

In the simplest case of planar circular orbits where $\sin i_0 = 0$, $z_0 = c_2 = \sigma = \pm 1$, $a_{11}(\tau) = 20\sigma\sin 2\tilde{\Omega}(\tau)$,

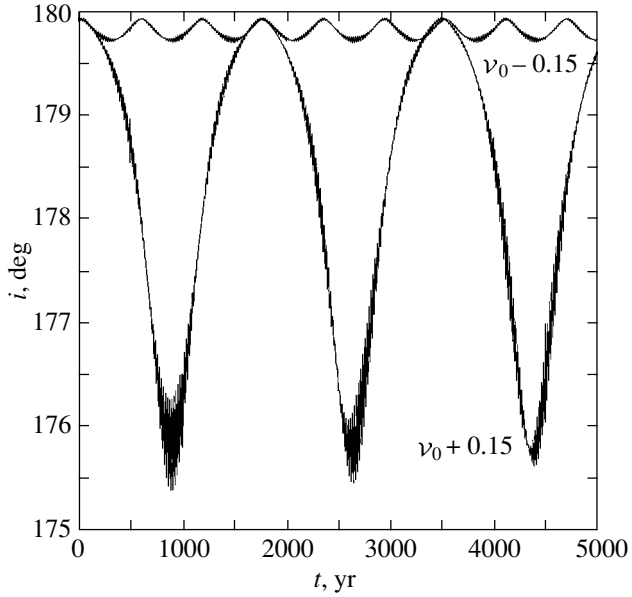

Fig. 7. Same as Fig. 4 for $i_0 = 179°.9$, $e_0 = 0.5$, $\omega_0 = 17°.965$, $\tilde{\Omega}_0 = \omega_0 + 90°$ ($\Omega_0 = 0$, $\psi_0 = 90°$), $\nu = 18.656 \pm 0.15$.

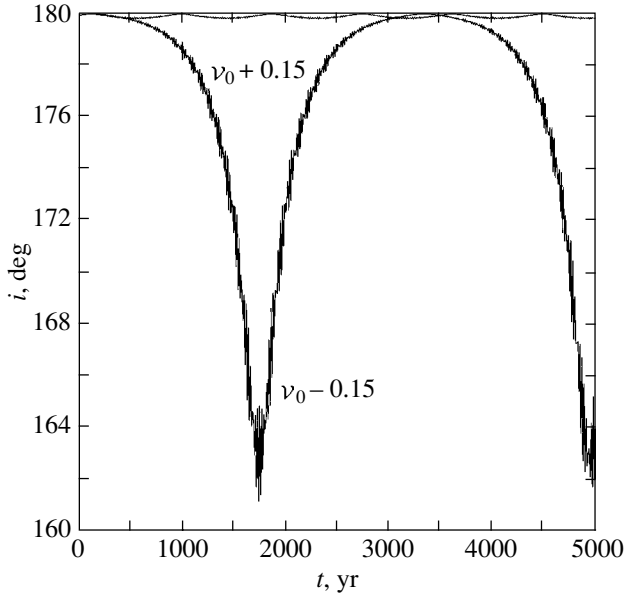

Fig. 8. Same as Fig. 7 for $\nu = 21.488 \pm 0.15$.

$a_{12}(\tau) = 8[3\cos 2\tilde{\Omega}(\tau) - 1]$, the linear transformation

$$(h\ k)^{\mathrm{T}} = \mathbf{A}(\tau)(y_1\ y_2)^{\mathrm{T}}$$

reduces system (12), in accordance with the well-known Lyapunov theorem (see, e.g., Yakubovich and Starzhinskiĭ 1972), to a system of equations with constant coefficients that is equivalent to the original one in terms of stability:

$$\left(\frac{dy_1}{d\tau}\ \frac{dy_2}{d\tau}\right)^{\mathrm{T}} = \mathbf{B}(y_1\ y_2)^{\mathrm{T}}. \qquad (13)$$

The orthogonal periodic matrix $\mathbf{A}$ and the constant matrix $\mathbf{B}$ are given by the formulas

$$\mathbf{A} = \begin{pmatrix} \cos\tilde{\Omega}(\tau) & \sigma\sin\tilde{\Omega}(\tau) \\ -\sigma\sin\tilde{\Omega}(\tau) & \cos\tilde{\Omega}(\tau) \end{pmatrix},$$

$$\mathbf{B} = \begin{pmatrix} 0 & 16 + \sigma\nu \\ 24 - \sigma\nu & 0 \end{pmatrix}.$$

The new variables y_1 and y_2 can be expressed in terms of the eccentricity e of the satellite orbit and the variable ψ used above and are defined by the formulas

$$y_1 = e\cos\psi, \quad y_2 = \sigma e\sin\psi.$$

The roots of the characteristic equation for system (13) are defined by

$$\lambda_{1,2} = \pm\sqrt{(\nu + 16\sigma)(24\sigma - \nu)}.$$

It thus follows that its zero solution is unstable at $\nu \le 24$ and $\nu \le 16$ if $\sigma = 1$ and $\sigma = -1$, respectively. In the opposite cases, i.e., at $\nu > 24$, $\sigma = 1$ and $\nu > 16$, $\sigma = -1$, the solution is stable. The frequency of the small oscillations in variables y_1, y_2 at $\sin i_0 = 0$ can be determined from the formula

$$\omega^2_{y_1y_2} = (\nu + 16\sigma)(\nu - 24\sigma) = \omega^2_{\zeta\psi}.$$

Of interest for the subsequent analysis of the stability of the zero solution of system (12) is the case of parametric resonance where the commensurability condition for the oscillation frequencies of the variables (y_1, y_2) and (z, $\tilde{\Omega}$) is satisfied at integer m and m^*,

$$\omega^2_{y_1y_2}/\omega^2_{z\tilde{\Omega}} = (m/m^*)^2 = \bar{L}, \qquad (14)$$

where $\omega^2_{z\tilde{\Omega}} = \nu(\nu + 8\sigma)$ at $\sin i \to 0$ (Vashkov'yak 2005).

Equation (14) defines the special (resonance) values of the parameter ν that correspond to periodic solutions of extended system of four equations (4), (12). At $\bar{L} = 1$, the only positive resonance value $\nu_{1/1} = 24$ exists only at $\sigma = -1$.

At $\bar{L} \ne 1$,

$$\nu_{m/m^*} = \frac{4}{1 - \bar{L}}\left[\sigma\left(1 + \bar{L}\right) \pm \sqrt{\bar{L}^2 - 22\bar{L} + 25}\right].$$

For prograde orbits ($\sigma = 1$) these values can be obtained from Tables 1 and 2 by substituting m^* for m and m for m^*. Of these, only one point $\nu_{1/2} \approx 30.2557$ at $\sin i_0 > 0$ generates a narrow region of instability of the zero solution of linear system (12) to eccentricity in the ν, $\cos i_0$ plane.

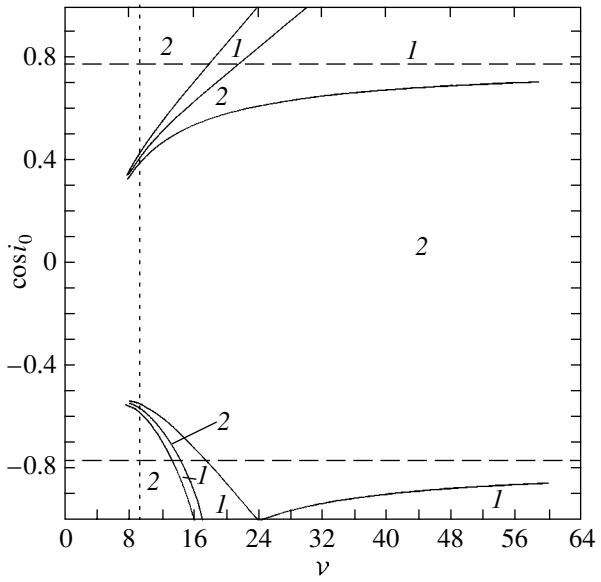

Fig. 9. Regions of linear stability (*1*) and instability (*2*) of the circular particular solution to eccentricity in the ν, z_0 plane (the horizontal dashed straight lines denote the critical inclinations, $\cos i_0 = \pm\sqrt{3/5}$).

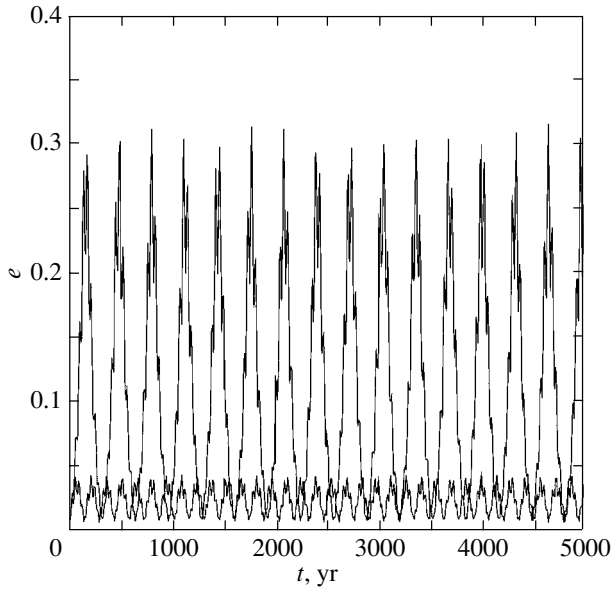

Fig. 10. Time dependences of the eccentricity for $e_0 = 0.01$, $\omega_0 = 0$, $\tilde{\Omega}_0 = 0$ ($\Omega_0 = 252\overset{\circ}{.}035 = \lambda'_0$), $\nu \approx 30$; $i_0^{(1)} \approx 48\overset{\circ}{.}7$ (lower and upper curve—$e_{\max}^{(1)} \approx 0.04$); $i_0^{(2)} \approx 51\overset{\circ}{.}7$ (upper curve—$e_{\max}^{(2)} \approx 0.3$).

The resonance values ν_{m/m^*} for retrograde orbits ($\sigma = -1$) can be obtained from Tables 3 and 4 using the same substitution as that for $\sigma = 1$. As will be seen from our numerical results, the point $\nu_{1/2} \approx 16.9224$ generates a narrow region in the ν, z_0 plane, while the point $\nu_{2/2} = \nu_{1/1} = 24$ generates, a very extended instability region.

The above regions at low and arbitrary values of $\sin i_0$ can be constructed using the perturbation theory and the numerical method of calculating the trace of the monodromy matrix, respectively. When calculating the monodromy matrix for system (13), we can assume that $\tilde{\Omega} = 0$, so $z_0 = \cos i_0$ is equal to the minimum value of this variable. The stability condition for the zero solution of systems (13) and (12) is

$$-2 < S(\nu, z_0) < 2. \qquad (15)$$

Our calculations show that for the given circular solution, condition (15) is violated in a wide region of the ν, z_0 plane. To reduce the amount of graphic data, we do not give the dependences $S(\nu)$ for fixed z_0. Figure 9 shows the structure of the regions of linear stability (*1*) and instability (*2*) of the circular solution to eccentricity.

Region *1* adjacent to the upper boundary, the horizontal line $z_0 = 1$, contains the narrow instability region (line) generated by the point $\nu_{1/2} \approx 30.2557$. The lower boundary of this region can be revealed only numerically, while its very existence in no way follows from the analysis of the simplest case of $z_0 = 1$. Region *1* adjacent to the lower boundary, the horizontal line $z_0 = -1$, contains the narrow region generated by the point $\nu_{1/2} \approx 16.9224$. In contrast to this region (line), the point $\nu_{1/1} = 24$ generates the widest instability region. For this ν, instability emerges at an arbitrarily small deviation of z_0 from -1 (or of i_0 from 180°). Just as in the doubly averaged Hill problem, circular orbits that are highly inclined to the plane of motion of the perturbing body ($z_0 \approx 0$) prove to be unstable to eccentricity (Lidov 1961; Kozai 1962). Furthermore, for $\nu \to \infty$, the boundaries of the instability region approach the horizontal lines corresponding to the *critical inclinations* $i_0 = \arccos\sqrt{3/5}$ and $i_0 = \pi - \arccos\sqrt{3/5}$ known from the papers mentioned above (the dashed lines in Fig. 9).

The dotted line in Fig. 9 indicates the vertical straight line

$$\nu = \frac{16}{\sqrt{3}}, \qquad (16)$$

which has the same meaning as that in Figs. 3 and 6. When condition (16) is satisfied, the satellite orbit touches the Hill sphere, so the region to the right of the dotted straight line corresponds to the orbits located entirely within this sphere.

We performed a check numerical integration of the complete (nonlinearized) evolutionary system of equations (1) for the orbits of fictitious Saturnian

satellites in a time interval of 5000 yr with the initial orbital elements $e_0 = 0.01$, $\omega_0 = 0$, and $\tilde{\Omega}_0 = 0$ ($\Omega_0 = \lambda_0'$). Several special pairs of ν and i_0 corresponded to the points located near the boundaries of the region, but on opposite sides of them. Our calculations showed that at small $e_0 = 0.01$, the maximum eccentricity $e_{\max}$ in the regions of linear stability does not exceed ~0.08. This value is considerably larger in the instability regions, where it reaches 0.8–0.95, and the eccentricity of the satellite orbit at $i_0 = 90°$ reaches unity in a finite time.

As an example, Fig. 10 shows the time dependences of the eccentricities of two orbits with $\nu \approx 30$ ($a \approx 29.8$ million km), $i_0^{(1)} \approx 48\overset{\circ}{.}7$, $i_0^{(2)} \approx 51\overset{\circ}{.}7$. At these parameters, we have $e_{\max}^{(1)} \approx 0.04$ and $e_{\max}^{(2)} \approx 0.3$ for stable (in the linear approximation) and unstable orbits, respectively.

CONCLUSIONS

In this paper, we analyzed the stability of particular solutions of the singly averaged Hill problem. Our linear analysis of the stability of these solutions in the simplest cases was continued numerically for arbitrary initial orbital parameters.

The planar particular solution is stable in the linear approximation to the sine of the inclination almost in the entire domain of admissible parameters ν and e_0 (or the semimajor axis and maximum eccentricity of the satellite orbit).

For prograde planar orbits, the countable set of narrow instability regions generated at $e_0 = 0$ by the singular (resonance) points of the ν axis constitutes an exception. The narrow instability regions found are essentially lines. The width of each instability region decreases with increasing order of the resonance between the frequencies of the small oscillations of two different pairs of satellite orbital elements (planar and spatial). The maximum width $\Delta\nu_{\max}$ of this region in the ν, e_0 plane corresponding to the minimum resonance order of 3 is ~0.05. A check numerical integration of the complete (nonlinearized) evolutionary system of equations showed that the change in the inclination for an inner point of this instability region, while remaining limited, exceeds the amplitude of the inclination oscillations for outer points close to the boundaries of the region by more than an order of magnitude.

For retrograde planar orbits, there is also a countable set of narrow instability regions generated at $e_0 = 0$ by the resonance points on the ν axis. In addition to this set, there is also an instability region generated by the point $\nu = 24$, $e_0 = 0$, which is much wider ($\Delta\nu_{\max} \approx 4$) than that for prograde orbits, while the change in inclination can reach 18° compared to the initial value.

The circular particular solution is unstable in a wide domain of parameters ν and $\cos i_0$ (or the semimajor axis and the maximum cosine of the inclination of the satellite orbit) and, in addition, inside two narrow regions (lines). Circular orbits with small inclinations to the plane of motion of the perturbing body ($\cos i_0 \approx \pm 1$) are stable in the linear approximation for physically plausible values of ν. These values are $\nu > 24$ and $\nu > 16$ for prograde and retrograde orbits, respectively. Only the two narrow regions mentioned above and the much wider region generated by the point $\nu = 24$, $\cos i_0 = -1$ constitute exceptions. As the inclination increases, this instability region expands and occupies most of the domain of parameters ν and $\cos i_0$. The instability region includes, in particular, the circular orbits orthogonal to the plane of motion of the perturbing body.

The regions of linear stability found for the two particular solutions of the singly averaged Hill problem under consideration determine the sets of parameters ν, e_0, and i_0 for which the previously derived analytical time dependences of the orbital elements and the qualitative patterns of orbital evolution are valid. The revealed resonance values of the parameter ν can be used to construct the planar periodic generating solutions and to numerically continue them into the region of spatial elliptical orbits.

REFERENCES

1. Y. Kozai, Astron. J. **67**, 591 (1962).
2. M. L. Lidov, Iskusstv. Sputn. Zemli **8**, 5 (1961).
3. M. L. Lidov, V. A. Lyakhova, and N. M. Teslenko, Kosm. Issled. **25**, 163 (1987).
4. N. D. Moiseev, Tr. Gos. Astron. Inst. im. P. K. Shternberga **XV**, 75 (1945a).
5. N. D. Moiseev, Tr. Gos. Astron. Inst. im. P. K. Shternberga **XV**, 100 (1945b).
6. M. A. Vashkov'yak, Pis'ma Astron. Zh. **31**, 545 (2005) [Astron. Lett. **31**, 487 (2005)].
7. V. A. Yakubovich and V. M. Starzhinskiĭ, *Linear Differential Equations with Periodic Coefficients* (Nauka, Moscow, 1972).

Translated by A. Dambis